VERLAG DER TECHNISCHEN UNIVERSITÄT GRAZ

Saniya Behzadpour

Assessment and mitigation of systematic errors in GRACE and GRACE-FO observations

GEOD 5

MONOGRAPHIC SERIES TU GRAZ
GEODESY

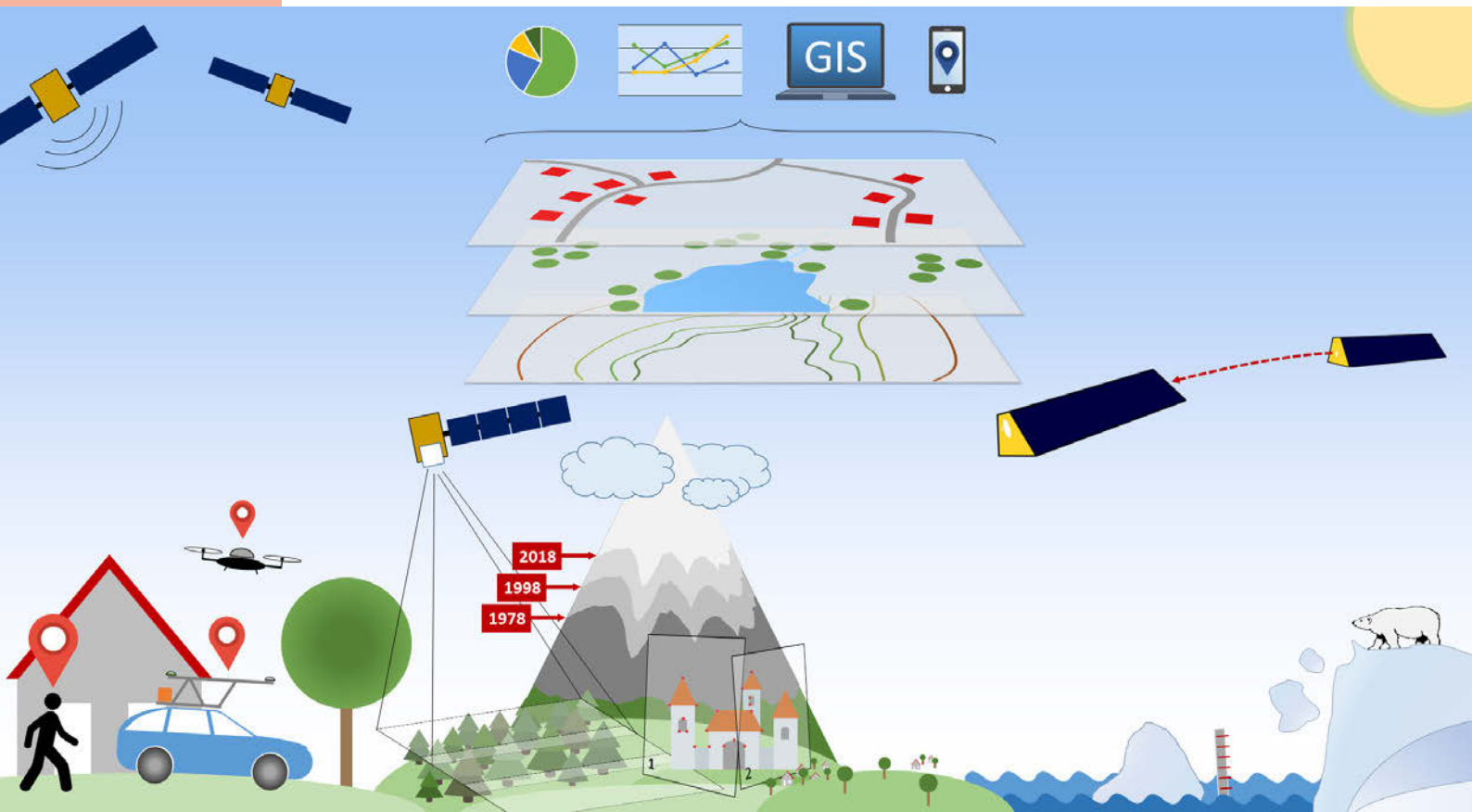

Saniya Behzadpour

Assessment and mitigation of systematic errors in GRACE and GRACE-FO observations

Monographic Series TU Graz

Geodesy

Series Editor:

Monographic Series TU Graz

Geodesy Volume 5

Saniya Behzadpour

Assessment and mitigation of systematic errors in GRACE and GRACE-FO observations

---

This work is based on the dissertation *"Contributions to GRACE/GRACE-FO Time-variable Gravity Field Recovery: Detection and Mitigation of Systematic Errors and Improved Single Accelerometer Approach"*, presented at Graz University of Technology; submitted to the Faculty of Mathematics, Physics and Geodesy in 2022.

Supervision / Assessment:
Torsten Mayer-Gürr (Graz University of Technology)
Gerhard Heinzel (Max Planck Institute)

Cover design Verlag der Technischen Universität Graz
Cover photo ifG, TU Graz

2022 Verlag der Technischen Universität Graz
www.tugraz-verlag.at

E-Book
ISBN 978-3-85125-933-9
DOI 10.3217/978-3-85125-933-9

Abstract

The research presented in this dissertation contributes to the ongoing effort of the geodetic community to improve the accuracy of temporal gravity field models derived from Gravity Recovery And Climate Experiment (GRACE) and its follow-on (GRACE-FO) mission. The conducted research is focused on three main subjects: Post-fit range rate residual analysis to identify remaining instrumental errors, modeling the identified errors, and improving the single accelerometer methodology.

The analysis of post-fit residuals leads to identification of un-modelled instrumental errors. To reduce these errors from the observations, a parametric model is developed and implemented within the gravity field recovery process. The proposed parametric model mitigate the impact of these errors on the observations and improves the estimates of gravity field parameters.

The last subject addresses the main challenge in the GRACE-FO processing, which is the reduced performance of one of the on-board accelerometers. Here, a novel approach to recover the accelerometer data by incorporating non-gravitational force models is proposed. This allows for the computation of an alternative data product, which significantly improves the overall accuracy of the gravity fields.

Kurzfassung

Die in dieser Dissertation vorgestellte Forschung trägt zu den laufenden Bemühungen der geodätischen Gemeinschaft bei, die Genauigkeit von zeitlichen Schwerefeldmodellen zu verbessern, die vom Gravity Recovery And Climate Experiment (GRACE) und seine Folgemission (GRACE-FO) abgeleitet sind. Die durchgeführte Forschung konzentriert sich auf drei Hauptthemen: Post-Fit-Residualanalyse zur Identifizierung verbleibender instrumenteller Fehler, Modellierung der identifizierten Fehler und Verbesserung der Einzelbeschleunigungsmesser-Methodik.

Die Analyse von Post-Fit-Residuen führt zur Identifizierung von nicht modellierten Instrumentenfehler. Um diese Fehler zu reduzieren, wird ein parametrisches Modell entwickelt und innerhalb der Schwerefeldprozessierung implementiert. Dieses Modell mildert die Auswirkungen dieser Fehler auf die Beobachtungen und verbessert die Schätzungen der Schwerefeldparameter.

Der letzte Abschnitt behandelt die verminderte Leistungsfähigkeit eines Beschleunigungssensors bei GRACE-FO. Dabei wird ein neuartiger Ansatz zur Wiederherstellung der Beschleunigungsdaten durch die Verwendung von nicht-gravitativen Kräftemodellen vorgeschlagen. Dies ermöglicht die Berechnung alternative Daten, das die Gesamtgenauigkeit der Gravitationsfelder erheblich verbessert.

Acknowledgements

This dissertation would not have been possible without the support and help of a number of wonderful individuals. I am deeply thankful to each and every one of them for being a part of this journey.

First and foremost, I owe my deepest gratitude to my supervisor, Univ.-Prof. Torsten Mayer-Gürr, for his continuous support, encouragement, and patience. I have been very lucky to have a supervisor who cared so much about my work, encouraged me to think outside the box, and gave me the right guidance throughout my study. I also would like to express my gratitude to Prof. Gerhard Heinzel for his time and consideration as the external reviewer and co-examiner.

I am forever thankful to my current and former colleagues at the working group for their support, companionship, and valuable feedbacks, and of course for teaching me how to play foosball in breaks.

Lastly, I would like to thank my parents for always encouraging me to pursue my dreams, for their unconditional love and their constant support throughout my life.

Contents

Introduction

1

1.1. Motivation

The total amount of water on a planet is defined as a hydrosphere. The hydrosphere includes water that is stored in vapor, liquid or in solid state around the plant. On Earth, water is stored in numerous places: in the oceans, as water vapor in the atmosphere and in natural reservoirs on the continents. These include surface waters such as streams, rivers, lakes, underground water resources, as well as the storage of water in frozen form as snow and glacier ice. Water is in constant exchange between all storage compartments. It evaporates from the land surface and the oceans and enters the atmosphere as water vapor. If the water vapor condenses to form precipitation, it fills the various reservoirs on the continents as rain or snow. Water that does not evaporate from there flows back into the ocean via the surface water network or as groundwater. These diverse storage and exchange processes form the global water cycle, which on the one hand depends heavily on the current and future climate and on the other hand influences climate development itself. A global warming of 1 °C theoretically increases the capacity of the atmosphere to absorb water vapor by 7% (Coumou & Rahmstorf, 2012), which could lead to an increase in precipitation. So far, however, such model estimates can hardly be substantiated by empirical data, as there are only sufficient measurement data for a few regions. The water cycle on the continents is subject to many variations in space and time. The water balance varies between precipitation, evaporation, runoff and storage depending on the climatic zone, season or natural conditions. Environmental changes such as climate change, changes in land cover and land use due to the expansion of agricultural or urban areas and other anthropogenic interventions such as the construction of reservoirs or the extraction of groundwater can have significant effects on the water cycle. Our water needs are met from the Earth's freshwater resources, from surface waters such as rivers and lakes, but in many regions in particular from the water stored underground. This groundwater covers around 50% of the world's water needs for households, agriculture and industry, in rural areas even up to 90%. In many regions, the future economic and social development of society depends on the availability and sustainable management of water.

In many cases, the availability of water and its variability, is not yet sufficiently known and understood. The terrestrial measurement of water storage is difficult, on the one

hand because of a large number of different compartments, each of which would have to be measured individually. On the other hand, there is the difficulty that the groundwater in particular is difficult to access. Therefore, water quantities can often only be estimated from point measurements and with indirect methods.

With the satellite mission Gravity Recovery and Climate Experiment (GRACE), on the other hand, changes in gravity over time can be measured (Tapley et al., 2004). These changes are a direct expression of the mass changes occurring on or below the Earth's surface, including the variations in continental water storage. The extraordinary importance of GRACE for hydrology lies in the fact that it is the only observation system that can record changes in storage on the continents over a large area and integrate all storage compartments. With GRACE it was possible for the first time to provide global data showing the variability of water storage on monthly, seasonal and interannual time scales.

After more than 15 years of providing high resolution maps of Earth's mass transport, the science operations of the twin satellite mission GRACE came to an end on October 27, 2017. During its successful mission, GRACE provided unprecedented track record of the global mass re-distribution, substantially contributing to the understanding of natural processes in hydrology, oceanography, glaciology and other divisions of geophysics (e.g. Chambers, 2006; Chen et al., 2010; Wouters et al., 2019)

Continuing the legacy of GRACE, the next generation mission Gravity Recovery and Climate Experiment Follow-On (GRACE-FO) started on May 22, 2018 and is providing high-quality measurements required for extending the GRACE gravity time series ever since (Landerer et al., 2020). Beside undertaking the task of monitoring temporal gravity field from its predecessor, GRACE-FO is also a technology demonstrator, which tests the operation of the first inter-satellite laser interferometer in space.

Several analysis centers produce global temporal gravity models based on the data collected by GRACE and GRACE-FO. The official centers, i.e. the German Research Center for Geosciences (german: "Deutsches GeoForschungsZentrum"(GFZ)), the Center for Space Research (CSR) at University of Texas in Austin, and the Jet propulsion laboratory (JPL), regularly produce series of monthly/sub-monthly gravity field solutions in terms of spherical harmonics. In recent years, alternative GRACE gravity field models have also been published by other centers, such as GRGS (Groupe de Recherches de Geodesie Spatiale) solutions at CNES (Centre National d'Etudes Spatiales), AIUB (Astronomical Institute of the University of Bern) solutions at University of Bern, DMT (DEOS Mass Transport) solutions at Delft University of Technology, and Tongji solutions at Tongji University.

Since 2014, Institute of Geodesy at Graz University of Technology (TUG) biennially releases independent GRACE-only gravity series. The solutions are labeled as ITSG

and are developed within the working group of theoretical and satellite geodesy. The ITSG-Grace2018 (Kvas et al., 2019) gravity field model is the latest release of the ITSG sequence and similar to the previous releases, contains a high-resolution static field, unconstrained monthly solutions, and constrained daily solutions.

Despite a gradual improvement in the accuracy level of the published products, the expected accuracy based on pre-launch simulation studies, known as GRACE baseline, has not been reached. One reason why the predicted accuracy is not feasible, even in the middle of the GRACE mission, when the satellites provided high-quality measurements, lies in the fact that the following technical limitations of the mission were not taken into account:

Background model uncertainties During the estimation of gravity parameters from the satellite data, the static gravity field and its known variations, e.g. tides, are reduced from the observed gravity field through a priori models, so-called background models. In reality, however, these models are imperfect and their uncertainties propagate to the gravity parameters through the estimation process.

Geophysical aliasing The monthly solutions are averages over constant interval of a month. On the other hand, mass variations occur over the entire globe, in both spatial and temporal domains. These variations are sampled only along orbital ground tracks, causing undersampling (alias contamination).

Instrumental errors GRACE and GRACE-FO observations include several instrumental error sources. For instance, close to the end of the GRACE mission, due to the reduced battery capacity, the on-board accelerometer of the GRACE-B was turned off, and its measurements were replaced by synthetic accelerometer data, also known as transplant data. GRACE-B transplant data is generated by a series of adjustments to the GRACE-A accelerometer measurements. Similarly, at the beginning of GRACE-FO mission, the GRACE-D accelerometer data degraded and were required to be replaced with synthetic data as well. Using the synthetic accelerometer data in both missions is one of the main challenges of providing high-quality gravity field models.

The key problem is that some of these errors cannot be detected and therefore corrected before gravity determination as they are superimposed upon the sought-after gravity signal. Therefore, the efforts shall continue to disentangle and mitigate remaining errors during the gravity determination process. Any feasible refinement in this process not only contributes to improving the quality of the gravity products of the GRACE and GRACE-FO, the lessons learned are also beneficial for any future GRACE-like mission.

1.2. Objectives

The main objective of this work is to improve the quality of monthly gravity field solutions by identifying the remaining errors within the GRACE processing chain and investigate alternative approaches which fully incorporates the characteristics of the errors within the scope of ITSG-Grace2018. The conducted research is focused on three aspects of the gravity recovery:

- Post-fit range rate residual analysis to identify remaining instrumental error sources,
- Mitigating KBR systematic errors using parametric models,
- Improving the single accelerometer methodology.

1.3. Outlines

This work is divided into 7 chapters. The first three chapters develop the foundations of the topic, starting with introducing the satellites and their instruments, followed by the relevant mathematical backgrounds required in the course of this research.

Chapter 4 investigates the ability of wavelets to help in identifying specific error sources in GRACE range-rate residuals. The multi-resolution analysis (MRA) using discrete wavelet transform (DWT) is applied to decompose the residual signal into different scales with corresponding frequency bands. Temporal, spectral, and orbit-related features of each scale are then extracted for further study. The chapter continues to describe the propagated errors from K-Band Ranging (KBR) system, systematic errors due to the Sun intrusions into one of the star cameras, and introduces the eclipse transition spikes. These type of errors are one of the primary results of the proposed analysis.

Chapter 5 focuses on the two later error sources, i.e. eclipse transition and Sun intrusion errors. It contains detailed descriptions of their corresponding event detection and model characteristics. This follows by the description about setting up their parametric model in the gravity field estimation process.

Chapter 6 contributes to an improvement of the GRACE-FO derived gravity field solutions by investigating the role of the degraded GRACE-D accelerometer data. This chapter present a novel approach to recover this data by incorporating non-gravitational force models. The comparison between the alternative dataset and the officially provided data is presented and their impact on monthly gravity field solutions is studied.

Chapter 7 contains the summary and conclusions of the study.

GRACE and GRACE-FO missions

2

The following chapter gives an overview on the GRACE and GRACE-FO missions, their objectives, measurement concept, instruments, and data products. For further details, the reader is referred to Case et al. (2010), Wen et al. (2019), and the references therein.

2.1. Mission overview

GRACE was a satellite gravimetric mission, supported by National Aeronautics and Space Administration (NASA) in the United States and German Aerospace Center (DLR) in Germany (Tapley et al., 2004). The primary objective of the mission was to obtain global high-resolution maps of the Earth's gravity field for a planned lifetime of up to five years. This objective was achieved by measuring the inter-satellite range and its variation between two satellites in a trailing formation. The secondary science objective of the GRACE mission was to provide global temporal temperature and humidity profiles. This is done through GPS radio occultation measurements for weather prediction application.

The twin satellites shared a near circular polar orbit at the launch altitude of approximately 490 km and followed each other at a distance between 170 to 270 km. Considering a non-repeating orbit and formation design, GRACE was able to cover the globe every 30 days, collecting required measurements to determine Earth's gravity field. Along with the changing inter-satellite range, each satellite determined its position, velocity, attitude, and the acted upon accelerations due to non-gravitational forces.

After 15 years and 7 months, more than trice the designed lifetime, the GRACE operational mission phase ended in October 2017. The successor mission, GRACE-FO, with the primary objective of GRACE observation continuity, was successfully launched on May 22, 2018 (Landerer et al., 2020). Having many similarities in configuration and orbit design to GRACE, GRACE-FO is additionally serves as a technology demonstrator, having the first Laser Ranging Interferometer (LRI) on-board.

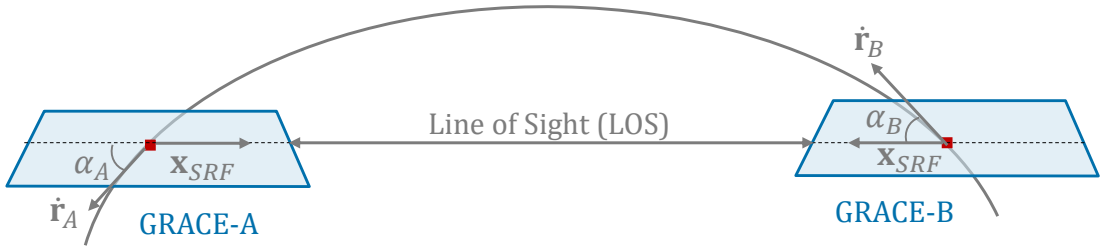

Figure 2.1.: The geometry of LOS and orientation of the leading and trailing satellite. A pitch angle offset (α_A, α_B) enables inter-satellite ranging.

2.2. Measurement principle

The fundamental measurement principle for determining the Earth's gravity field parameters is distance measurements between the two satellites, which are combined with position, velocity and acceleration measurements. Due to the Earth's in-homogeneous mass distribution and continuous re-distribution, the gravitational force acting on each satellite slightly differs from the other twin, which results in continuous variations in the inter-satellite distance.

For both missions, the distance between the two satellites is measured with a dual one-way K/Ka Band Ranging (KBR) measured with a noise level of approximately 1 µm/$\sqrt{\text{Hz}}$ at a frequency of 0.1 Hz. The GRACE-FO satellites additionally provide LRI ranging measurements, but with much less noise at a level of 1 nm/$\sqrt{\text{Hz}}$ at frequencies over 0.1 Hz (Abich et al., 2019).

During the science phase, the satellites are in a nominal orientation, as depicted in Figure 2.1, with the two K-Band antenna pointing along the Line of Sight (LOS) with a precision of a few milliradians. This requires both satellites to fly with a $\pm 1°$ pitch angle offset to provide precise inter-satellite pointing.

The measured inter-satellite distance is however affected by both gravitational and non-gravitational forces. For gravity field recovery, the variations induced by the gravitational forces need to be separated from the non-gravitational forces. This is achieved by the measurements of the accelerometer (ACC), which precisely measures the non-gravitational forces acting on the satellites.

2.3. On-board instruments

The Science Instrument System (SIS) includes all scientific sensors of the inter-satellite ranging system, the GPS receivers, and associated sensors such as Star Camera Assembly (SCA). The following explains the science instruments of GRACE/GRACE-FO which are of particular interest within the scope of this dissertation.

2.3.1. Accelerometer

For both missions, the on-board accelerometer is a three-axis electrostatic accelerometer manufactured by the Office National d'Études et de Recherches Aérospatiales (ONERA) (Christophe et al., 2015; Touboul et al., 1999). The accelerometer provides information about the linear and angular acceleration of the satellite, with two high-sensitive axes, the radial and along-track axes exhibiting a resolution better than $0.1\ \mathrm{nm}/(\mathrm{s}^2\sqrt{\mathrm{Hz}})$, and one less-sensitive axis, the cross-track axis with a precision of $1\ \mathrm{nm}/(\mathrm{s}^2\sqrt{\mathrm{Hz}})$.

The accelerometer is placed in the center of mass (CoM) of the satellite. The core of the sensor consists of a proof mass, surrounded by an electrode cage. The proof mass is suspended by electrostatic forces generated by the electrodes. The sensor measurement is determined from the usage of analog voltages, producing the electrostatic force. The electrostatic force is proportional to the sum of the non-gravitational forces acting on the satellite and other disturbances. Linear acceleration measurements are given in the accelerometer reference frame (AF), with he origin of this frame placed in the center of mass of the proof mass (cf. Appendix A).

Following a battery cell failure in September 2016, the accelerometer on-board GRACE-B was switched off and its measurements were replaced by synthetic data. These synthetic data were obtained from the GRACE-A accelerations, by applying time and attitude corrections and GRACE-B thruster responses (Bandikova et al., 2019). In the case of GRACE-FO, from the beginning of the mission the ACC measurements from both satellites were contaminated by different types of noise. To achieve a sufficient accuracy for gravity field recovery, a series of calibration processes were needed to be applied. Furthermore, after approximately one month in orbit, the GRACE-D accelerometer has started showing non-nominal behavior. Following a mode switch on June 21, 2018, noise levels on GRACE-D increased substantially on all axes, and the data again needed to be substituted by synthetic ACC data. For this reason, the GRACE-FO Science Data System (SDS) team has developed and provided calibrated accelerometer data (ACT) products (McCullough et al., 2019). More details on ACT products are given in Chapter 6.

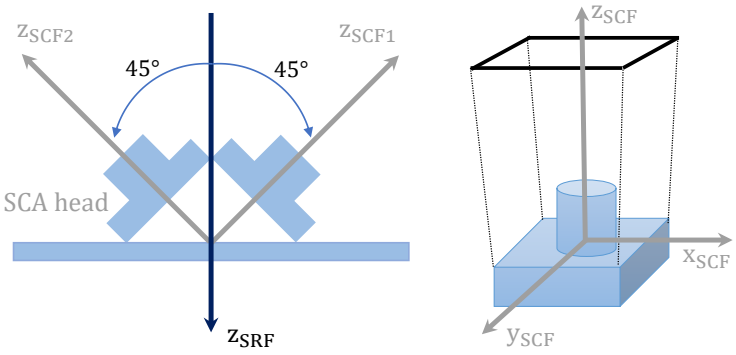

Figure 2.2.: Illustration of the star camera unit configuration (left) and an individual camera head (right).

2.3.2. Attitude and orbit control system

The Attitude and Orbit Control system (AOCS) determines satellite orientations and orbital positions and provides three-axis stabilized Earth-pointing attitude control throughout the mission. This system includes a GPS receiver, SCA, high-performance gyro package, coarse Earth and Sun sensor, magnetometer, Inertial Measurement Unit (IMU), magnetic torquers and a cold gas propulsion system.

Star camera assembly

The SCA provides satellite attitude data w.r.t. the inertial reference frame (cf. appendix A). For GRACE, the system consists of two star camera heads pointing to the lateral sides of the spacecraft, as shown in Figure 2.2, whereas GRACE-FO SCA has an additional camera head pointing upwards. The extra camera head increases attitude data availability during Sun/Moon blinding and improves accuracy about all directions. Each camera observes and detects the star constellation that is visible within their rectangular field of view (FoV). Using the available star catalogs on-board, they can provide information about the spacecraft attitude.

Cold gas propulsion system

Cold gas thrusters are highly reliable as well as low cost actuators for the attitude and orbit control. Each satellite has twelve 10 mN gas thrusters for attitude control, and two 10 mN thrusters for orbit control. The orbit control thrusters are used for obit maneuvers to maintain the required separation distance or the swap maneuver. These thrusters are barely used (2-3 times per year) as these maneuvers are rarely

performed. On the contrary, the attitude control thrusters are activated more frequently, approximately 1000 per day.

2.3.3. K/Ka Band Ranging

In both missions, KBR is the primary scientific instrument for providing range information. For the inter-satellite ranging, each satellite transmits and receives two carrier signals at specific frequencies in the K and Ka-Band. The range is then derived for both of these bands, based on the interferometric principle. By combining the two ranging observations, one can derive a so-called ionosphere-free range $\Delta\rho_{KBR}$. To yield observations of the inter-satellite distance ρ_{SST}, the complete ranging equation is (Kim & Tapley, 2002):

$$\rho_{SST} = \Delta\rho_{KBR} + \Delta\rho_{AOC} + \Delta\rho_{LTC} + n + e, \tag{2.3.1}$$

where $\Delta\rho_{AOC}$ is antenna offset correction (AOC), $\Delta\rho_{LTC}$ is light time correction for the distance the satellites travelled during the signal transmission, n is an unknown integer-cycle phase ambiguity, and e is some random error.

2.3.4. Global Positioning System Receiver

The Global Positioning System (GPS) Receiver Assembly is used for precise orbit determination and time synchronization of the satellites. Each satellite is equipped with three GPS antennas: The main antenna is located on the top of the spacecraft for positioning, and one back-up antenna on the rear panel as well as an occultation antenna for determination of vertical temperature and humidity profiles. The GPS time information also serves as an absolute timing reference for the on-board computer (OBC).

2.4. Data levels

The SDS members are responsible for processing, verification, and distribution of science and housekeeping telemetry data as well as any secondary data, e.g., meteorological and hydrological data, required for processing and verification (Case et al., 2010; Wen et al., 2019). The data products are processed at various levels ranging from Level 0 to Level 3, as shown in Figure 2.3. Data products resulting from Level-1A through 3 will be provided to the scientific community.

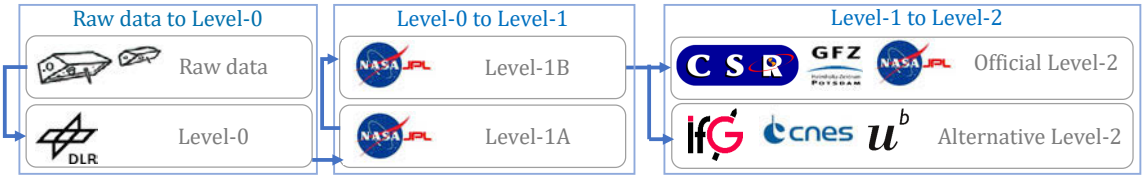

Figure 2.3.: Illustration of the Level-0 to Level-2 data processing.

Level-0: Level-0 data are raw data products at full instrument resolution achieved by telemetry collection by the GRACE Raw Data Center (RDC) of the Mission Operation System (MOS) at DLR in Neustrelitz, Germany. The DLR is responsible for the telemetry data reception as well as the mission control of the satellites. The telemetry data includes the Science Instrument and Spacecraft Housekeeping data, which are received twice per day and then stored in appropriate format in an archive at the RDC.

Level-1A: Level-1A data are the result of non-destructive processing applied to Level-0 data, meaning that the Level-1A data are reversible to Level-0. To convert the binary encoded measurements to physical units, a set of calibration factors is applied to the measurements. The data are transformed to the corresponding satellite receiver time-frame, and if needed, time tag integer second ambiguity is resolved. Additionally, they are edited and marked with "flags" that indicate data quality. Finally the data is reformatted for further processing.

Level-1B: Level-1B data are the result of irreversible processing applied to Level-1A data. They are down-sampled and transformed to GPS time, then cleaned and filtered to convert to desired quantities for Level-2 processing. The processing from Level-0 to Level-1B is called the Level-1 Processing, which is officially conducted by JPL.

Level-2: Level-2 data include the daily/weekly, monthly, and static gravity field derived from calibrated Level-1B data products. The three official processing centers have developed their Level-2 processing software independently, and routinely published their products. Furthermore, alternative GRACE gravity field models have also been published by other centers. The planned latency for monthly gravity field model is within 60 days of the data acquisition. The Level-2 data products also include ancillary data products (e.g., mean atmospheric and oceanic mass variations), which are necessary to study temporal variations within the gravity field solutions.

Level-3: Level-3 data are the transformed gravity anomalies to monthly land mass grids that usually contain terrestrial water storage anomalies (Landerer & Swenson, 2012). To achieve Level-3 products, the Level-2 input data needs post-processing filtering as well as geophysical data corrections.

Table 2.1.: Required GRACE/GRACE-FO Level-1 data products for the presented research.

Data products	Release	Description
ACT1A	-	Calibrated 10-Hz linear acceleration in AF and OBC time
ACT1B	RL04	Calibrated 1-Hz linear acceleration
ACC1B	RL02, RL04	1-Hz Linear accelerometer data
SCA1B	RL03, RL04	Processed SCA data for rotation from CRF to SRF
KBR1B	RL03, RL04	K-Band ranging data and the corrections
CLK1B	RL02, RL04	Receiver clock offsets to convert time tags to GPS time
TIM1B	RL02, RL04	Time conversion from OBC to GPS time
GNV1B	RL02, RL04	Satellite's position and velocity, given in TRF
THR1B	RL02, RL04	Thruster activations given in GPS time
MAS1B	RL02	Total satellite mass in kilograms

2.5. Data products

The analysis and results presented within this dissertation are based on the GRACE-FO Level-1A data, GRACE Release 02-03 (RL02-RL03) and GRACE-FO RL04 Level-1B data products. Table 2.1 summarizes the complete list of the used data products. All Level-1B science data products are presented in the Science Reference Frame (SRF; Appendix A), and GPS time format.

2.6. ITSG-Grace2018

The Theoretical and Satellite Geodesy (ITSG) working group of Institute of Geodesy at Graz University of Technology has a successful record in producing GRACE-only gravity field solutions using an in-house developing software, the Gravity Recovery Object Oriented Programming System (GROOPS) (Mayer-Gürr et al., 2021). The ITSG-Grace2018 gravity field model (Kvas et al., 2019) is the latest release of the ITSG sequence covering the complete GRACE time-span. To continue the GRACE time series, ITSG-Grace2018 is routinely updated with operational GRACE-FO solutions, using a consistent processing scheme.

ITSG-Grace2018 is mainly computed from the official Level-1B products. Additionally, in-house computed kinematic orbit positions for both satellites serve as observations

in the gravity field recovery. The kinematic orbit positions were computed following the raw acceleration approach of Zehentner and Mayer-Gürr (2016).

Before the start of the gravity field recovery, additional preprocessing steps, suggested by Klinger (2018), are followed to improve the data quality. The preprocessing starts with resampling of the Level-1B science data to a common sampling of 5 s. In the next step, a threshold-based data screening algorithm identifies and excludes large outliers from each data product. Apart from outliers, epochs around calibration and yaw-turn maneuvers were also removed from further processing. For more details on the data screening and preprocessing, the reader is addressed to Klinger (2018).

The background models used in ITSG-Grace2018 contain state-of-the-art geophysical models and are also consistent with the current RL06 of the official centers. A detailed list of all background models used for GRACE and GRACE-FO solutions can be found in Table 2.2.

To set-up the observation equations, three observation groups are introduced in the adjustment process: The satellite positions from kinematic orbits, the KBR range-rate observations, and the pseudo-observations which constrain the daily gravity fields (Kvas et al., 2019). The variational equation approach is followed to set up the observation equations as well as the integration of each satellites' reduced dynamic orbit (Ellmer & Mayer-Gürr, 2017). In the initial step, the dynamic orbits are integrated for an arc length of 24 hours using background models and the Level-1B dynamic orbit, and the pre-calibrated accelerometer data. The accelerometer parameterization is based on the approach introduced by Klinger and Mayer-Gürr (2016a): The scale factors are estimated daily using a fully populated matrix. The accelerometer biases are also estimated daily, parameterized by cubic B-splines with 6-hour knots. In order to improve the accuracy, the resulting dynamic orbit is fitted to kinematic orbits and range rate observations in a least squares adjustment. In the course of this adjustment, the initial orbit states of both satellites and accelerometer calibration parameters are also estimated. The resulting dynamic orbit and calibrated accelerometer data are used to re-integrate the orbit to reach a convergence on the sub-micrometer level. The outputs are the final dynamic orbits, state transition, and sensitivity matrices, which are required to set up the observation equation system. The equation system is assembled not only for mean monthly gravity coefficients but also for co-estimated daily gravity parameters and calibration parameters.

The daily gravity coefficients up to degree 40 are computed in order to recover sub-monthly gravity variations within the framework of a Kalman smoother estimation (Kurtenbach et al., 2012). The Kalman smoother utilizes a prior information about the temporal-spatial correlations of the daily gravity fields. This prior information is derived from geophysical models in terms of an empirical covariance function,

Table 2.2.: Comparison between ITSG-Grace2018 and ITSG-Grace operational force models

Perturbation	ITSG-Grace2018	ITSG-Grace operational
Earth's static gravity field, (trend, and annual oscillation)	Internal GRACE+GOCE 2017	GOCO06s[1]
Dealiasing	AOD1B RL06[2]	AOD1B RL06[2]
Sub-monthly Hydrology	LSDM[3]	LSDM[3]
Astronomical tides (moon, sun, planets)	JPL DE421[4]	JPL DE432
Solid earth tides	IERS2010[5]	IERS2010[5]
Ocean tides	FES2014b[6] + GRACE estimates	FES2014b[6] + updated GRACE estimates
Atmospheric tides	van Dam-Ray[7]	AOD1B RL06[2]
Pole tides	IERS2010[5]	IERS2010[5]
Ocean pole tides	Desai2004[8]	Desai2004[8]
Non-conservative forces	ACC1B	In-house ACT1B (Ch. 6)
Relativistic corrections	IERS2010[5]	IERS2010[5]

[1] Kvas et al. (2021) [2] Dobslaw et al. (2017) [3] Dill (2008) [4] Folkner et al. (2009) [5] Petit and Luzum (2010) [6] Carrere et al. (2015) [7] van Dam and Ray (2010) [8] Desai (2002)

modeled by an autoregressive (AR) process. Detailed description and implementation of this approach are given by Kvas et al. (2019).

Next to gravity parameters, additional calibration parameters are also estimated to mitigate the systematic errors of the instruments. The source of these errors can be miscalibration or imperfect performance of the instruments, as well as changes in the environment which may affect the measurement process. To reduce the effect of the systematic errors, their pattern is parameterized with a deterministic function and the corresponding parameters are co-estimated together with the gravity parameters.

The K-Band ranging system is also subject to systematic errors. In the previous release, only co-estimated corrections applied to these measurements were the KBR antenna phase centre (APC) variations (Ellmer, 2018). By an empirical approach described in Chapter 4, this scheme has been revisited to mitigate additional errors, detected by analyzing the post-fit residuals. These errors include disturbances due to the eclipse transition of the satellites and the Sun intrusions into one of the star cameras of GRACE-A, also studied by Harvey et al. (2017a) and Goswami et al. (2018). More details on this subject can be found in Chapter 4 and 5.

Besides the systematic errors, the GRACE observations are also contaminated with stochastic noise. To obtain minimum variance estimators of the gravity parameters, a proper stochastic model of the observations is required. ITSG-Grace2018 processing scheme assumes that the observation groups are not cross-correlated. Subsequently, an individual covariance matrix for each group of observation is determined. Similar to the previous release, the noise process for kinematic orbits and range rates is assumed to be wide-sense stationery (van Etten, 2006). This means that the auto-covariance function, or equivalently the Power Spectrum Density (PSD) of the noise signal remains constant during a month. An additional variance factor is also introduced for 3-hour sub-daily arcs to account for noise variability. Instead of introducing a priori information, the PSD and the arc-wise variances are estimated from the observation themselves in an iterative adjustment using the approach of Variance Component Estimation (VCE; Koch and Kusche, 2002; Mayer-Gürr, 2006). The same technique is also applied to estimate the relative accuracies for the combination of the different groups of observations.

In ITSG-Grace2018, in addition to the stationary noise in range rate observations which is originated from the measurement system, a pre-computed nonstationary model is introduced, accounting for the emerging noise from the KBR antenna offset correction (AOC). This model is developed through the propagation of the satellite orientation uncertainties to AOC and has proven to be complementary to the purely stationary model in describing the complete noise behavior. The details of the stochastic models are described by Ellmer (2018), to which the reader is addressed for further information.

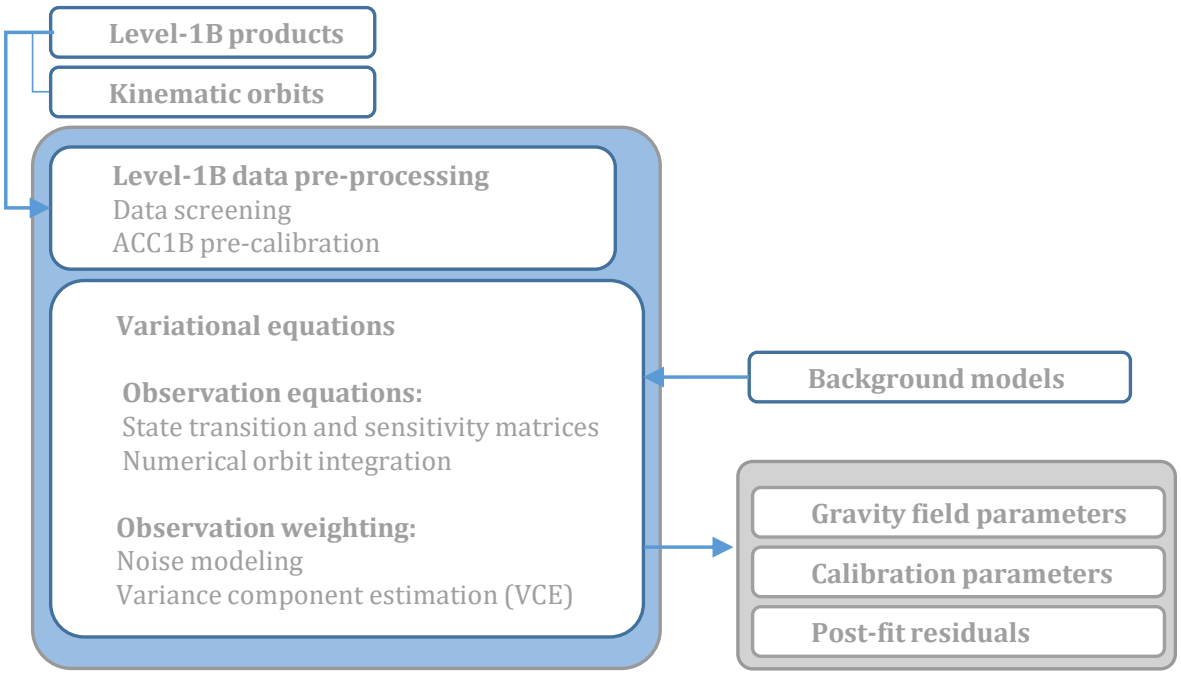

Figure 2.4.: Schematic overview of the ITSG-Grace2018 processing chain.

Using the final stochastic model, the full system of normal equations for each month are assembled. Afterward, the accumulated normal equations are solved to estimate monthly gravity coefficients, spanning from degree 2 up to 120. Figure 2.4 shows a schematic overview of the ITSG-Grace2018 processing chain.

Mathematical background and basic concepts

3

This chapter will give a short overview of the most important physical and mathematical concepts used throughout this dissertation. This includes the basic equations describing the Earth's gravity field (Section 3.1) and non-gravitational forces (Section 3.2). This is followed by the principles of least squares adjustment (Section 3.3) applied for gravity field recovery. Further, the temporal representations and the basic concept of time-frequency analysis applied in this research are also introduced in Section 3.4 and Section 3.5, respectively.

3.1. Earth's gravity field

GRACE satellite's orbit is affected by summation of different gravitational and non-gravitational forces. The primary gravitational force is caused by the Earth's gravitational potential. Other gravitational forces, the so-called background models also influence the orbit of the satellites. In order to study the Earth's gravity field and its variation, the accelerations caused by the following gravitational forces are modeled and reduced from the observations:

Direct tides The satellites' orbits are directly influenced by gravitational forces from third bodies, primarily the Sun and the Moon. The corresponding acceleration is derived by using a description of the third body's position in celestial coordinates, i.e. an ephemeris.

Solid Earth tides Direct tidal forces also cause deformation and mass variations within the Earth, which, in turn, have secondary tidal effects on the satellite orbit.

Ocean Tides Another secondary tidal effect is the mass variation in the ocean, which consequently cause gravitational variations. The ocean tide is modeled based on spherical harmonics with several constituents with long period, diurnal, semi-diurnal, and quarter-diurnal cycles.

Atmosphere tides In addition to ocean, direct tides also cause global-scale periodic mass variation in the atmosphere.

Solid earth and ocean pole tide Polar motion, which is the change in the Earth's rotation w.r.t its solid body, results in changes of the centrifugal force. This contributes to mass variation in the solid Earth as well as the oceans.

For more detailed description of the tidal and other gravitational forces, the reader is referred to the International Earth Rotation and Reference System Service (IERS) conventions (Petit & Luzum, 2010).

Earth's gravitational potential is commonly modeled with a truncated series expansion of spherical harmonics (SH) coefficients,

$$V(r,\lambda,\theta) = \frac{GM}{R}\sum_{n=0}^{N}\left(\frac{R}{r}\right)^{n+1}\sum_{m=0}^{n}\left[c_{nm}C_{nm}\left(\lambda,\theta\right) + s_{nm}S_{nm}\left(\lambda,\theta\right)\right], \tag{3.1.1}$$

where r, λ, and θ are the satellite distance, latitude, and longitude in an Earth-fixed coordinate system, respectively. G is the universal constant of gravitation. R and M are the Earth's radius and mass, respectively. c_{nm} and s_{nm} are the normalized SH coefficients of degree n and order m, and $C_{nm}\left(\lambda,\theta\right)$ and $S_{nm}\left(\lambda,\theta\right)$ are base functions of the 4π-normalized Legendre polynomials $\bar{P}_{nm}\left(\cos\theta\right)$,

$$C_{nm}\left(\lambda,\theta\right) = \cos\left(m\lambda\right)\bar{P}_{nm}\left(\cos\theta\right), \tag{3.1.2}$$

$$S_{nm}\left(\lambda,\theta\right) = \sin\left(m\lambda\right)\bar{P}_{nm}\left(\cos\theta\right). \tag{3.1.3}$$

The resolution of a spherical harmonic model the depends on the highest degree and order of the model N and is defined as half of the shortest representable wavelength

$$\psi_{min} = \frac{\pi R}{N} \approx \frac{20000\ km}{N}, \tag{3.1.4}$$

where ψ_{min} is the resolution in km and R is the Earth's radius. Equation (3.1.4) defines the formal resolution, whereas the real resolution of the gravity field models depends on the techniques and the data used to determine the models. The gravitational attraction $\boldsymbol{g}$ due to Earth's gravitational potential V is defined as

$$\boldsymbol{g}(r,\lambda,\theta) = \nabla V(r,\lambda,\theta). \tag{3.1.5}$$

3.1.1. Degree amplitudes

A common way to evaluate different gravity field models is to compare their signal degree amplitudes and variances. The signal amplitudes, describing the energy content of the gravity signal per SH degree n, is defined as the square root of the degree variances

$$\sigma_n = \sqrt{\sum_{m=0}^{n}\left(c_{nm}^2 + s_{nm}^2\right)}, \tag{3.1.6}$$

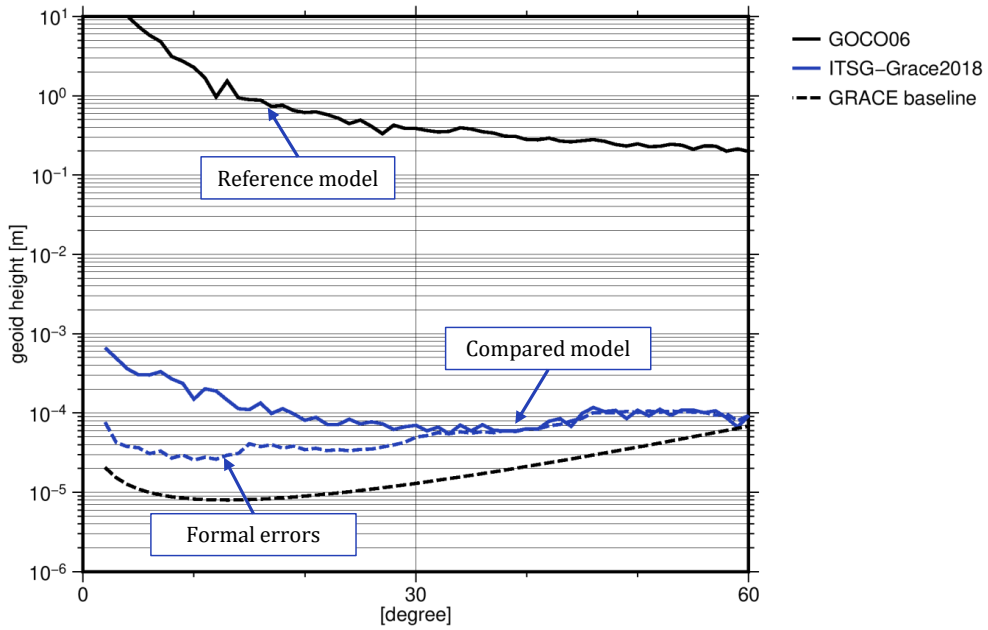

Figure 3.1.: Degree amplitudes of an arbitrary monthly gravity field model from ITSG-Grace2018, compared with a reference model (GOCO06).

and the error degree amplitudes or formal errors are given by

$$\hat{\sigma}_n = \sqrt{\sum_{m=0}^{n} (\sigma_{nm}^2 + \sigma_{nm}^2)}, \tag{3.1.7}$$

where σ_{nm}^2, σ_{nm}^2 are the error estimates of SH coefficients. To compare two arbitrary gravity field models, the difference degree amplitude, with Δc_{nm} and Δs_{nm} can be computed:

$$\Delta\sigma_n = \sqrt{\sum_{m=0}^{n} (\Delta c_{nm}^2 + \Delta s_{nm}^2)}\ . \tag{3.1.8}$$

Figure 3.1 shows an reference gravity signal (GOCO06; Kvas et al., 2021) and its difference degree amplitudes from an arbitrary monthly model, ITSG-Grace2018 December 2018. It also shows the GRACE baseline, a pre-launch estimate of the expected accuracy for GRACE monthly gravity field solutions (Kim & Tapley, 2002).

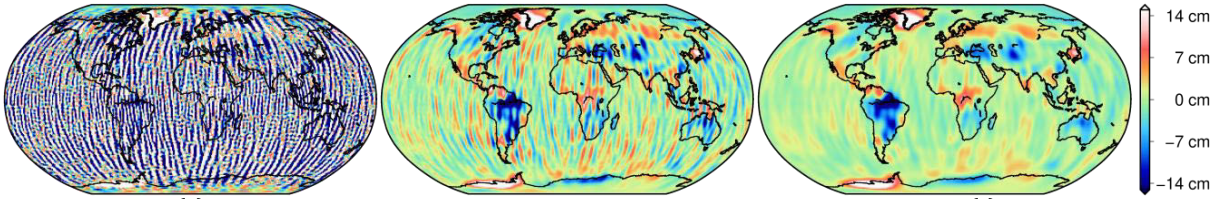

Figure 3.2.: Gaussian filtered EWHs for ITSG-Grace2018 December 2008 solution ($N = 120$) w.r.t GOCO06 with (a) 200, (b) 300, and (c) 400 km radii.

3.1.2. Spatial representation

The differences of monthly gravity field models are also investigated in the spatial domain in terms of equivalent water height (EWH; Wahr et al., 1998). Differences of monthly solutions are assumed to be caused by water redistributions, as the most of the other disturbances such as tidal effects are modelled and removed from the measurements. Therefore, the EWH values are mainly used to interpret the differences of monthly solutions w.r.t a reference field,

$$\Delta EWH(r,\lambda,\theta) = \frac{M}{4\pi R^2 \rho_w} \sum_{n=0}^{N} \sum_{m=0}^{n} \frac{1+k'_n}{2n+1} \left[c_{nm} C_{nm}(\lambda,\theta) + s_{nm} S_{nm}(\lambda,\theta) \right], \quad (3.1.9)$$

where ρ_w is the density of water and k' is the degree-wise load love number, describing the deformation induced by surface mass variations.

One of the major problems with GRACE gravity field models is the increasing error spectrum at higher degrees. These errors are mainly caused by the instrumental noise, temporal aliasing due to the unmodeled short-term mass variations (Dobslaw et al., 2017), and the anisotropic spatial sampling of the mission. In the spatial representation, these errors appear as a nonphysical north-south striping pattern, the so-called meridional strips. In order to reduce the strips, a common spatial smoothing technique by Gaussian function can be applied (Jekeli, 1981). This technique is based on multiplying all spherical harmonic coefficients by a predefined filtration factor. This factor is determined by the filter radius r. The larger this factor is, the more it dampens the noise as well as the geophysical information contained in higher degree coefficients, as shown in Figure 3.2.

3.2. Non-gravitational forces

GRACE satellites are categorized as low-Earth-orbiting (LEO) satellites. The non-gravitational accelerations acting upon LEO satellites are mainly due to atmospheric

Table 3.1.: LEO satellite non-gravitational forces.

Description	magnitude	reference
Atmospheric drag	$\sim 1 - 10^5$ nm/s^2	Vokrouhlicky et al. (1994)
Solar radiation pressure	~ 30 nm/s^2	Fliegel and Gallini (1996)
Earth radiation pressure	~ 10 nm/s^2	Rodriguez-Solano et al. (2011)

drag, solar radiation pressure (SRP), and earth radiation pressure (ERP), with their approximate magnitudes mentioned in Table 3.1. To model these effects for GRACE/GRACE-FO, the satellites' geometry and surface properties are required, which are obtained from the satellite's macro model (Case et al., 2010; Wen et al., 2019). The macro model simplifies the shape of the satellite into 9 panels, as shown in Figure 3.3, and describes the geometry and optical properties of each panel. These properties are described in Section 3.2. For each panel, the area, the normal vector in the SRF, and surface emissivity (Emiss), absorptivity (Absorp), as well as reflectivity (Refl) coefficients are reported.

In the following, the acceleration modeling is described for one individual surface element of the macro model. The total non-gravitational acceleration acting upon a satellite is the summation of all the described accelerations over the total surface elements of that satellite.

3.2.1. Atmospheric drag

Aerodynamic force is the force acting on the satellite's surface caused by interchange of momentum with the atmosphere molecules. For LEO satellites, it is the dominant non-gravitational perturbation. The aerodynamic force is modeled as:

$$\boldsymbol{a}_{aero,i} = -\frac{1}{2}\frac{A_i}{m}\boldsymbol{C}_{a,i}\rho \left\|\boldsymbol{v}_{TAS}\right\|^2, \tag{3.2.1}$$

depending on the dimensionless aerodynamic coefficient $\boldsymbol{C}_{a,i}$, the atmospheric density ρ, the cross-sectional area A_i, the satellite mass m, and the true airspeed $\boldsymbol{v}_{TAS}$, i.e. the velocity of the spacecraft relative to the atmosphere in satellite reference frame. Here, the cross-sectional area is obtained from the macro model. For GRACE, the mass of the satellite can be obtained from MAS1B products, but for GRACE-FO satellites, this variable is set to their launch mass values, as the MAS1B data product currently report the tank mass, and not the total mass. Therefore, for the purpose of simplification, this variation can be neglected.

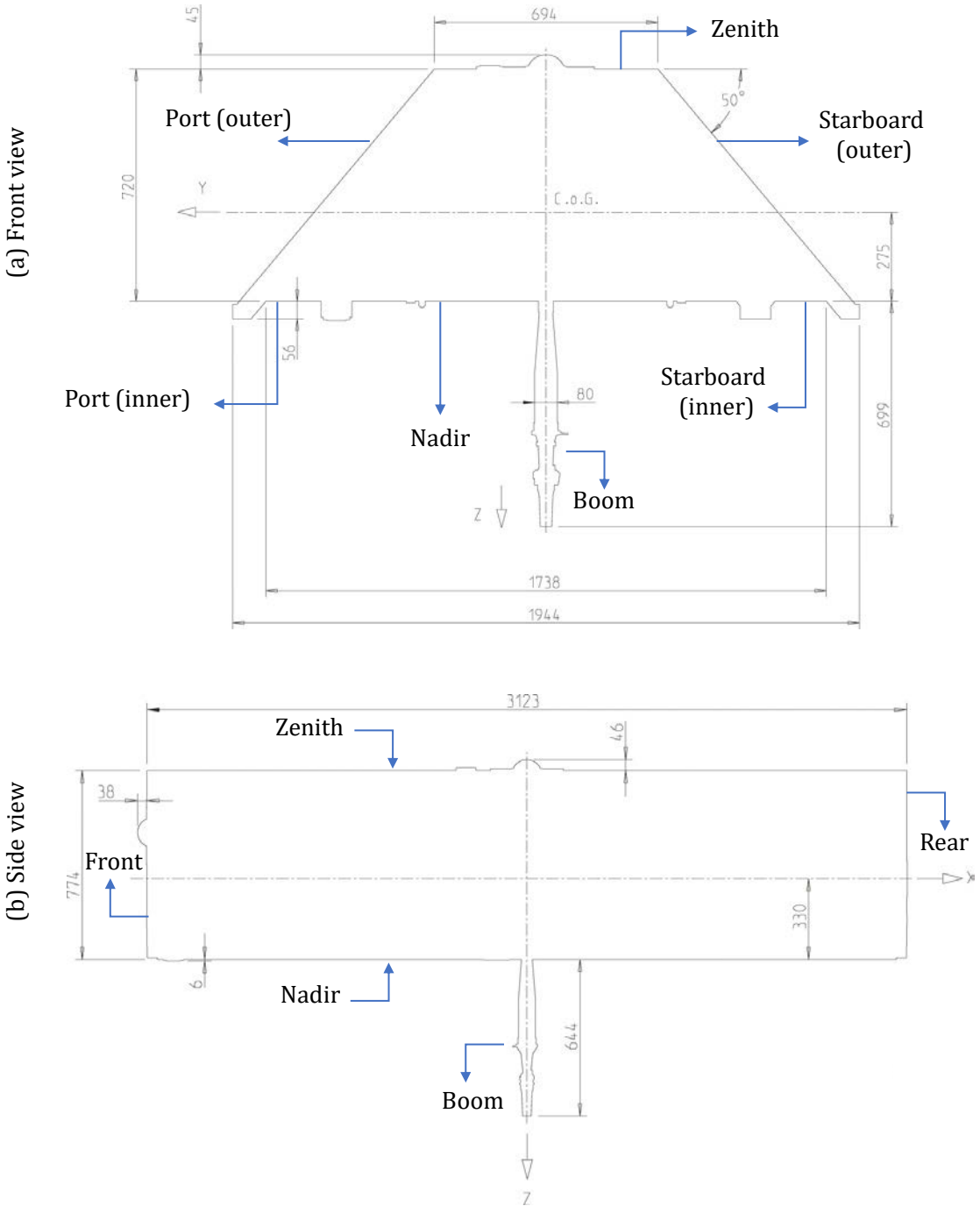

Figure 3.3.: GRACE/GRACE-FO macro model shown in front view (a) and side view (b), Source: Bettadpur (2012).

Table 3.2.: GRACE/GRACE-FO surface properties (Bettadpur, 2012).

Panel	Area (m^2)	Normal	Emiss (IR)	Absorp (Vis)	Refl (Vis, Geom)	Refl (Vis, Diff)	Refl (IR, Geom)	Refl (IR, Diff)
Front	0.96	$\begin{bmatrix}+1.00\\+0.00\\+0.00\end{bmatrix}$	0.62	0.34	0.40	0.26	0.23	0.15
Rear	0.96	$\begin{bmatrix}-1.00\\+0.00\\+0.00\end{bmatrix}$	0.62	0.34	0.40	0.26	0.23	0.15
Starboard (outer)	3.16	$\begin{bmatrix}+0.00\\+0.77\\-0.64\end{bmatrix}$	0.81	0.65/0.72*	0.05	0.30	0.03	0.16
Starboard (inner)	0.23	$\begin{bmatrix}+0.00\\-0.77\\+0.64\end{bmatrix}$	0.62	0.34	0.40	0.26	0.23	0.15
Port (outer)	3.16	$\begin{bmatrix}+0.00\\-0.77\\-0.64\end{bmatrix}$	0.81	0.65/0.72*	0.05	0.30	0.03	0.16
Port (inner)	0.23	$\begin{bmatrix}+0.00\\+0.77\\+0.64\end{bmatrix}$	0.62	0.34	0.40	0.26	0.23	0.15
Nadir	6.07	$\begin{bmatrix}+0.00\\+0.00\\+1.00\end{bmatrix}$	0.75	0.12	0.68	0.20	0.19	0.06
Zenith	2.17	$\begin{bmatrix}+0.00\\+0.00\\-1.00\end{bmatrix}$	0.81	0.65/0.72*	0.05	0.30	0.03	0.16
Boom	0.046	–	0.62	0.34	0.40	0.26	0.23	0.15

*0.65 for active solar panel and 0.72 for non-operating panel.

For atmospheric density, there exist several models, such as the Jacchia-Bowman 2008 (JB2008; Bowman et al. (2008)), and the Drag Temperature Model 2013 (DTM2013; Bruinsma, 2015), and the NRLMSISE-02 (Emmert et al., 2021). For modeling the drag force in this dissertation, which is exclusively carried out for GRACE-FO in Section 6.4.1, the NRLMSISE-00 model is used to obtain atmospheric density. This choice is based on the short delivery latency and the availability of real-time values.

The $\boldsymbol{v}_{TAS}$ is the relative velocity of the satellite w.r.t the atmosphere in satellite reference frame, which is the sum of inertial velocity of the satellite $\dot{\boldsymbol{r}}$, co-rotating atmosphere and atmospheric wind velocity $\boldsymbol{v}_w$:

$$\boldsymbol{v}_{TAS} = \dot{\boldsymbol{r}} - \boldsymbol{\omega}_E \times \boldsymbol{r} + \boldsymbol{v}_w, \tag{3.2.2}$$

where $\boldsymbol{r}$ is the satellite position and $\boldsymbol{\omega}_E$ is the angular velocity of the Earth sidereal rotation. The wind velocity is derived from Horizontal Wind Model 2014 (HWM14; Drob et al. (2015)). The position and velocity of the satellite are derived from dynamic orbit products which are initially reported in Terrestrial Reference Frame (TRF). The component of the aerodynamic force toward normal velocity direction $\hat{\boldsymbol{v}}_{TAS}$ is referred to as drag and the component toward $\frac{\hat{\boldsymbol{v}}_{TAS} \times \hat{\boldsymbol{n}}_i}{\|\hat{\boldsymbol{v}}_{TAS} \times \hat{\boldsymbol{n}}_i\|} \times \hat{\boldsymbol{v}}_{TAS}$ as lift, with $\hat{\boldsymbol{n}}_i$ being the unit normal vector to the satellite plate. Hence, the aerodynamic coefficient can be expressed by:

$$\boldsymbol{C}_{a,i} = C_D \parallel \hat{\boldsymbol{v}}_{TAS} + C_L \perp \hat{\boldsymbol{v}}_{TAS}. \tag{3.2.3}$$

Therein, C_D and C_L are dimensionless drag and lift coefficients, respectively. As drag is the major component of the aerodynamic force acting on satellites, neglecting lift and referring to drag force instead of aerodynamic force is conventional. Therefore, in this dissertation, the aerodynamic coefficient is referred to as drag coefficient, which is set to a constant value of 2.4 for GRACE satellites.

Due to uncertainties in the state and attitude of the satellite, interaction of the satellite's surface and atmosphere molecules affecting the drag coefficient, as well as uncertainties associated with atmospheric density models, it is not possible to model the drag force accurately. Therefore, the values used for density and drag coefficient play a significant role in drag model uncertainty (Moe & Moe, 2005; Prieto et al., 2014).

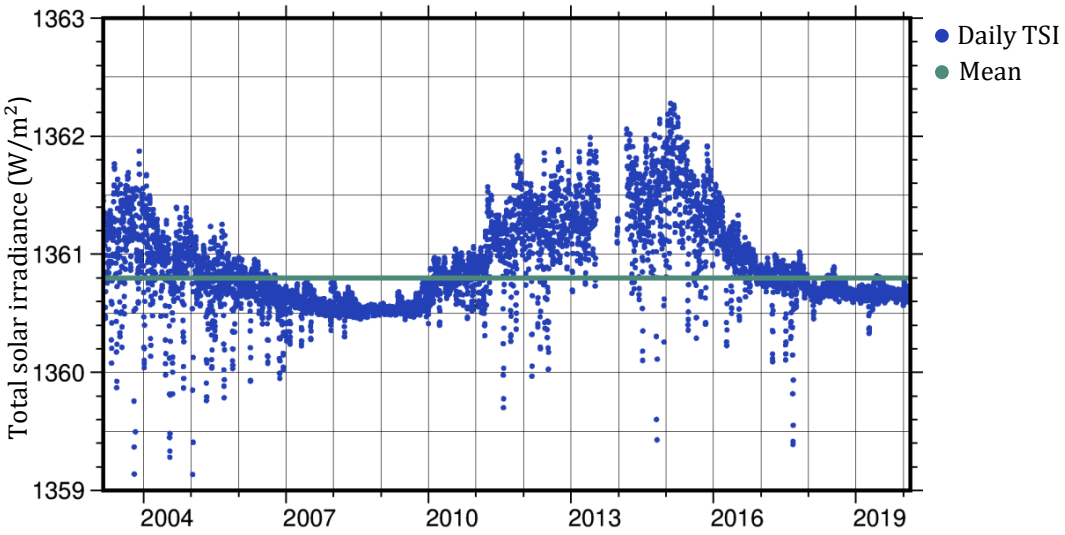

Figure 3.4.: The time series of daily total solar irradiance (TSI) observed by the Solar Radiation and Climate Experiment (SORCE) (Kopp & Lean, 2011).

3.2.2. Solar radiation pressure

Solar radiation pressure (SRP) is one of the major non-gravitational forces acting on a LEO satellite. Before introducing the corresponding acceleration, it is important to understand two main parameters which determine the amount of solar radiation exposed to the satellite: Total solar flux Φ and Shadow factor λ.

Total solar flux Φ

The incoming SRP $P_\odot$ at specific distance from the Sun $r_\odot$ is obtained from

$$P_\odot = \lambda \frac{1AU^2}{r_\odot^2} \Phi, \tag{3.2.4}$$

in which λ is the shadow function and Φ is the total solar irradiance (TSI) at one astronomical unit ($1AU = 149,597,870,700\ m$). Figure 3.4 shows daily TSI values based on the observations of the Solar Radiation and Climate Experiment (SORCE) satellite (Kopp & Lean, 2011) from 2003 to 2020. The relative small variation of TSI, which is only 0.1-0.2 percent, has insignificant effect on the incoming SRP. In this dissertation, for the purpose of simplification, the TSI variation is neglected and the mean value $\Phi \sim 1360.7\ \mathrm{W/m^2}$ is considered.

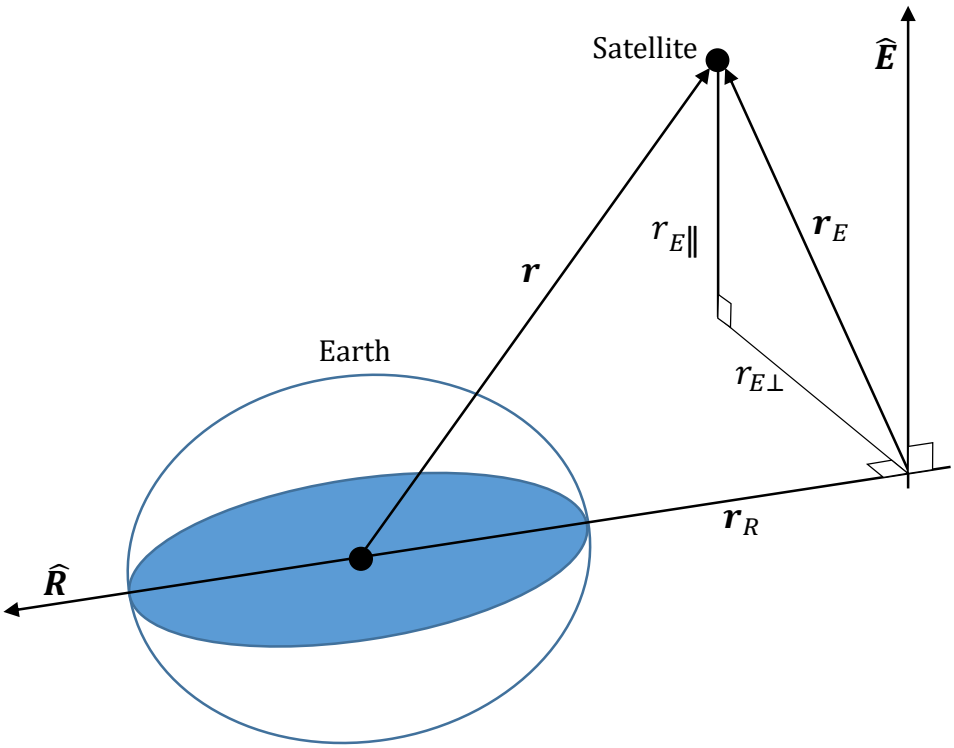

Figure 3.5.: The geometric parameters required for SOLAARS-CF shadow function. The satellite position $\mathbf{r}$ is projected towards Sun-Earth direction $\hat{\mathbf{R}}$ and the remaining component $\mathbf{r}_E$ is projected parallel and perpendicular to ecliptic normal vector $\hat{\mathbf{E}}$. The parallel component $r_{E\|}$ is then adjusted with oblateness scale factor. Figure is adapted from Robertson et al. (2015).

Shadow factor λ

The incoming $P_\odot$ is directly proportional to the degree of Sun exposure, which can be quantified with the shadow factor λ. λ determines whether the satellite is fully exposed to sunlight ($\lambda = 1$), is in Earth's shadow or umbra ($\lambda = 0$), or is in penumbra ($0 < \lambda < 1$). By neglecting oblateness and atmosphere effects and assuming a conical model, ($0 < \lambda < 1$) can be determined from the angular separation and diameters of Earth and Sun (e.g. Montenbruck and Gill (2000)).

For more realistic modeling, Robertson et al. (2015) proposed a physical model, denoted as SOLAARS model, which takes the influence of Earth's polar flattening and atmospheric effects such as sunlight scattering and refraction into account. Due to the complexity of the original model, Robertson et al. (2015) also provides the results of a curve fitting to the full SOLAARS model, which is called SOLAARS Curve Fit (SOLAARS-CF). This simplified model is defined by satellite position w.r.t the Sun, Earth, and the orbital plane of Earth, i.e. ecliptic, as described in Figure 3.5. This model

assumes zero axial tilt for the Earth, which results in mapped polar flattening in the ecliptic direction $\hat{\mathbf{E}}$. As shown in Figure 3.5, a number of geometry parameters are required for SOLAARS-CF model, which are defined as follows:

$\mathbf{r}$ is satellite position,
$\hat{\mathbf{R}}$ is the unit vector from Earth towards the Sun,
r_R is the projection of satellite position along $\hat{\mathbf{R}}$: $r_R = -\mathbf{r} \cdot \hat{\mathbf{R}}$,
$\mathbf{r}_E$ is the remaining component of satellite position after the projection along $\hat{\mathbf{R}}$: $\mathbf{r}_E = \mathbf{r} - \mathbf{r}_R$,
$r_{E\parallel}$ is the prependicular component of $\mathbf{r}_E$ to the ecliptic normal vector $\hat{\mathbf{E}}$,
$r_{E\perp}$ is the parallel component of $\mathbf{r}_E$ to the ecliptic normal vector $\hat{\mathbf{E}}$.

When computing shadow factor using SOLAARS-CF, the axial tilt of Earth is neglected. Therefore, to take the oblateness into account, r_E needs to be adjusted with a simple oblateness scaling factor:

$$r'_E = \sqrt{r_{E\perp}^2 + (s_O r_{E\parallel})^2}, \tag{3.2.5}$$

where r'_E is the adjusted distance and s_O is the ratio of Earth's equatorial radius to its polar radius. After computing the adjusted distance r'_E, the shadow function can be obtain from

$$\lambda = \frac{1 + a_1 + a_2 + a_1 \tanh(a_3(r'_E - a_4)) + a_2 \tanh(a_5(r'_E - a_6)) + \tanh(a_7(r'_E - a_8))}{2 + 2a_1 + 2a_2}, \tag{3.2.6}$$

where r'_E is in units of 10^6 meters, $a_1 - a_8$ are fit coefficients and are reported in Table 3.3. Throughout this dissertation, the SOLAARS-CF model is used to compute the shadow factor. Figure 3.6 compares GRACE-C shadow factors derived from the SOLAARS-CF model to the values derived from the conical model, revealing that the main differences can be seen during penumbra, with SALAARS-CF model showing up to 3 times longer transitions.

Corresponding acceleration

The SRP acceleration is caused by the interaction of the radiation flux of the Sun with the surface of satellite through three types of interaction: specular reflection, diffuse reflection, and absorption, as shown in Figure 3.7. According to Montenbruck and Gill

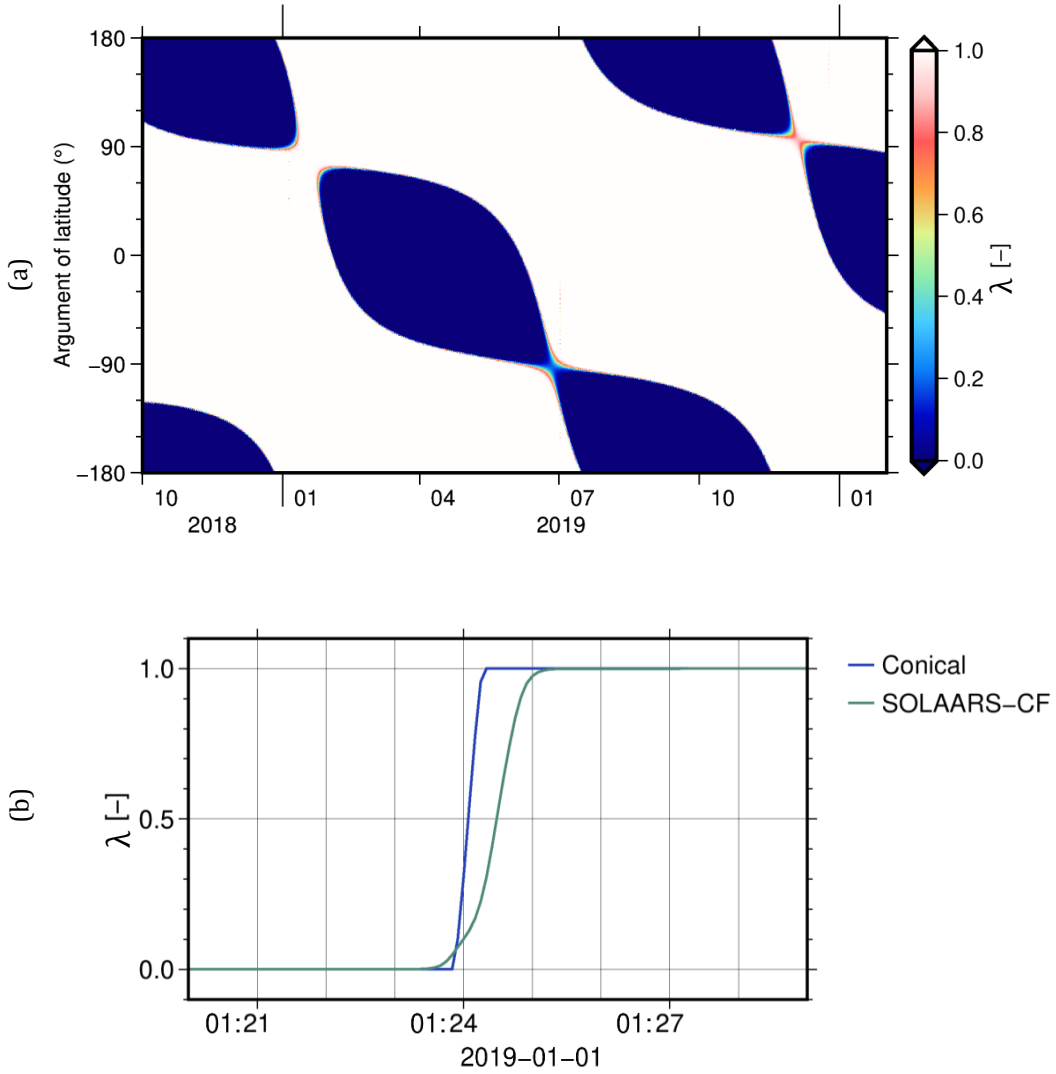

Figure 3.6.: (a) GRACE-C shadow function derived from SOLAARS-CF model w.r.t GRACE-C argument of latitude from 2018-10-01 to 2020-02-01 and (b) A comparison between shadow function time-series derived from the conical model and the SOLAARS-CF model in one shadow transition event on 2019-01-01.

Table 3.3.: SOLAARS-CF model coefficients as a function of r_R in units of 10^6 meters.

Formula	b_1	b_2	b_3	b_4
$a_1 = b_1 e^{b_2 r_R} + b_3 e^{b_4 r_R}$	0.1715	-0.1423	0.01061	-0.01443
$a_2 = b_1 r_R + b_2$	0.008162	0.3401	-	-
$a_3 = b_1 e^{b_2 r_R} + b_3 e^{b_4 r_R}$	260.9	-0.4661	27.81	-0.009437
$a_4 = b_1 {r_R}^{b_2} + b_3$	-0.006119	1.176	6.385	-
$a_5 = b_1 e^{b_2 r_R} + b_3 e^{b_4 r_R}$	87.56	-0.09188	19.30	-0.01089
$a_6 = b_1 r_R + b_2$	0.002047	6.409	-	-
$a_7 = b_1 e^{b_2 r_R} + b_3 e^{b_4 r_R}$	61.98	-0.1629	27.87	-0.02217
$a_8 = b_1 e^{b_2 r_R} + b_3 e^{b_4 r_R}$	6.413	-0.0002593	-0.01479	-0.1318

(2000), the radiation pressure $P_\odot$ causes an acceleration on a flat surface plate which can be calculated as:

$$\boldsymbol{a}_{srp,i} = -\frac{P_\odot}{mc} A_i \cos(\theta_i) \left[(c_{a,i} + c_{d,i}) \hat{\boldsymbol{e}}_\odot - 2 \left(\frac{c_{d,i}}{3} + c_{s,i} cos(\theta_i) \right) \hat{\boldsymbol{n}}_{\boldsymbol{i}} \right]. \tag{3.2.7}$$

In this equation c is the speed of light and θ_i is the incident angle between the direction from Sun to the satellite, $\hat{\boldsymbol{e}}_\odot$ and $\hat{\boldsymbol{n}}_{\boldsymbol{i}}$. The satellite properties such as the surface unit normal vector $\hat{\boldsymbol{n}}_{\boldsymbol{i}}$, the corresponding area A_i as well as the surface coefficients for absorption $c_{a,i}$, specular and diffuse reflectivity $c_{s,i}$ and $c_{d,i}$, respectively are taken from the satellite macro-model by Case et al. (2010) and Wen et al. (2019).

When a satellite's surface is exposed to any type of radiation, part of this radiation is being absorbed by the surface, depending on its absorption ratio $c_{a,i}$. By assuming that the total absorbed energy instantaneously re-radiates from the surface (Montenbruck et al., 2014) and according to Lambert's law, an additional term $\boldsymbol{a}_{rr}$ is added to eq. (3.2.8)):

$$\boldsymbol{a}_{rr,i} = -\frac{P_\odot}{mc} A_i \cos(\theta_i) \left[-\frac{2}{3} c_{a,i} \hat{\boldsymbol{n}}_{\boldsymbol{i}} \right]. \tag{3.2.8}$$

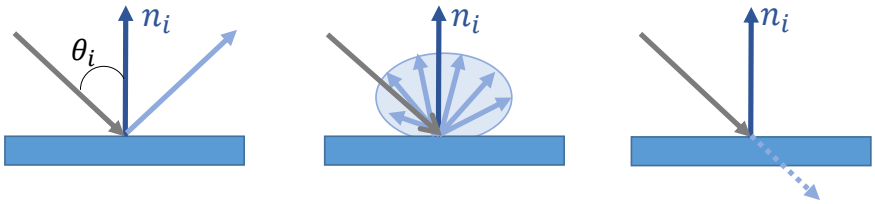

a) Specular reflection c_s b) Diffuse reflection c_d c) absorption c_a

Figure 3.7.: Three types interaction between incoming photons and a flat satellite's surface: (a) specular reflection, (b) diffuse reflection, and (c) absorption with their corresponding coefficients c_s, c_d, and c_a, respectively.

3.2.3. Earth radiation pressure

The Earth radiation pressure (ERP) is the force acting on the satellite's surface due to the shortwave visible radiation and longwave infrared radiation re-emitted by the Earth. The shortwave radiation $P_{\oplus,sw}$ is the reflected shortwave solar radiation by the Earth's surface or clouds. Therefore, the shortwave radiation pressure is only reflected by the daylight side of the Earth and may vary significantly depending on land, ocean, and atmosphere characteristics. On the contrary, the longwave part of the ERP $P_{\oplus,lw}$ is the absorbed and re-emitted portion of the received solar radiation by each Earth's surface element. These two radiation components can be approximately formulized as follows:

$$P_{\oplus,sw_k} = \frac{1}{\pi r_{sat,k}^2} \cos(\alpha_k)\delta_k P_{\odot,k} \cos(\phi_k)\Delta\Omega_k, \tag{3.2.9}$$

$$P_{\oplus,sw_k} = \frac{1}{4\pi r_{sat,k}^2} \cos(\alpha_k)\epsilon_k P_{\odot,k}\Delta\Omega_k, \tag{3.2.10}$$

The shortwave ERP from the Earth's surface element k depends on the surface area $\Delta\Omega_k$, incoming solar radiation pressure arriving at this element $P_{\odot,k}$, the angle of the incident solar radiation ϕ_k, which is the angle between the element normal vector and its direction to the Sun, the angle of the reflected radiation α_k, mean reflectivity of the element δ_k, and the distance to the satellite $r_{sat,k}$. In addition to the introduced parameters, the longwave ERP depends on the mean emissivity of the surface element ϵ_k.

In this dissertation, the mean reflectivity and emissivity of Earth's surface are obtained from monthly mean values based on the data provided by Clouds and Earth's Radiant Energy System (CERES) model from 2000 to 2009 (Rodriguez-Solano et al., 2011;

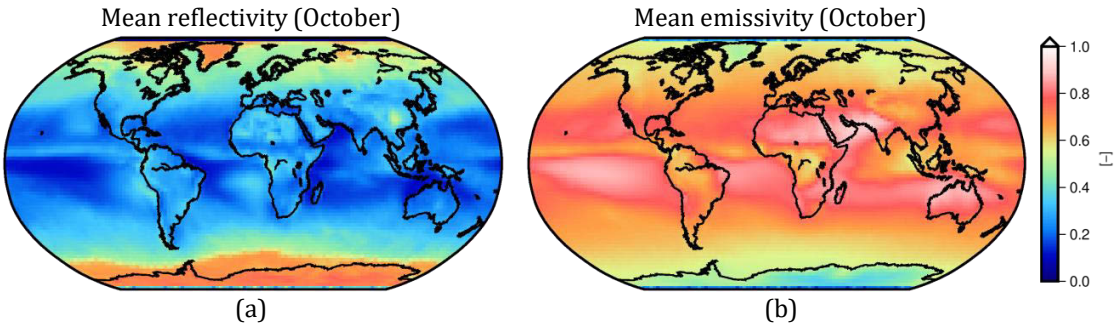

Figure 3.8.: (a) Mean reflectivity and (b) emissivity values for the month of October derived from CERES data (Rodriguez-Solano et al., 2011; Wielicki et al., 1996).

Wielicki et al., 1996). These values are constant for each month of the year and are provided in grids with a resolution of 2.5° × 2.5°. Figure 3.8 shows these grids for the month of October.

The resulting acceleration on a flat surface can be obtained according to

$$\boldsymbol{a}_{erp,sw_i} = \sum_k P_{\oplus,sw_k} \frac{A_i}{m} \cos(\theta_i) \left[c_{a,i} \hat{\boldsymbol{e}}_{\oplus} - 2 \left(\frac{c_{a,i} + c_{d,i}}{3} + c_{s,i} cos(\theta_i) \right) \hat{\boldsymbol{n}}_{\boldsymbol{i}} \right], \quad (3.2.11)$$

$$\boldsymbol{a}_{erp,lw_i} = \sum_k P_{\oplus,lw_k} \frac{A_i}{m} \cos(\theta_i) \left[c_{a,i} \hat{\boldsymbol{e}}_{\oplus} - 2 \left(\frac{c_{a,i} + c_{d,i}}{3} + c_{s,i} cos(\theta_i) \right) \hat{\boldsymbol{n}}_{\boldsymbol{i}} \right]. \quad (3.2.12)$$

3.3. Least squares adjustment

The method of least squares (LSM) or least squares adjustment (LSA), also known as the Gauss-Markov model, is the most frequently used technique for determining parameters in geodesy. It is used to find the optimal estimated values of the unknown parameters $\boldsymbol{x}$ in an overdetermined system, meaning that there are more observations $\boldsymbol{l}$ than unknowns $\boldsymbol{x}$. In the following, an overview of the method is described, which can be found in details in Koch (1999).

Starting from a linearized system, the aim is to find estimated values $\hat{\boldsymbol{x}}$ w.r.t some initial values $\boldsymbol{x}_0$ for the true values $\boldsymbol{x}$ that are linked to the observations through a functional relationship $f(\boldsymbol{x})$. The measured observations are a sum of the model function $f(\boldsymbol{x})$ and an error term $\boldsymbol{e}$. The observation errors are assumed to be normally distributed and free from systematic errors and the variance-covariance matrix of the

observations $\boldsymbol{\Sigma}_{ll}$ is assumed to be known. With these assumption, an equation system is set up

$$\Delta \boldsymbol{l} = \boldsymbol{A}\Delta \boldsymbol{x} + \boldsymbol{e}, \tag{3.3.1}$$

where $\Delta \boldsymbol{l} = \boldsymbol{l} - f(\boldsymbol{x}_0)$ is the reduced observation vector, and $\boldsymbol{A}$ is the design matrix, representing the partial derivatives of the function $f(\boldsymbol{x})$ w.r.t the parameters. Given a matrix of observation weights $\boldsymbol{P} = \boldsymbol{\Sigma}_{ll}^{-1}$, if $\boldsymbol{A}^{\mathsf{T}}\boldsymbol{P}\boldsymbol{A}$ is invertible, the least squares solution of eq. (3.3.1) is

$$\Delta \hat{\boldsymbol{x}} = \left(\boldsymbol{A}^{\mathsf{T}}\boldsymbol{P}\boldsymbol{A}\right)^{-1}\boldsymbol{A}^{\mathsf{T}}\boldsymbol{P}\Delta \boldsymbol{l}, \tag{3.3.2}$$

and the estimated residuals of the observations are

$$\hat{\boldsymbol{e}} = \boldsymbol{l} - \boldsymbol{A}\hat{\boldsymbol{x}}. \tag{3.3.3}$$

eq. (3.3.2) can be rewritten as

$$\boldsymbol{N}\Delta \hat{\boldsymbol{x}} = \boldsymbol{n} \tag{3.3.4}$$

with $\boldsymbol{N}$ being the normal equation of the system

$$\boldsymbol{N} = \boldsymbol{A}^{\mathsf{T}}\boldsymbol{P}\boldsymbol{A}, \tag{3.3.5}$$

and $\boldsymbol{n}$ being the right hand side

$$\boldsymbol{n} = \boldsymbol{A}^{\mathsf{T}}\boldsymbol{P}\boldsymbol{l}. \tag{3.3.6}$$

Additionally, one can obtain the variance-covariance matrix of the estimated parameters from

$$\hat{\boldsymbol{\Sigma}}_{\hat{\boldsymbol{x}}\hat{\boldsymbol{x}}} = \boldsymbol{N}^{-1}. \tag{3.3.7}$$

3.3.1. Decorrelation

The weight matrix $\boldsymbol{P}$ of the observations is usually assumed to be the inverse form of the covariance matrix $\boldsymbol{P} = \boldsymbol{\Sigma}_{ll}^{-1}$. The direct calculation of the inverse should be avoided as it is computationally expensive and numerically unstable (Björck, 1996). If the matrix is positive definite, the Cholesky decomposition exists

$$\boldsymbol{\Sigma}_{ll} = \boldsymbol{W}^{\mathsf{T}}\boldsymbol{W}, \tag{3.3.8}$$

with $\boldsymbol{W}$ being an upper triangular matrix. The decomposition has the advantage that for eq. (3.3.2) the inverse computation can be avoided by substituting eq. (3.3.8)

$$\hat{\boldsymbol{x}} = \left(\boldsymbol{A}^{\mathsf{T}}\boldsymbol{W}^{-1}\boldsymbol{W}^{-\mathsf{T}}\boldsymbol{A}\right)^{-1}\boldsymbol{A}^{\mathsf{T}}\boldsymbol{W}^{-1}\boldsymbol{W}^{-\mathsf{T}}\boldsymbol{l}. \tag{3.3.9}$$

With the transformation

$$\bar{\boldsymbol{A}} = \boldsymbol{W}^{-\mathsf{T}}\boldsymbol{A}\,, \qquad \bar{\boldsymbol{l}} = \boldsymbol{W}^{-\mathsf{T}}\boldsymbol{l}, \tag{3.3.10}$$

the normal equation matrices can be re-written as

$$\boldsymbol{N} = \boldsymbol{A}^{\mathsf{T}}\boldsymbol{P}\boldsymbol{A} = \bar{\boldsymbol{A}}^{\mathsf{T}}\bar{\boldsymbol{A}}\,, \qquad \boldsymbol{n} = \boldsymbol{A}^{\mathsf{T}}\boldsymbol{P}\boldsymbol{l} = \bar{\boldsymbol{A}}^{\mathsf{T}}\bar{\boldsymbol{l}}. \tag{3.3.11}$$

This means that the transformed system can be interpreted as an LSA from uncorrelated observations

$$\hat{\boldsymbol{x}} = \left(\bar{\boldsymbol{A}}^{\mathsf{T}}\bar{\boldsymbol{A}}\right)^{-1}\bar{\boldsymbol{A}}^{\mathsf{T}}\bar{\boldsymbol{l}}. \tag{3.3.12}$$

For this reason, this transformation is also called decorrelation and homogenization. Accordingly, the uncorrelated residuals $\bar{\boldsymbol{e}}$ can be computed from

$$\bar{\boldsymbol{e}} = \bar{\boldsymbol{l}} - \bar{\boldsymbol{A}}\hat{\boldsymbol{x}}. \tag{3.3.13}$$

3.3.2. Parameter elimination

For a given a normal equation system $\boldsymbol{N}\hat{\boldsymbol{x}} = \boldsymbol{n}$, it can be useful to solely estimate the parameters of interest $\hat{\boldsymbol{x}}_1$ and eliminate other parameter groups $\hat{\boldsymbol{x}}_2$, e.g. to reduce the processing cost. The normal equation system can be separated as

$$\begin{bmatrix} \boldsymbol{N}_{11} & \boldsymbol{N}_{12} \\ \boldsymbol{N}_{12}^{\mathsf{T}} & \boldsymbol{N}_{22} \end{bmatrix} \begin{bmatrix} \hat{\boldsymbol{x}}_1 \\ \hat{\boldsymbol{x}}_2 \end{bmatrix} = \begin{bmatrix} \boldsymbol{n}_1 \\ \boldsymbol{n}_2 \end{bmatrix}. \tag{3.3.14}$$

Solving the second equation for $\hat{\boldsymbol{x}}_2$ and substituting the solution into eq. (3.3.14) gives a new set of normal equations $\boldsymbol{N}'\hat{\boldsymbol{x}}_1 = \boldsymbol{n}'$, with

$$\boldsymbol{N}' = \boldsymbol{N}_{11} - \boldsymbol{N}_{12}\boldsymbol{N}_{22}^{-1}\boldsymbol{N}_{12}^{\mathsf{T}} \qquad \text{and} \qquad \boldsymbol{n}' = \boldsymbol{n}_1 - \boldsymbol{N}_{12}\boldsymbol{N}_{22}^{-1}\boldsymbol{n}_2\,. \tag{3.3.15}$$

The system eq. (3.3.15) gives the same solution for $\hat{\boldsymbol{x}}_1$ as eq. (3.3.14). Solving for $\hat{\boldsymbol{x}}_1$ in this manner can be advantageous, depending on the structure and size of the initial normal equation system.

3.3.3. Variance component estimation

When determining the gravitational field, different observation groups are often combined with different levels of accuracy to estimate the unknown parameters. In the GRACE mission, for example, the KBR measurements are used together with the kinematic orbits. For an optimal combination, the proper relative weighting between the observation groups is necessary. Following Koch and Kusche (2002), instead of using a priori information, the relative weighting of the observation groups can be determined iteratively from the estimation process using the method known as Variance Component Estimation (VCE). The normal equation of k uncorrelated observation groups $\boldsymbol{l}_k$ can be obtained from:

$$\boldsymbol{N} = \sum_k \frac{1}{\hat{\sigma}_k^2} \boldsymbol{N}_k = \sum_k \frac{1}{\hat{\sigma}_k^2} \boldsymbol{A}_k^\top \boldsymbol{P}_k \boldsymbol{A}_k, \tag{3.3.16}$$

and

$$\boldsymbol{n} = \sum_k \frac{1}{\hat{\sigma}_k^2} \boldsymbol{n}_k = \sum_k \boldsymbol{A}_k^\top \boldsymbol{P}_k \boldsymbol{l}_k. \tag{3.3.17}$$

Starting the least square adjustment with initial values for $\hat{\sigma}_k$, the estimated variance component for the observation group k is:

$$\hat{\sigma}_k = \frac{\Omega_k}{r_k}, \tag{3.3.18}$$

with

$$\Omega_k = \hat{\boldsymbol{e}}_k^\top \boldsymbol{\Sigma}_k^{-1} \hat{e}_k, \tag{3.3.19}$$

and

$$r_k = m_k - \frac{1}{\hat{\sigma}_k^2} trace(\boldsymbol{N}_k \boldsymbol{N}^{-1}). \tag{3.3.20}$$

Ω_k is the square sum of the residuals, r_k is the partial redundancy, m_k is the number of observations in the observation group k. For the next iterations, the estimated variance is used as the initial value, until convergence.

3.4. Temporal representations

This section explains how to efficiently represent time-series with a mathematical function. The most common approach is to introduce a set of basis functions and consider the time-series as weighted sum of these functions. The corresponding weights are then determined using least square adjustment. This section describes the temporal representation approaches which are used in this dissertation.

3.4.1. Uniform basic splines

B-spline curves are piece-wise polynomial functions (de Boor, 2001) that are recursively defined according to the degree of the splines n. Given a knot vector $\{\hat{t}_0, ..., \hat{t}_m\}$ with normalized time $\hat{t}_i \in [0, 1]$, the i-th B-spline basis function $N_{i,p}$ is defined recursively by:

For $p = 0$ and $0 \leq i \leq m - p - 1$:

$$N_{i,0}(\hat{t}) = \begin{cases} 1 & \hat{t}_i \leq \hat{t} < \hat{t}_{i+1} \\ 0 & else. \end{cases} \tag{3.4.1}$$

and for $p \geq 1$:

$$N_{i,p}(\hat{t}) = \frac{\hat{t} - \hat{t}_i}{\hat{t}_{i+p} - \hat{t}_i} N_{i,p-1}(\hat{t}) + \frac{\hat{t}_{i+p+1} - \hat{t}}{\hat{t}_{i+p+1} - \hat{t}_{i+1}} N_{i+1,p-1}(\hat{t}). \tag{3.4.2}$$

The elements of the knot vector are accordingly called knots. The knot vectors are divided into clamped and unclamped knot vectors. The difference is that in the clamped variant the endpoints appear multiple times. In the unclamped variant, however, only once. In addition, the knot vectors are divided into periodic, or uniform, and non-periodic, or non-uniform. The difference lies in the fact whether the inner knots are arranged equidistantly or not.

The number of splines on an interval is determined by the number of knots and the degree of splines. If $m + 1$ is the number of knots, then $n = m - p - 1$ is the number of B-spline basis functions of degree p (de Boor, 2001). B-spline curves have following important properties:

- End point interpolation: The end points lie on the curve.
- Affine invariance: Affine transformations such as rotations, displacements or scaling do not change the shape of the curve and only need to be applied on the control points.
- Convex hull property: Each point of the curve lies in the convex hull of the control polygon.

Figure 3.9 shows arbitrary B-spline basis functions of order 1, 2, 3 and 4.

3.4.2. Legendre polynomials

A time variable function can be represented by Legendre polynomials, a system of complete and orthogonal polynomials (Arfken et al., 2013). The Legendre polynomial P_n for $n = 0, 1, 2, ..$ is defined by:

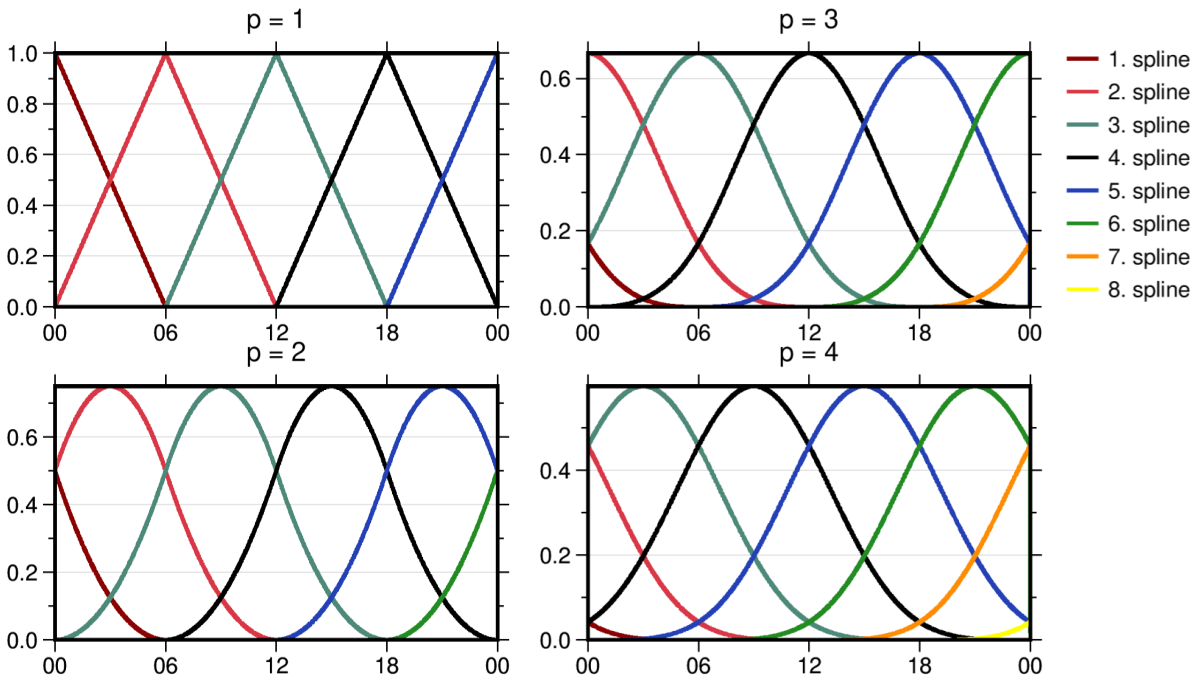

Figure 3.9.: B-spline basis functions of order 1, 2, 3, and 4 on a uniform knot vector with 6 hour sampling.

$$P_n(t) = \frac{1}{2^n} \sum_{k=0}^{n/2} \frac{(-1)^k (2n-2k)!}{k!(n-k)!(n-2k)!} \hat{t}^{n-2k}. \tag{3.4.3}$$

The P_n form an orthogonal set of polynomials on normalized time $\hat{t} \in [-1, 1]$. Figure 3.10 shows basis Legendre polynomials of degree 0, 1, 2, 3, and 4.

Given a series of $m+1$ values $x(t_0) \dots x(t_m)$, the time-series can be represented by:

$$x(t) = \sum_{k=0}^{n} a_k P_k(t). \tag{3.4.4}$$

Defining an adjustment problem, the associated parameters $\boldsymbol{a}$ can be obtained by solving the following system:

$$\underbrace{\begin{bmatrix} x(t_0) \\ \vdots \\ x(t_m) \end{bmatrix}}_{\boldsymbol{x}} = \underbrace{\begin{bmatrix} P_0(\hat{t}_0) & P_1(\hat{t}_0) & \cdots & P_n(\hat{t}_0) \\ \vdots & \vdots & \ddots & \vdots \\ P_0(\hat{t}_m) & P_1(\hat{t}_m) & \cdots & P_n(\hat{t}_m) \end{bmatrix}}_{\boldsymbol{A}} \underbrace{\begin{bmatrix} a_0 \\ \vdots \\ a_n \end{bmatrix}}_{\boldsymbol{a}}. \tag{3.4.5}$$

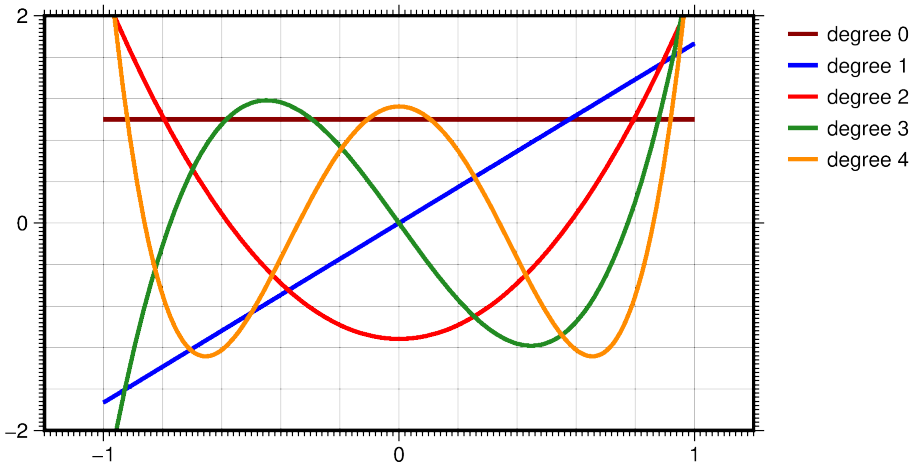

Figure 3.10.: Basis Legendre polynomials for $n = \{0, 1, 2, 3, 4\}$.

3.5. Temporal-spectral analysis

Representing a one-dimensional signal in the time domain shows the general amplitude and its variations as a function of time. However, to understand the signal's characteristics, a common practice is to study the signal in frequency domain by applying Fourier transform (Keller, 2004). Fourier transform decomposes a signal into the sum of sine and cosine wave components. The spectrum of frequency components is the frequency domain representation of the signal. This representation shows how the signal's energy is distributed over a range of frequencies. Using a pair of mathematical operators, a signal can be transformed to the time and/or frequency domains interchangeably.

The time and frequency domains highlight different properties in a signal. The frequency domain reveals the periodic properties, while the time domain is useful for detecting abrupt changes or transient periods. A fundamental limitation of the Fourier transform is that during the transformation process all temporal information would be lost. Therefore, it is not possible to localize and differentiate transient signals in the frequency domain.

3.5.1. Short-time Fourier trasform

To address the Fourier analysis limitations, time-frequency analysis is proposed to study a signal in both the temporal and frequency domains (Keller, 2004). One method of exploring both the temporal and frequency information is the Short Time Fourier Transform (STFT). The STFT divides a signal into shorter segments using a window

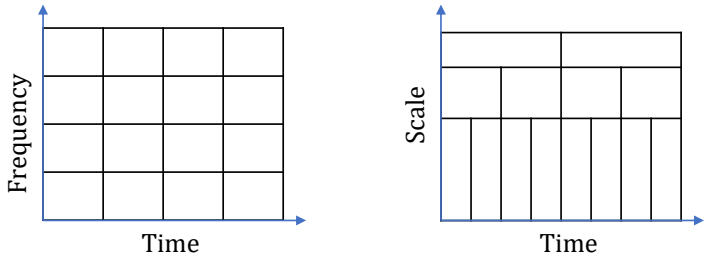

(a) STFT (b) DWT

Figure 3.11.: Comparison of the time-frequency resolution for (a) the STFT and (b) the discrete wavelet transform. In contrast to STFT, wavelet transform uses a window function that can dilate or contract, and this enables the details of the signal to be extracted based on their temporal properties.

function and then performs the Discrete Fourier Transform (DFT) for each segment,

$$STFT(\tau, \omega) = \int_{-\infty}^{\infty} f(t)h(t-\tau)e^{-i\omega t}\, dt, \tag{3.5.1}$$

where $h(t-\tau)$ is a window function, which is multiplied to the signal $f(t)$.

The main property of STFT is the altering the trade-off with the time and frequency resolutions by choosing a wider/shorter window. One can shorten the window to improve the temporal resolution, but this means that the frequency resolution reduces. Shorter windows can detect sudden changes in a signal but would not be able to analyze the lower frequency components of the signal. This is based on the Heisenberg's uncertainty principles (Busch et al., 2007), which states to gain resolution in one domain, one must lose resolution in the other. This is because the same time-frequency window that is used in the lower frequencies is also used in the higher frequencies. These fixed windows are either too large or too short to analyze the variety of frequencies that can exist in a signal.

3.5.2. Wavelet transform

Wavelet analysis improves on the STFT to provide better resolution in both domains by changing the time and frequency windows, as illustrated in Figure 3.11. The wavelet transform $Wf(u,s)$ of a signal $f(t)$ can be described as

$$Wf(u,s) = \langle f, \psi_{u,s} \rangle = \int_{-\infty}^{\infty} f(t) \frac{1}{\sqrt{s}} \bar{\psi} \left(\frac{t-u}{s} \right) \mathrm{d}t, \tag{3.5.2}$$

in which signal is convolved with a set of scaled and translated versions of a basis function called mother wavelet $\bar{\psi}$. In eq. (3.5.2), u is the translation parameter which localizes the wavelet in the time domain, and s is the scale parameter which localizes the wavelet in the frequency domain. Since u and s parameters are continuous values, there are an infinite number of coefficients in this transformation. This leads to a redundancy of information and increases the number of numerical operations. Therefore, generally, the discrete wavelets with discretized parameters are employed. The common practice is to use a J-scale dyadic discretization based on powers of two:

$$\psi(j,n) = 2^{-j/2}\bar{\psi}\left(\frac{t-n2^j}{2^j}\right); \quad j,n \in \mathbb{Z}. \tag{3.5.3}$$

The resulting transform is called Discrete Wavelet Transform (DWT):

$$d(j,n) = \sum_t f(t)\psi_{j,n}(t), \tag{3.5.4}$$

$$a(J,n) = \sum_t f(t)\phi_{J,n}(t), \tag{3.5.5}$$

with $\phi_{J,n}(t)$ being the scaling function, which is defined with the wavelet function $\psi(j,n)$. For signal $f(t)$ with sampling frequency of F_s, the discrete wavelet coefficients $d(j,n)$ decompose the signal into detail subsignals at the scale 2^j ($1 \leq j \leq J$) and an approximation subsignal $a(J,n)$. Using the J-scale dyadic discretization, each detail subsignal corresponds to the frequency interval $[F_s/2^{j+1}, F_s/2^j]$. The approximation of the signal at the scale J also corresponds to the frequency interval $[0, F_s/2^{J+1}]$.

In an inverse discrete wavelet transformation, the original signal is reconstructed back by adding all the detail subsignals as well as the approximation subsignal:

$$f(t) = \sum_n a(J,n)\phi_{J,n}(t) + \sum_{j\leq J}\sum_n d(j,n)\psi_{j,n}(t). \tag{3.5.6}$$

Mallat (1989) developed an efficient method to calculate DWT for a discrete signal $f[n]$, connecting any DWT orthonormal basis with a particular class of digital filters, the conjugate mirror filters. He introduced the Fast discrete Wavelet Transform (FWT) by implementing a pair of conjugate mirror filters, associated with a specific mother wavelet:

$$h[n] = \left\langle \frac{1}{\sqrt{2}}\bar{\phi}\left(\frac{t}{2}\right), \bar{\phi}(t-n)\right\rangle, \tag{3.5.7}$$

$$g[n] = \left\langle \frac{1}{\sqrt{2}} \bar{\psi}\left(\frac{t}{2}\right), \bar{\phi}(t-n) \right\rangle, \tag{3.5.8}$$

where $h[n]$ and $g[n]$ are lowpass and highpass filters in the associated filter pair, respectively. Using the FWT approach, eq. (3.5.5) and eq. (3.5.5) turn into the convolution of the highpass and lowpass filters with the discrete signal. This filtering process is accompanied by a factor two down-sampling of the input signal to cancel the aliasing between the resulting coefficients (Vetterli & Herley, 1992),

$$d[p] = \sum_{n=-\infty}^{\infty} g[n-2p] f[n] = f * \bar{g}[2p]. \tag{3.5.9}$$

$$a[p] = \sum_{n=-\infty}^{\infty} h[n-2p] f[n] = f * \bar{h}[2p], \tag{3.5.10}$$

where the coefficients a are called the approximation of the first level decomposition, also referred to as low-pass output. Moreover, the coefficients d are detail coefficients or alternatively the high-pass output.

Additionally, Mallat (1989) also introduced the reconstruction algorithm, called fast inverse DWT, in which the initial signal $f[n]$ is recovered by up-sampling and filtering. The up-sampled coefficients $\hat{a}$ and $\hat{d}$ are obtained by placing zeros between each pair of samples in the output signals $a[n]$ and $d[n]$. The initial signal is obtained by filtering the zero-padded coefficients by the corresponding inverse filters $\tilde{h}[n]$ and $\tilde{g}[n]$:

$$f[n] = \hat{a} * \tilde{h}[n] + \hat{d} * \tilde{g}[n]. \tag{3.5.11}$$

There exists several families of wavelets which are distinguished by their respective filter coefficients. The Daubechies wavelets, Coiflets, and Symlets are a few examples of wavelet families, proven to be useful for a particular application. The Daubechies wavelets (Daubechies, 1992) are from a family of wavelets which have highly well-located elements, making them suitable tools for signal detection and classification applications. These wavelets are characterized by their vanishing moments, which is their mother wavelet's smoothness property. The mother wavelet with higher vanishing moments is smoother, which leads to error reduction in the decomposition/reconstruction process. Figure 3.12 shows Daubechies-20, i.e. the Daubechies wavelet with 20 vanishing moments, decomposition low-pass and high-pass filters and its corresponding inverse filters.

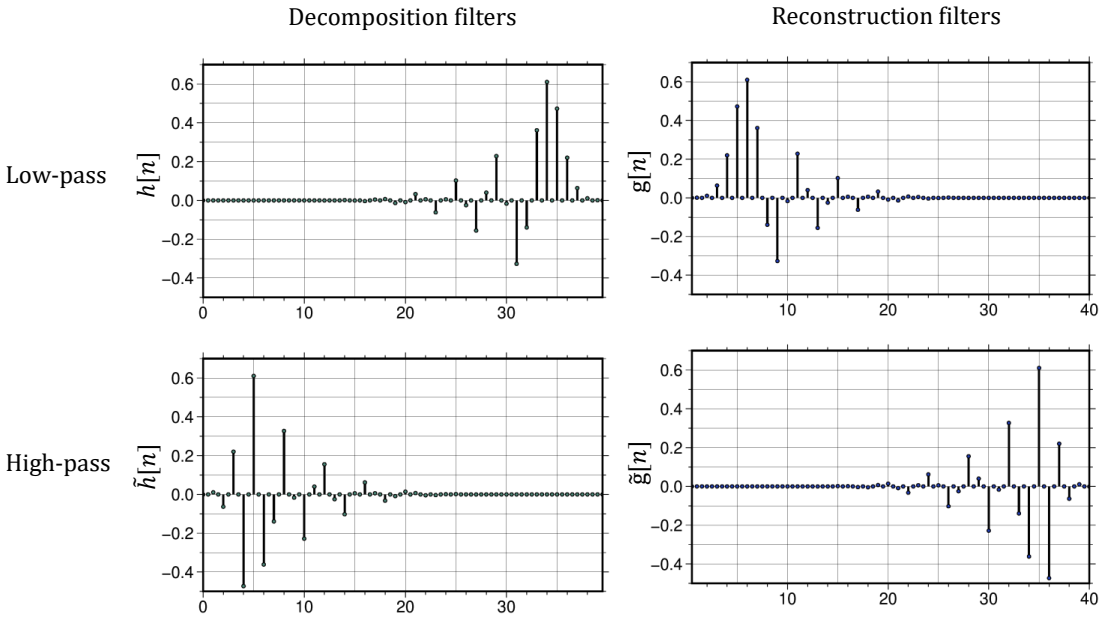

Figure 3.12.: Daubechies-20 decomposition and reconstruction conjugate mirror filters.

3.5.3. Multi-resolution analysis

The Multi-resolution Analysis (MRA) algorithm is an efficient framework to represent a signal at different levels of resolution. As described in section 3.5.2, a single-level DWT decomposes the signal into an approximation subsignal and a detail subsignal. If the decomposition continues successively on the approximation subsignal, as suggested by Mallat (1989) and Y. Meyer (1993), it leads to a sequence of details with desired spectral and temporal resolutions. In other words, the initial signal turns into the approximation coefficients of the last decomposition level and the accumulated detail coefficients of every level. If needed, the original signal can be reconstructed again from the wavelet representation using the inverse DWT. Figure 3.13 shows a schematic MRA decomposition tree.

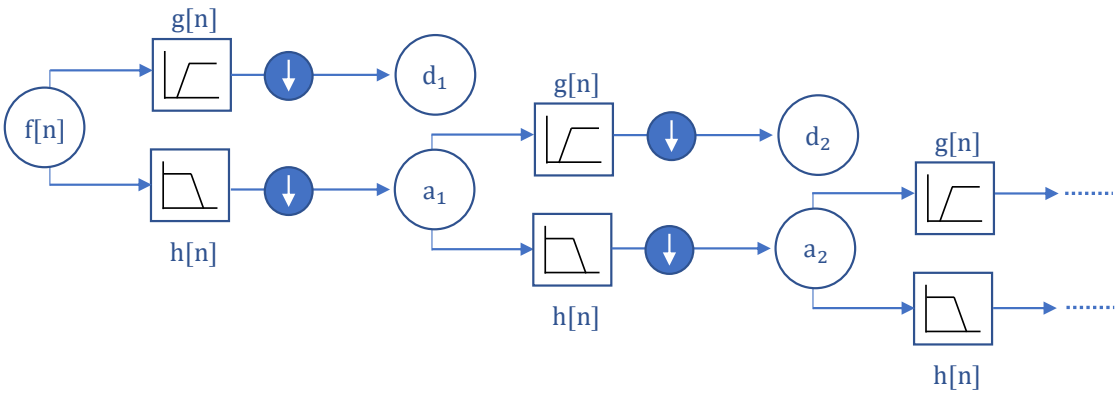

Figure 3.13.: MRA decomposition tree. At each level of decomposition, the signal passes through a high-pass filter $g[n]$ and a low-pass filter $h[n]$. The filtering is then followed by a factor two down-sampling.

Range-rate residual analysis 4

Attribution This chapter of this dissertation which addresses the remaining error contributors in ITSG-Grace2018 preliminary results, is a revised version of the publication Behzadpour et al. (2019) by the author. This chapter adapts the same methodology and focuses on the KBR instrument-related errors, therefore expands on section 4 of Behzadpour et al. (2019). This is a necessary background for Chapter 5 and the final ITSG-Grace2018 model (Kvas et al., 2019), where the introduced systematic errors are being eliminated.

This chapter investigates the ability of wavelets in identifying KBR instrument related error sources in GRACE range rate residuals. The Multi-resolution Analysis (MRA) (cf. Section 3.5.3) is applied to decompose the monthly residual signal into different scales with corresponding frequency bands and explain temporal, spectral, and orbit-related features of each scale.

The advantage of the implemented method is a better separation of superimposed signals in frequencies lower than 10 mHz. This method enabled the identification of (a) systematic errors caused by eclipse crossings of the satellites and (b) systematic errors due to Sun intrusion into star camera, which are respectively explained in Section 4.6 and Section 4.4.

4.1. Introduction

When sets of global gravity field parameters are estimated from data sets of inter-satellite ranging measurements from GRACE, the postfit measurement residuals exceed the expected level considerably. The postfit residuals are particularly large for spectral components in the mHz band where they exceed the expected influence of sensor noise by one order of magnitude. This frequency band is particularly important for the determination of time variable gravity and mass variations. For further improvement of gravity field results, it is needed to disentangle and understand the sources of residuals in this frequency band.

Several effects are known to contribute to the residuals: systematic sensor and system modeling errors, such as uncertainties in star camera and accelerometer data, as well

as geophysical aliasing due to undersampling of rapid mass variations. In recent years, significant research efforts have been made to identify and model the GRACE systematic errors in KBR ranging system (Kim & Tapley, 2002; Ko et al., 2012), star camera data (Bandikova & Flury, 2014; Ellmer, 2018; Goswami et al., 2018; Harvey, 2016; Inácio et al., 2015) accelerometer data (Flury et al., 2008; Klinger & Mayer-Gürr, 2016b; Peterseim et al., 2012), and the effects of geophysical aliasing and uncertainties in background models (Bonin et al., 2012; Kurtenbach et al., 2012; Kvas et al., 2018).

The errors propagate through the complex numerics of estimating a large number of parameters: orbit parameters, spherical harmonic gravity field coefficients, sensor parameters – with the result of complex correlations and leakage of errors that goes on the one hand to the parameters, and on the other hand to the postfit observation residuals. As a result, residual analysis becomes a research topic since it not only leads to detection of measurement and physical modeling errors, but it also aids in the evaluation and improvement of gravity field solutions.

Over the years, there have been several attempts to provide a GRACE error budget based on real GRACE observations as well as simulated data. Ditmar et al. (2012) investigates the theoretical residuals, which are the difference between the observed GRACE ranging data and simulated data based on satellites orbit and force models. Using spectral analysis, they revealed that the noise budget is dominated by KBR system noise and inaccuracies in Earth's static gravity field at higher frequencies. On the other hand, for low-frequency noise, uncertainties in background models and errors in computed dynamic orbits are the major contributors to the noise budget. Flechtner et al. (2015) also confirmed these results by performing a full-scale simulation for GRACE-FO time-span and indicated that accelerometer noise, as well as inaccuracies in ocean tide and non-tidal mass variation model are the main error sources in low-frequency band.

However, using spectral analysis to study the GRACE errors, with main focus on the postfit residuals, has its drawbacks: The residuals are composed of a number of superimposed noisy signals and the spectral analysis performs the best based on the assumption that these signals have stationary behavior. The stationarity means that the mean, variance and autocorrelation function of the signal do not change over time. However, in reality, the features of transition and nonstationarity in residual time-series limit the reliability of the spectral analysis. As shown in Figure 4.1a, the classic Fourier analysis only describes the frequency components of the residuals and is unable to represent the beginning time and duration of each signal component (Keller, 2004).

One simple way to represent time variations of spectral components is to apply short time Fourier transform (STFT) (cf. Section 3.5.1). Figure 4.1b shows the square root of the STFT coefficients of an arbitrary residual time-series, which is called a spectrogram. A spectrogram represents the variation of spectral content over time. However, as

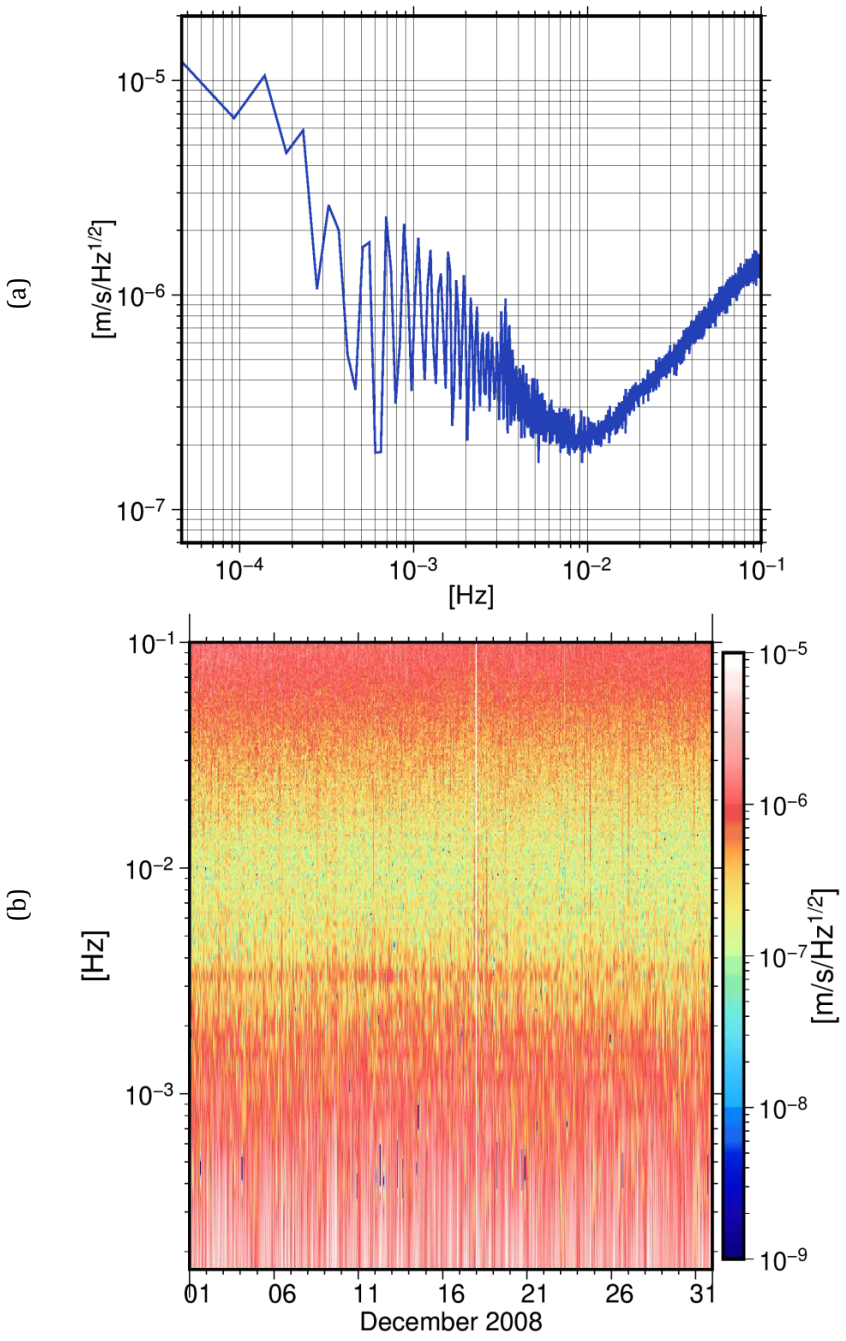

Figure 4.1.: GRACE range rate residuals from December 2008, obtained from preliminary ITSG-Grace2018, with AOC propagated errors (cf. Section 4.5). The residuals are expressed in terms of (a) root power spectral density (PSD) and (b) Spectrogram.

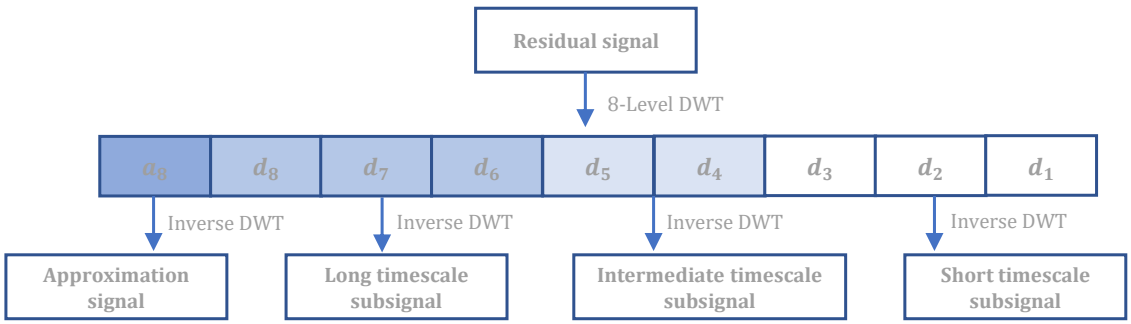

Figure 4.2.: Scheme of the proposed MRA method, which decomposes the residual signal into 4 subsignals.

mentioned in Section 3.5.1, the constant length of the STFT window function leads to the fixed time and frequency resolutions.

Wavelet analysis (cf. Section 3.5.2) is proposed to overcome resolution limitations of STFT in study non-stationary signals (Keller, 2004). In contrast to STFT, the wavelet transform provides a better trade-off between time and frequency resolutions by optimally adapting the window size to fully exploit the signal content.

The goal of this chapter is to use the wavelet transform to study the key contributors to GRACE range-rate residuals and, uncover non-stationary noise sources in KBR instrument that traditional spectral analysis cannot detect.

4.2. Decomposition of GRACE range-rate residuals

This study is conducted on GRACE range-rate residuals obtained in the course of computing the preliminary ITSG-Grace2018 (Kvas et al., 2019) gravity field model up to degree and order 60. The preliminary solutions are based on the state-of-the-art background and stochastic models, with only parameter estimated for KBR measurement being the antenna phase center variations (cf. Section 2.6).

The proposed method applies MRA to monthly time-series of residuals. The mother wavelet is chosen to be a discrete Daubechies wavelet transform with 20 vanishing moments (Daubechies, 1992) and the decomposition continues up to 8 levels (cf. Section 3.5.3). The Daubechies wavelet was chosen because of its common application in digital signal analysis and feature extraction. The choice of a high vanishing moment is due to the corresponding high smoothness feature and consequently more accurate frequency localization.

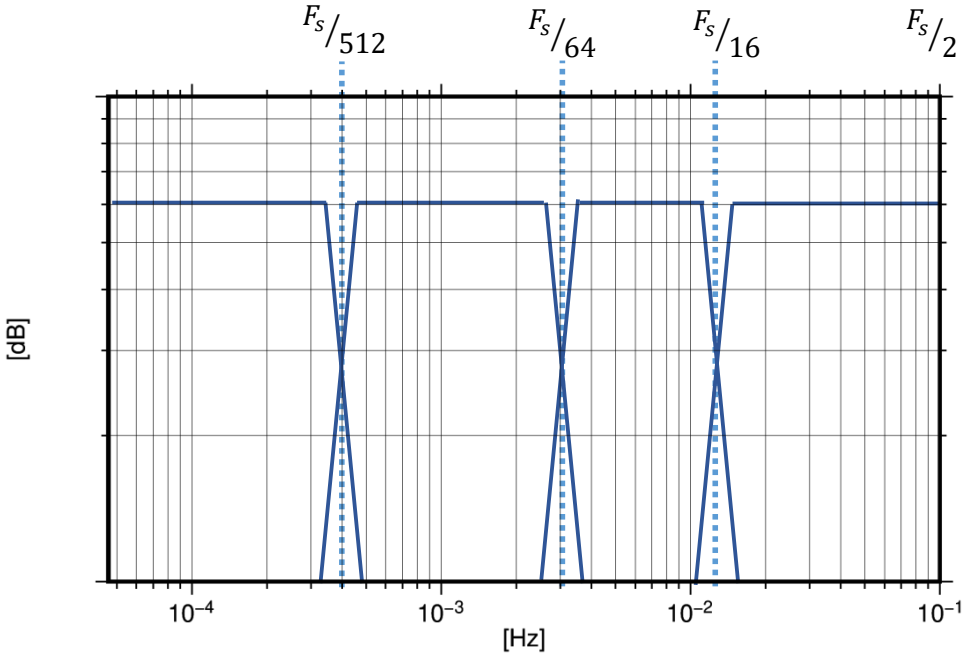

Figure 4.3.: Corresponding frequency bands for the decomposed subsignals based on the sampling of the original signal $F_S = 0.2\,\text{Hz}$.

Figure 4.2 shows the proposed method to decompose the residual signal. Based on the characteristic of the signal, the output is the results of the approximation signal and merged detail coefficients, categorized in three frequency sub-bands:

Short timescale details level 1 to 3 detail coefficients, which correspond to the frequency spectrum above 10 mHz;

Intermediate timescale details level 4 to 5 detail coefficients, which correspond to the approximate frequency spectrum from 3 mHz up to 10 mHz;

Long timescale details level 6 to 8 detail coefficients, which correspond to the approximate frequency spectrum from 0.5 mHz up to 3 mHz;

Figure 4.3 shows the resulting frequency sub-bands. At the final step, each detail group is transferred into time domain by inverse DWT. These time-series are considered as residual subsignals, which can be further analyzed in following domains:

Spectral/temporal domain As mentioned in Section 3.5, time-frequency methods show variations of the signal's frequency components w.r.t time. For nonstationary signals, this yields to the temporal localization of a signal's spectral components. Spectrogram (cf. Section 3.5.1) is an example of these methods, which illustrates changes of a signal's power as a function of time and frequency. The scalogram, which plots the amplitude of the coefficients as a function of the

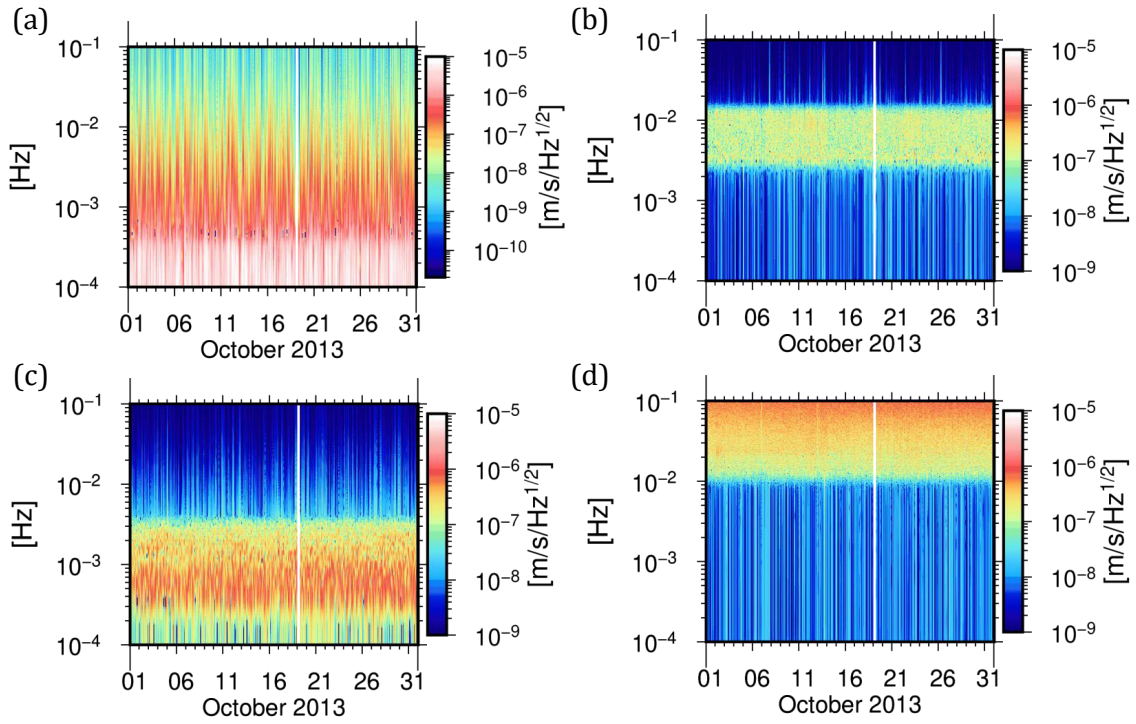

Figure 4.4.: Spectrograms of (a) short timescale, (b) intermediate timescale, (c) long timescale, and (d) approximation subsignals of the residual signal for October 2013. The window length is set to five hours.

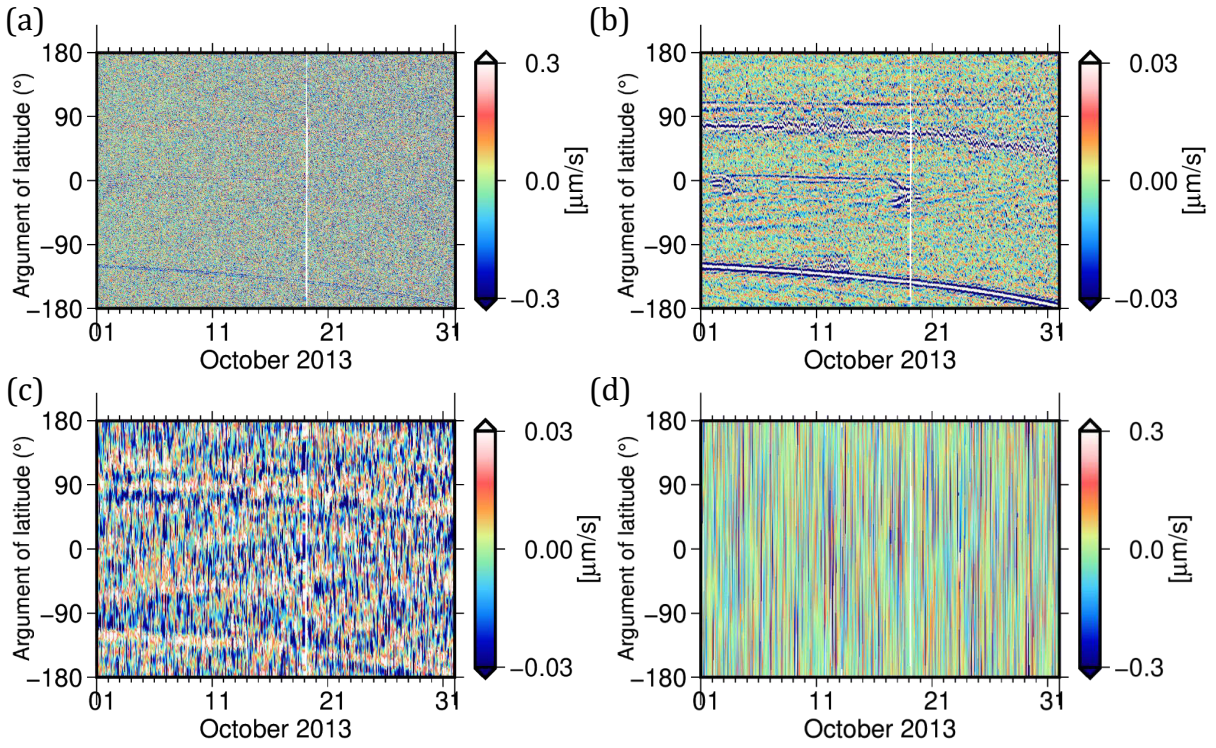

Figure 4.5.: Orbital analysis of (a) short timescale, (b) intermediate timescale, (c) long timescale, and (d) approximation subsignals of the residual signals for October 2013 w.r.t the GRACE-A argument of latitude.

scale and transition parameters, is another method in this category and can be used directly on the wavelet coefficients. For the analysis of residual subsignals, spectrograms are employed because interpreting a signal in terms of frequency is easier than scale. Figure 4.4 shows the spectrograms of the residual subsignals for October 2013.

Orbital domain To detect errors caused by instrument faults under certain orbital conditions, plotting each subsignal as a function of satellite angular position and time is helpful. The angular position is described by argument of latitude ν (cf. Appendix B), which describes the angle between the ascending node and the satellite. For GRACE satellite with a near-circular orbit, $\nu = 0°$ represents the ascending equator pass, $\nu = 90°$ the north pole, $\nu = 180°$ the descending equator pass, and finally $\nu = -90°$ the south pole. Figure 4.5 shows the residual subsignals for October 2013 w.r.t the GRACE-A argement of latitude.

These analysis cover the entire GRACE time span. With the main focus on KBR system errors, the following sections present highlight results from studying short and

intermediate time scales. These scales, which are equivalent to the frequency band above 3 mHz, are mainly dominant by the KBR system errors. For the long scale details, where the background models, in particular ocean tide model, are expected to be the main error contributor, the reader is referred to Behzadpour et al. (2019).

4.3. KBR system noise

To prove whether or not the applied method using the DWT is capable to detect the error sources, the investigation starts with well-known issues of the GRACE instruments. For instance, based on simulation and real data studies, it has been proved that the K-band system noise is dominant in the frequency range above 10 mHz (Ditmar et al., 2012; Kim, 2000). According to Kim (2000) errors of the pure K-band measurement depend on:

- Oscillator noise,
- System noise, including receiver noise and the time-tag error due to the different clock error for the two satellites, and
- Multipath noise, which is due to the reflection of the indirect K-band signals around antenna horn, depending on the satellites' attitude.

Neglecting the time-tag error and multipath noise in this step, the total accuracy of the K-band range measurement $\sigma_{error,r}$ can therefore be determined by the sum of the oscillator noise model σ_{USO} and receiver system noise model σ_{RCV}. According to Frommknecht (2007), the oscillator required noise level can be estimated using the following equation:

$$\sigma_{USO} = \frac{1}{2}(1 - e^{-2\pi\tau f})^2 \left(0.029 + \frac{77}{f^2} + \frac{5.3}{f^3} + \frac{0.0059}{f^4}\right). \tag{4.3.1}$$

Here τ denotes the signal propagation time between the two satellites, which is approximately 0.7 ms and f is the frequency. The receiver system noise is modeled as white noise and can be approximated by the following equation:

$$\sigma_{RCV} = 1 \times 10^{-6} m/\sqrt{Hz}. \tag{4.3.2}$$

The error models for the range rate can be derived from the error models eq. (4.3.1) and eq. (4.3.2), propagated onto range rate by differentiation:

$$\sigma_{KBR,\dot{r}} = \sigma_{KBR,r} \cdot 2\pi f. \tag{4.3.3}$$

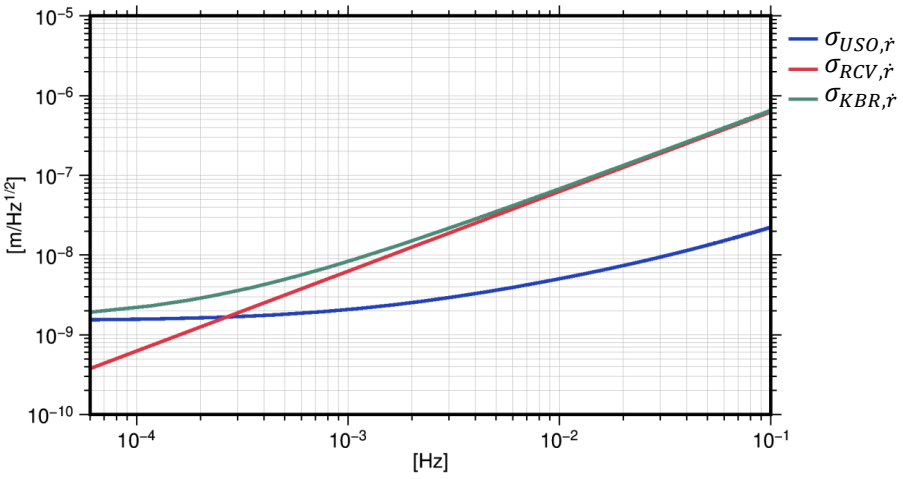

Figure 4.6.: $\sqrt{PSD}$ of the main components of the range-rate noise: USO instability and receiver system noise. The system noise is dominant in the frequency band above 0.3 mHz.

Figure 4.6 shows the root PSD of the range noise due to the USO instability and system noise. It can be concluded that up to a frequency of approximately 0.3 mHz the oscillator noise is dominant and in the frequency band above 0.3 mHz the system noise predominates. This frequency band corresponds to the short timescale details of the residuals.

Figure 4.7 compares these models with the actual range-rate residuals from December 2008. It can be seen that a more realistic $\sigma_{RCV} = 2.5 \times 10^{-6} m/\sqrt{Hz}$ explains the errors in the high-frequency band. In this band, the spectrogram of the short timescale components also shows similar linear relation with the frequency.

Ko et al. (2012) and Harvey et al. (2017b) showed that σ_{KBR} is dependent on the signal-to-noise ratio (SNR) of the K and Ka frequencies of the KBR system, with drops in signal quality, resulting in higher system noise. SNR values lower than minimum mission requirement, which is 630 (0.1)dB-Hz, indicate high phase errors and, therefore, reduced quality of the range observations. Figure 4.8a-d shows SNR values reported for four phase observations of two satellites for the year 2009. GRACE-A Ka SNRs shows the most stable behaviour, whereas for most of the mission period, erroneous low GRACE-B Ka SNR values are observed and therefore are not considered for data flagging. The three valid SNR values occasionally experience drops, mainly for two reasons (Harvey et al., 2017b):

1. Thermal variations in KBR system, affecting mainly GRACE-B K-band SNRs,
2. Sun intrusion into one of the star camera head, affecting mainly GRACE-A K-band SNRs, see Section 4.4.

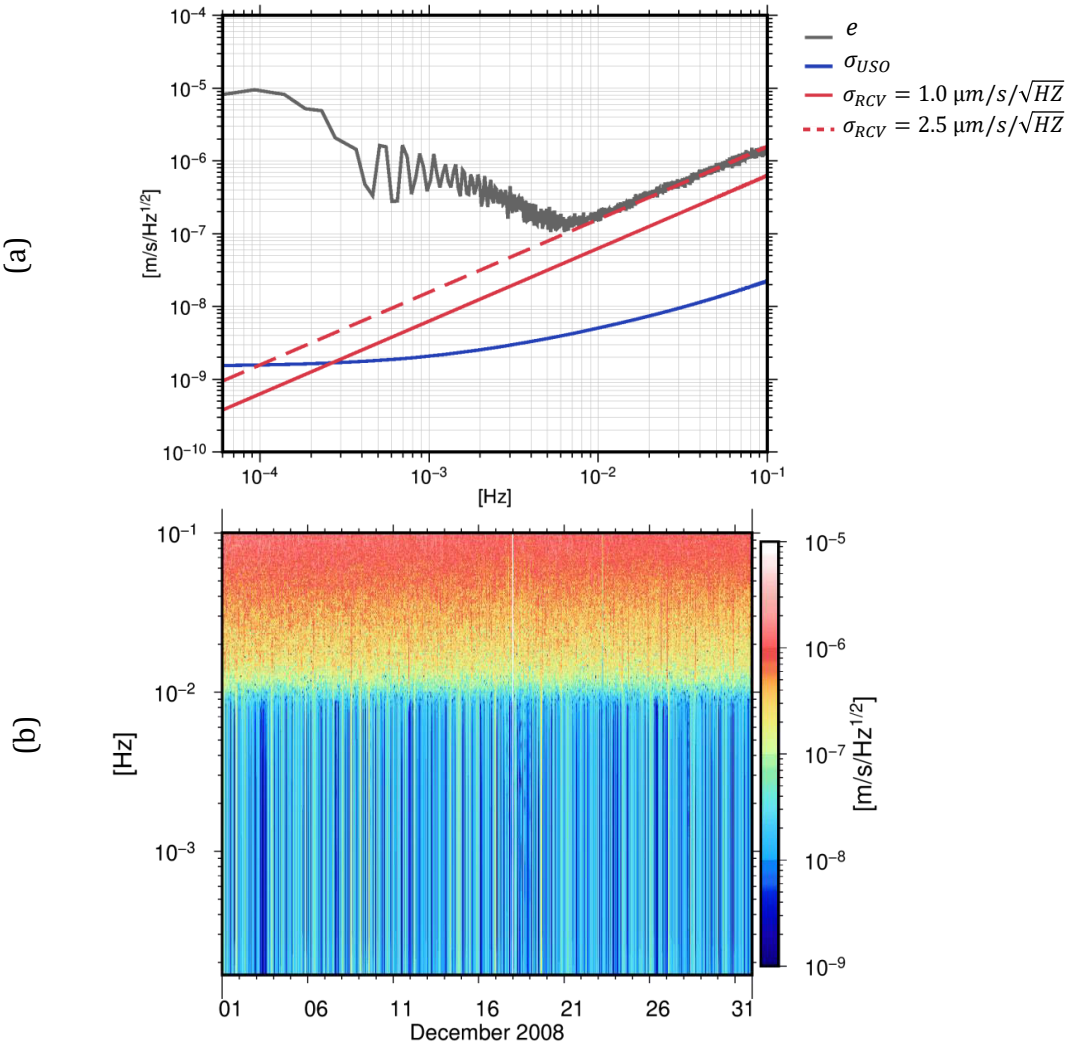

Figure 4.7.: (a) $\sqrt{PSD}$ of the range-rate noise components, compared to range-rate residuals from December 2008.(b) Spectrogram of short timescale components of the same months, showing linearly increased power with frequency.

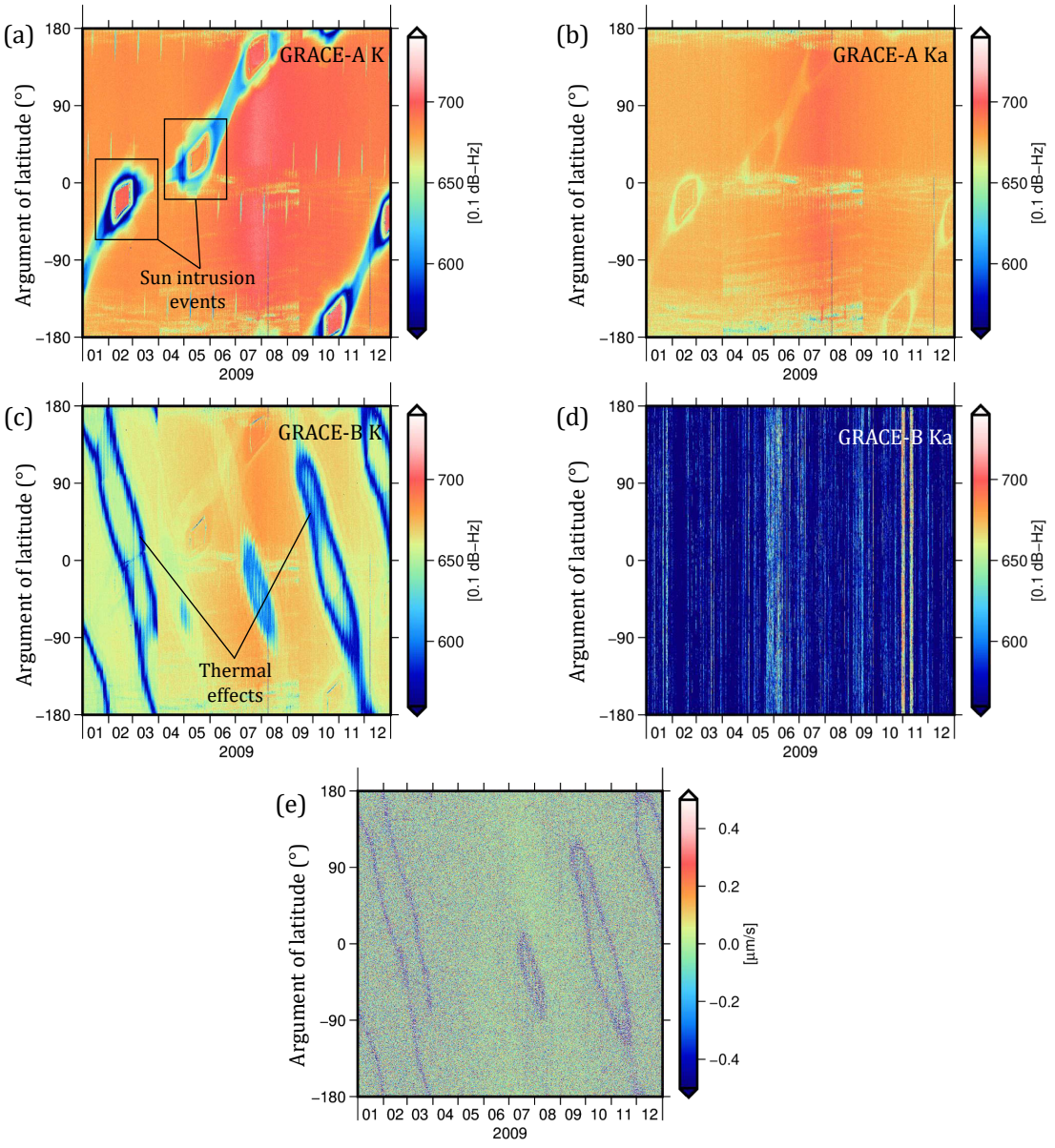

Figure 4.8.: (a) GRACE-A K, (b) GRACE-A Ka, (c) GRACE-B K, (d) GRACE-B Ka SNR values, and (e) short timescale details of the residuals in 2009. Short scale details have strong correlations with GRACE-B K-band SNRs. The values are plotted w.r.t the GRACE-A argument of latitude.

Harvey et al. (2017b) showed that the excessive high frequency noise in KBR observations is highly correlated with low SNR values of the K-band frequency observations by GRACE-B. They claimed that the fluctuations in one of the thermistors located near the KBR assembly are the reason of the drops in the K-band SNRs. Goswami et al. (2018) also demonstrated that these drops are propagated to the range-rate observations and consequently to the postfit residuals. Figure 4.8d confirms that the high frequency features in wavelet short timescale components have a strong correlation with temperature-dependent SNR drops.

4.4. Systematic errors due to Sun intrusion into star camera

GRACE satellite equipped with two star cameras, primary and secondary, providing information about the attitudes of the spacecraft. The redundant SCA head ensures the availability of attitude information, because each of SCA repeatedly is blinded by the Sun and the Moon. These events, in addition to thermal events, cause drops in the SNR values of K- and Ka-band signals on GRACE-A and K-band signal on GRACE-B (Goswami et al., 2018; Harvey et al., 2017b). The reason for these drops might lie in the fact that the KBR assembly is located near the instrument processing unit (IPU). This unit is responsible for SCA data processing onboard. Therefore, when the Sun/Moon enters the field-of-view (FOV) of one head, IPU processing increases, and this cause electromagnetic interference with the KBR system. When the FOV is fully blinded, the attitude is derived from the only available SCA head and IPU processing is reduced.

Figure 4.9 compares the intermediate timescale of the residuals with the GRACE-A K-band SNR values. Note that the drops in these SNRs cause rather deterministic spikes, whereas the thermal drops in GRACE-B SNRs increase the power of the stochastic noise on the KBR observations.

4.5. Antenna offset correction uncertainties

The Antenna Offset Correction (AOC) is one of the corrections applied to the KBR observations. The correction is derived from attitude data and antenna phase center vector specific to each satellite. Therefore, the magnitude of uncertainty of the satellite attitude data directly maps into the AOC and consequently to the KBR observations.

When left unmodeled, the propagated errors from attitude data are expected to be found in intermediate timescale details, according to Inácio et al. (2015) and Bandikova

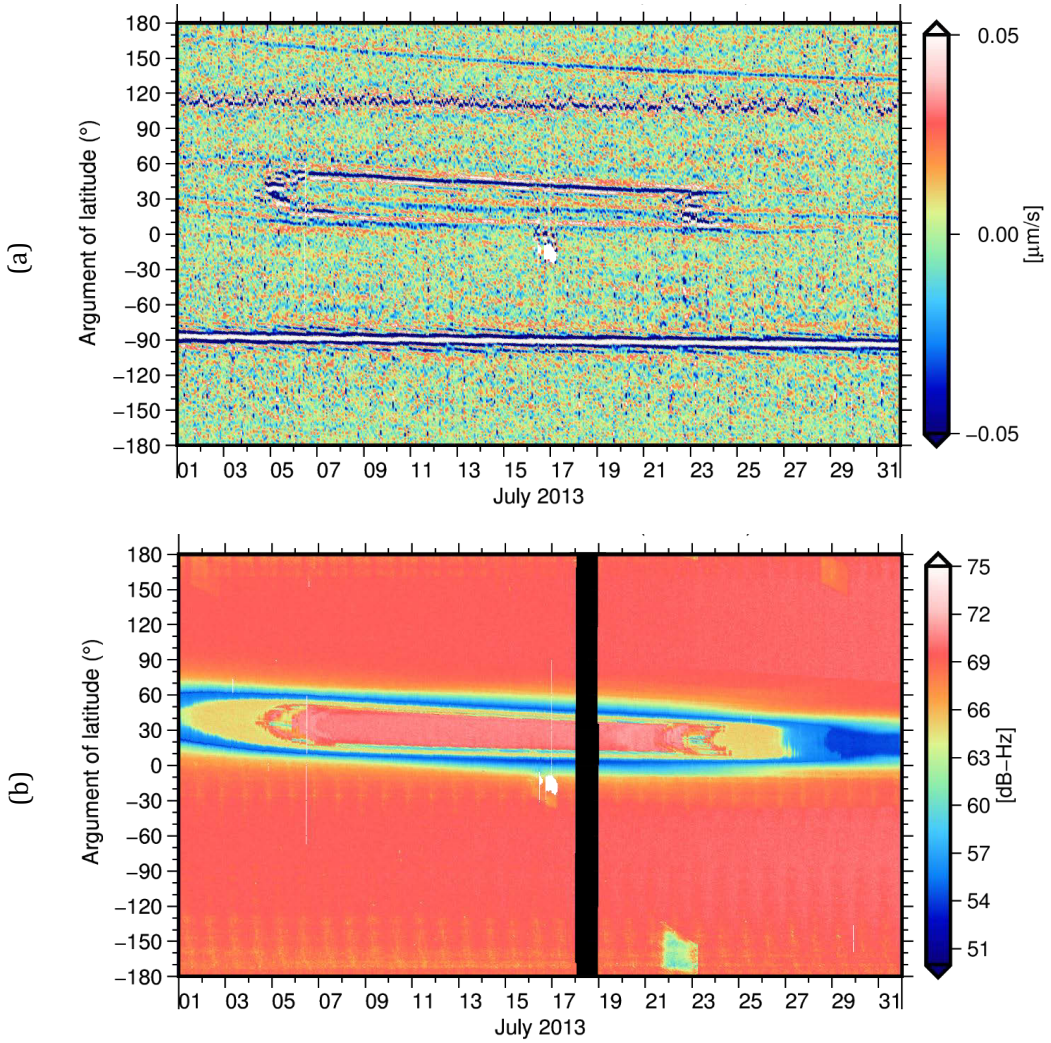

Figure 4.9.: Event associated with Sun intrusion to star camera can be seen in (a) intermediate timescale details of the residuals, and (b) GRACE-A K-band SNR values. The values are plotted w.r.t the GRACE-A argument of latitude in July 2013 and the black areas show data gaps in the SNR data.

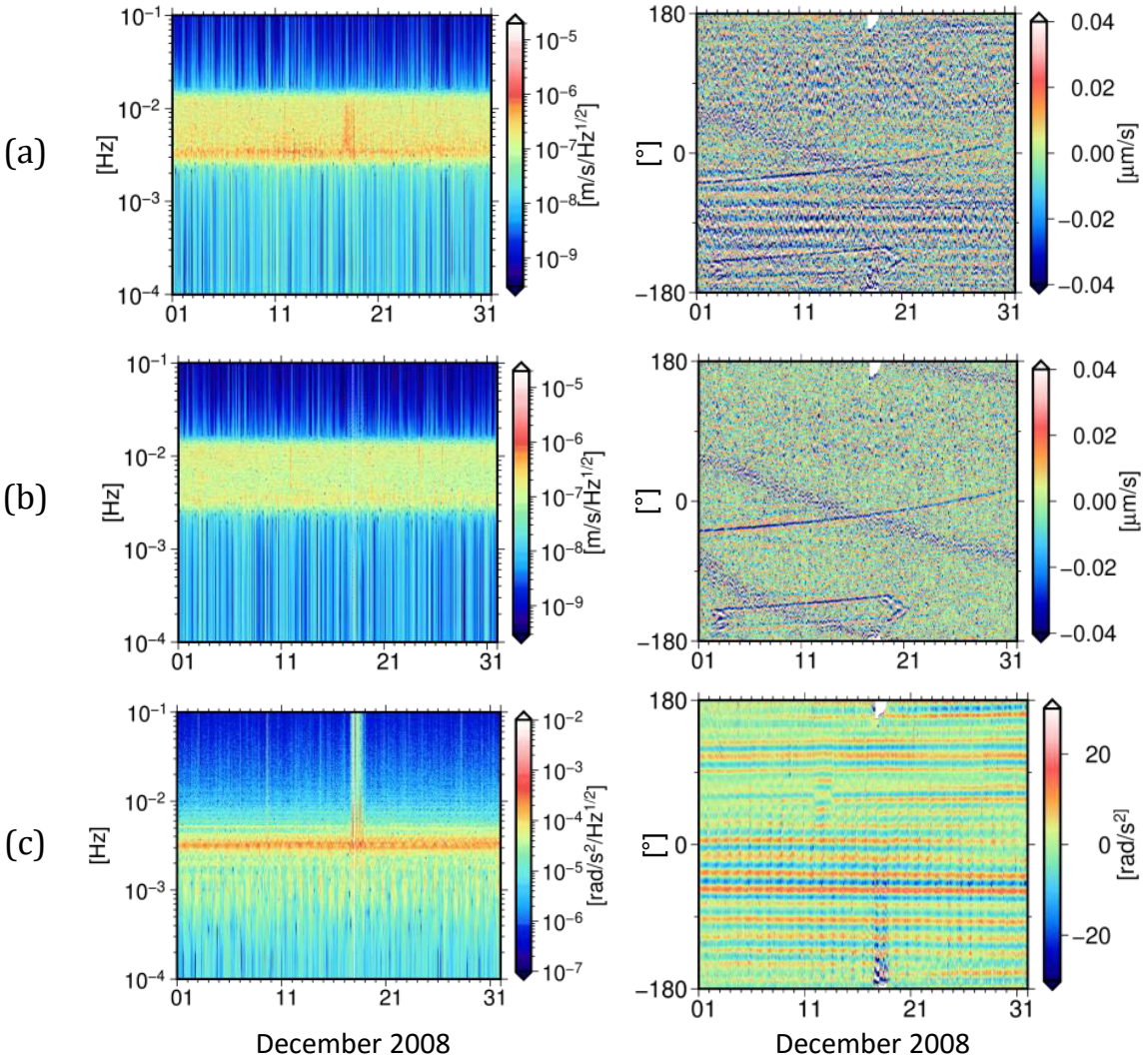

Figure 4.10.: Spectrograms (right panel) and orbital analysis (left panel) of (a) intermediate timescale details with AOC propagated errors, (b) intermediate timescale details after considering AOC stochastic model (Ellmer, 2018), (c) GRACE-A pitch angular acceleration variations for December 2008.

et al. (2012). Time-frequency analysis, shown in Figure 4.10, reveals a similarity between the residuals in intermediate scale and the angular acceleration variations derived from star camera observations.

Ellmer (2018) developed a stochastic model for the AOC through variance propagation based on full variance-covariance information of the satellite attitude data. Using one covariance matrix per 3-hourly arc per satellite, the AOC stochastic model was additionally introduced to the stochastic model for the range rate observations. The improved stochastic model better described the errors in the residuals, as shown in Figure 4.10b, and contributed to the improved gravity field solutions in the ITSG-Grace2018.

4.6. Systematic errors due to eclipse crossings

In addition to AOC propagated errors and Sun intrusion events, analysis of the intermediate timescale details reveals systematic features, which usually have a consistent intensity over a month.

These signatures can be most clearly observed in 2013, possibly in connection to the solar activity maximum in that year. According to Figure 4.11, these features have a high correlation with the eclipse transition phases of GRACE-A and GRACE-B and intensify under low β' condition.

Eclipse transition phases are occurred when a satellite enters or exits Earth's shadow. In each orbit revolution, the twin satellites of GRACE follow each other in two transition phases. The difference between GRACE-A and GRACE-B shadow factors (cf. Section 3.2.2) indicates if one of the satellites is in a transition phase. Therefore, difference values not equal to zero can be used to identify these transition events. Figure 4.12 compares GRACE-A shadow factors and the identified transition events.

Figure 4.13 illustrates that the systematic spikes in the intermediate timescale details appear at transition events during the whole GRACE time span. The sign of their amplitude, however, changes at several time points such as December 2005, June and December 2014. These periods indicate a time when a swap maneuver was carried out.

During the swap maneuvers, GRACE-A and GRACE-B exchanged their position in the formation. The formation initially started with GRACE-A as leading and GRACE-B as trailing satellite. The first swap maneuver was carried out in December 2005. At this time, it was necessary for the satellites to exchange their positions to limit the surface erosion of the K-band horn caused by atomic oxygen. Before this maneuver, eclipse transition spikes have a positive amplitude and are visible when the pair enters

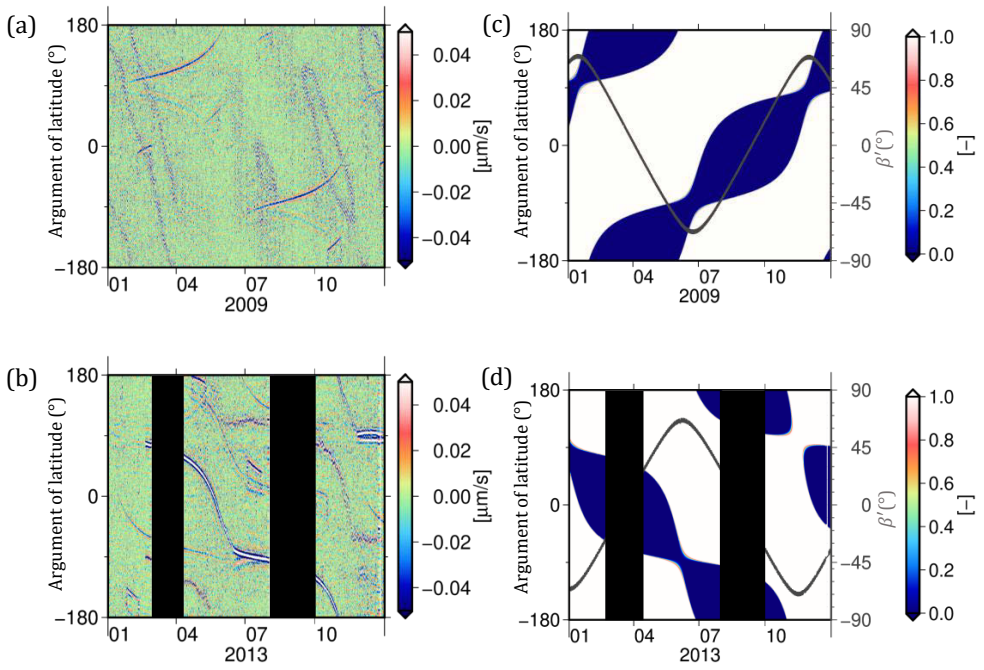

Figure 4.11.: Intermediate timescale details of the residuals in (a) 2009 and (b) 2013. The systematic features are correlated with changes in corresponding shadow factors, (c) and (d). The values are plotted w.r.t the GRACE-A argument of latitude and the black areas show data gaps in the observations.

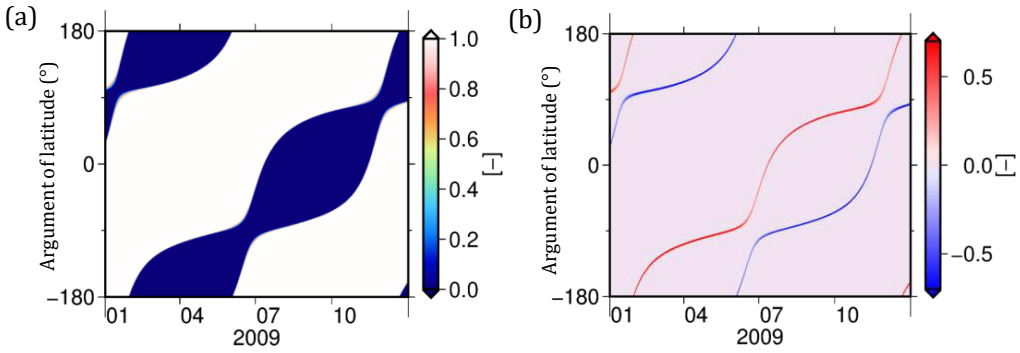

Figure 4.12.: (a) GRACE-A shadow factors derived from SOLAARS-CF model and (b) difference between GRACE-A and GRACE-B shadow factors, indicating transition periods. The values are plotted w.r.t the GRACE-A argument of latitude in 2009.

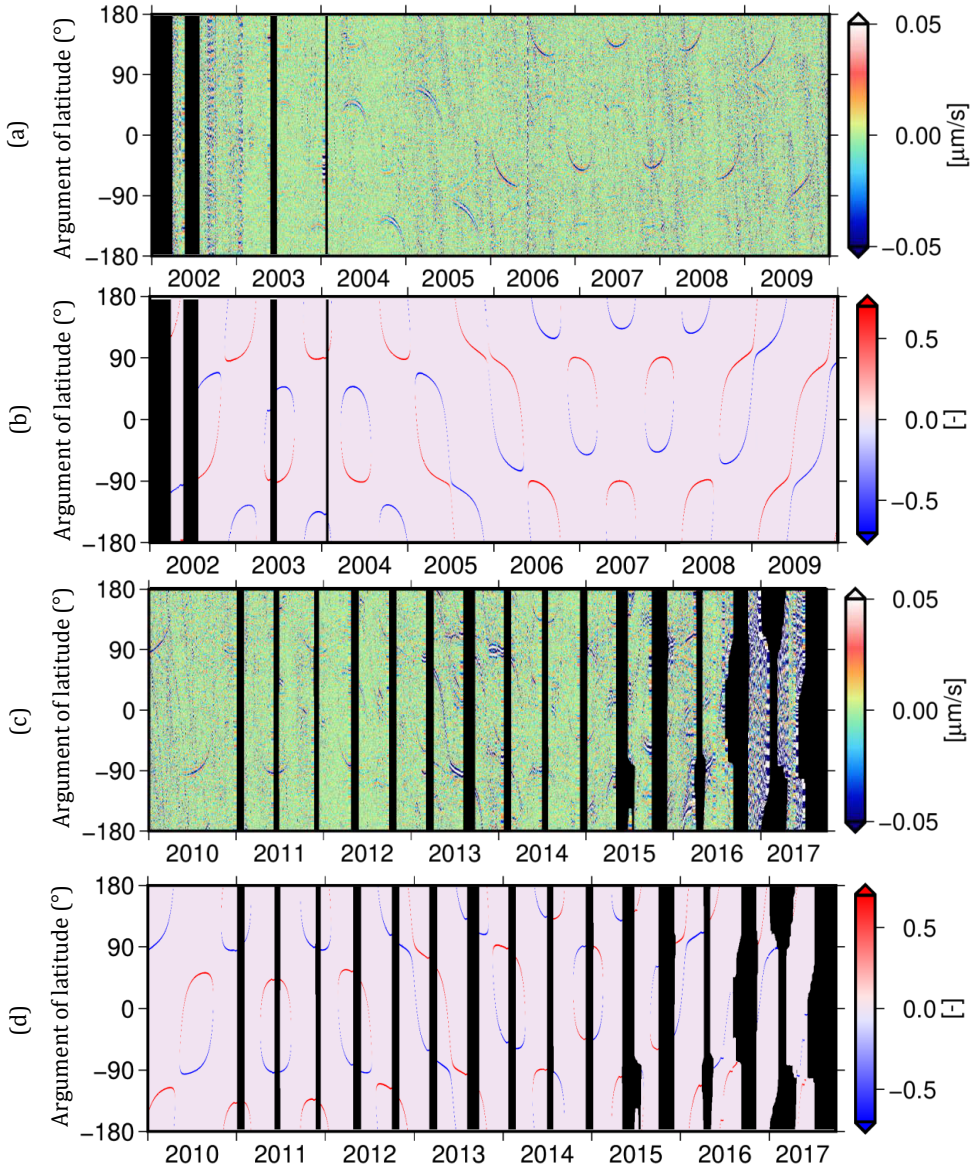

Figure 4.13.: Intermediate timescale details and the difference between GRACE-A and GRACE-B shadow factors from 2002 to 2009, (a) and (b), also from 2010 to 2017, (c) and (d). The values are plotted w.r.t the GRACE-A argument of latitude. The black areas show data gaps in the observations.

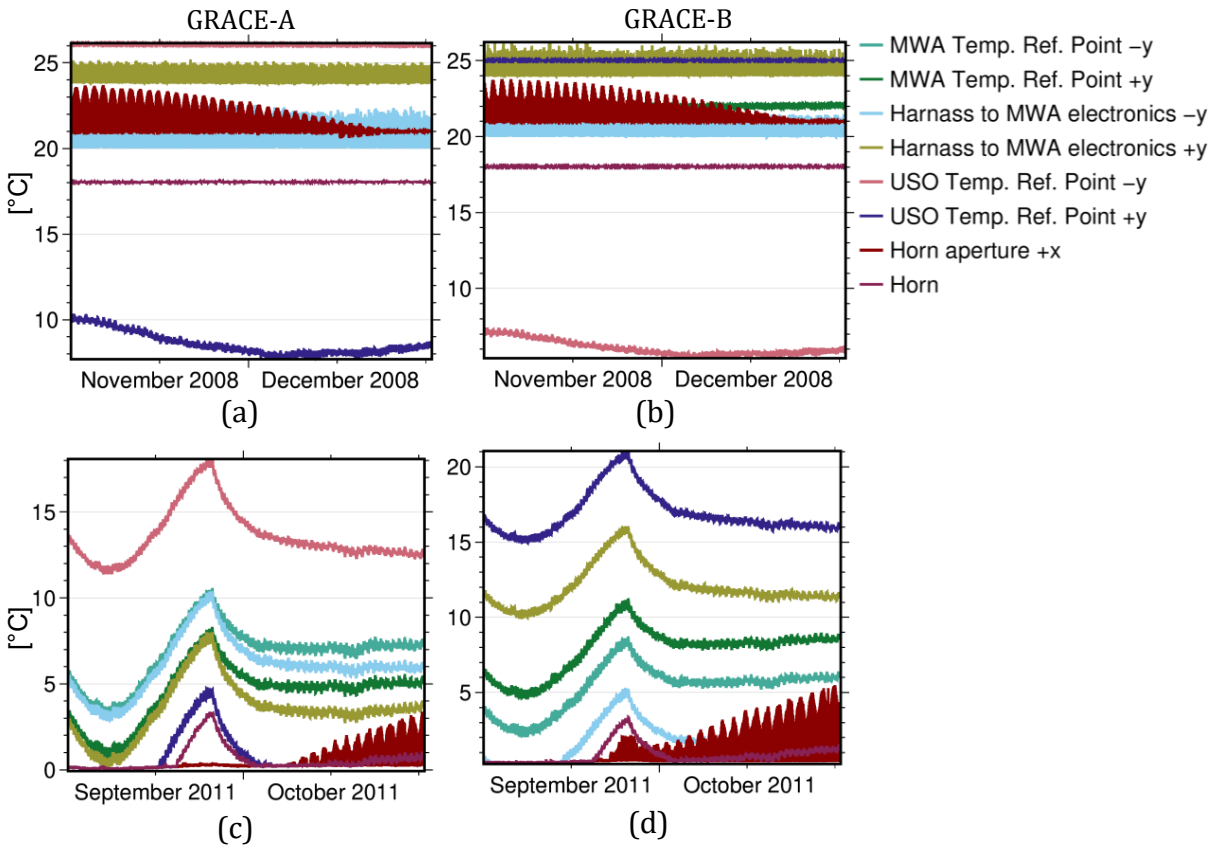

Figure 4.14.: High-resolution temperature measurements from the sensors close to KBR system during November-December 2008 (a: GRACE-A and b: GRACE-B) and September-October 2011 (c: GRACE-A and d: GRACE-B). During the first period, thermal control of the satellites was active and during the second period, it was switched off. Among the selected sensors, KBR antenna horn aperture sensor shows the most variation.

sunlight. Afterwards, with GRACE-B being the leading satellite, the signatures have a negative amplitude and are more visible when the pair enters the Earth's shadow.

After 2011, possibly as a result of disabled thermal control, the signatures appear in both transition events of an orbit revolution. This behaviour remains stable until the second swap maneuver in June 2014, when the sign of the spikes are changed once again. Similar behaviour can be observed during the following swap maneuvers, which happened more often towards the end of the mission.

The appearance and temporal behavior of the eclipse transition spikes in the residuals have been proven initially in Behzadpour et al. (2019) and this dissertation. Before this study, these spikes have been in fact unknown and no other studies address this problem in KBR observations. In the following, the origin of these errors and the

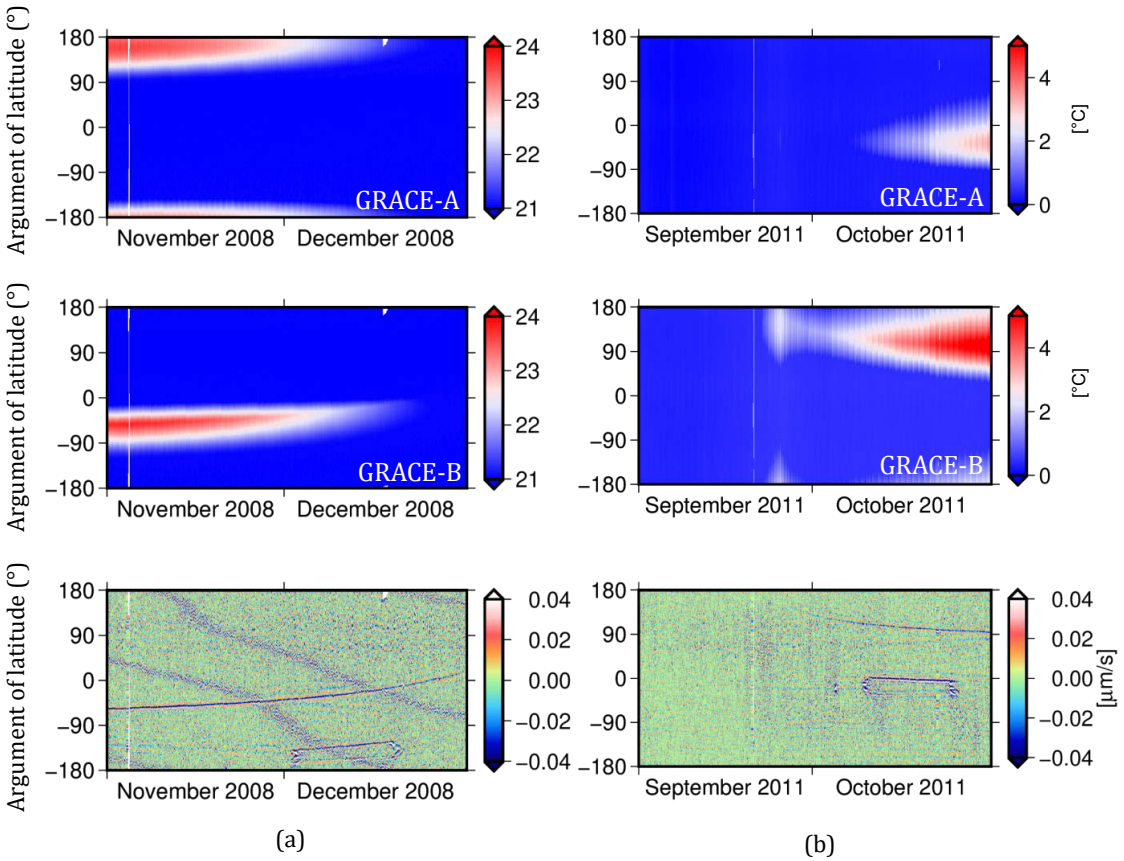

Figure 4.15.: KBR antenna horn temperature data, compared with intermediate timescale details for (a) November-December 2008 and (b) September-October 2011. The values are plotted w.r.t the GRACE-A argument of latitude.

possible source that causes them will be discussed.

Since the eclipse crossing errors are observed in the postfit residuals, there might be several origins that need to be considered such as accelerometer data, original KBR measurements and their corrections. Due to the impacted frequency band, it is unlikely that these errors are originated from accelerometer data. On the other hand, with their absolute mean value of about 0.04 µm/s, it is not possible to detect them directly in the ranging measurements and not even prefit range rate residuals.

Due to the dependency of the errors to the temperature condition of the satellite, the origins of the errors could be linked to the stability of internal temperature. This information can be obtained from GRACE thermal control data. The thermal control system, which includes a set of heaters and thermal sensors, is responsible for maintaining the operational temperature the on-board instruments throughout the mission. A part of thermal sensor measurements are reported in High-Resolution

Temperature data (HRT1A) with 60 s sampling. In the course of this study, a test dataset of GRACE Level-1A data, including HRT1A, became available to ITSG working group by GRACE SDS for further investigation.

Figure 4.14 shows the available data obtained from the thermal sensors, located near KBR system, for November 2008 and October 2011. Due to the active thermal control, temperature measurements are stable in November 2008, whereas in October 2011 with deactivated thermal control, there exists significant temperature variations, correlated with the β angle variations (Klinger & Mayer-Gürr, 2016b). For both periods, however, horn aperture sensor shows the most thermal variations.

Figure 4.15 confirms the connection between the GRACE-B K-band antenna horn temperature variation and the eclipse transition spikes. It can be assume that the rising temperature on the antenna horn could cause disturbances in the KBR measurements. This connection cannot be observed for GRACE-A temperature measurements, and it is not clear whether they also, to some extend, affect the observations. This hypothesis can be further examined for the complete GRACE time-span, once the Level-1A data are publicly available.

4.7. Summary

This chapter discussed the advantage of applying a wavelet analysis to the range-rate residuals, obtained from the preliminary ITSG-Grace2018 gravity field model.

First and foremost, this analysis demonstrates consistent results with the classical Fourier transform in analyzing stationary errors in the residuals: Section 4.3 confirmed that the main contributor to the short timescale details of the residuals, equivalent to the frequency above 10 mHz, is KBR system noise. This is aligned with the previous studies on this subject, e.g. Ko et al. (2012) and Ditmar et al. (2012).

Additionally, Section 4.4 showed that the systematic errors due to Sun intrusion into star camera can be found in intermediate timescale details, equivalent to the frequency range from 3 mHz to 10 mHz. This subject has also been studied in details by Harvey et al. (2017b) and Goswami et al. (2018).

The proposed method leads to a better separation of signals in mHz frequency range. One major result was to identify consistent signatures due to eclipse transition periods of the mission. Section 4.6 discusses these signatures and their possible link to temperature variations in GRACE-B KBR antenna aperture.

Parametric models for KBR systematic errors

5

This chapter describes how a parametric model for KBR systematic errors can be built and how these parameters can be adjusted. For the systematic errors detected in Section 4.4 and 4.6, a model is built that can match the errors by a set of parameters. These parameters need to be adjusted together with gravity field parameters by means of least square adjustment. Further, the impact of these parametric models on gravity field solutions will be discussed.

5.1. Introduction

When sets of global gravity field parameters are estimated from GRACE data, the post-fit residuals are valuable clues, indicating remaining errors in the observations and the estimation process. The postfit residuals are particularly of interest for spectral components in the mHz band. The mHz frequency range contains many valuable gravity field signal contributors, therefore, lowering the residuals in this range is critical for further improving gravity field results.

Prior to the release of ITSG-Grace2018, a careful inspection of the range-rate residuals has been performed in order to identify the un-modelled errors (cf. Chapter 4). This investigation revealed artifacts due to eclipse transition and Sun intrusion events in frequency range of 3 to 10 mHz, propagating into gravity parameters as well in the post-fit residuals, as shown in Figure 5.1.

Aiming at lowering the residuals in mHz frequency band and improving gravity field models, the un-modelled signals and systematic errors need to be taken into account. These errors cannot be described stochastically nor can be reduced beforehand as they cannot be separated from that the actual gravitational signal at the observation level. Therefore, the complex superposition of these signal can be solved during the gravity field estimation process with a proper parametric modeling.

This chapter proposes a novel approach to setup parametric modeling of the systematic errors due to (a) eclipse transition events, and (b) Sun intrusion to star camera field of view. The goal is to improve the gravity field solutions by co-estimating the model

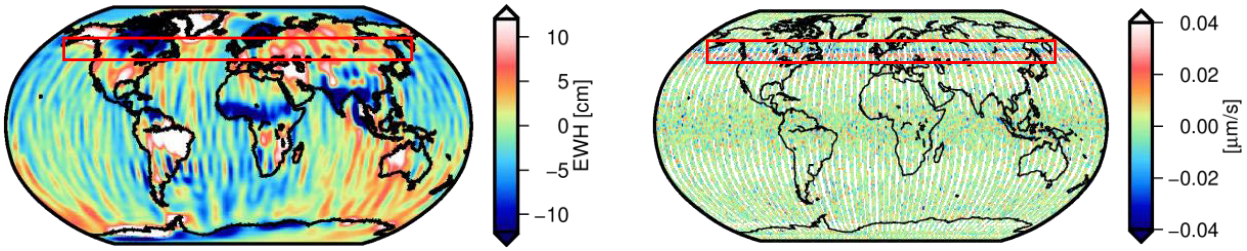

(a) (b)

Figure 5.1.: (a) Monthly gravity field in terms of EWH and (b) intermediate timescale details of the range rate residuals in May 2004. Note that the eclipse transition line, clearly visible in the residuals, also affect the gravity field in the same spatial region.

parameters for these events in the ITSG-Grace2018 scheme. The proposed modeling is validated with the resulting gravity field solutions and the obtained postfit residuals. Due to the improvement resulted from the proposed parametrization, this approach became a part of the processing standards for the ITSG-Grace2018 scheme.

5.2. Modeling systematic errors: Eclipse transition events

As described in Section 4.6, eclipse transition signatures are one of the main component of post-fit residuals in mHz frequency band. These artifacts occur for a short period of time when the pair satellites are in transient condition between sunlight and shadow.

For computing a parametric model for these artifacts, a sufficient number of representative waveforms is needed to obtain a mean model. The amplitude of the waveforms resulted from these events depends on which satellite is the leading satellite. For most of the mission period, when GRACE-B is the leading satellite, the artifacts have positive spike when the pair are entering the shadow area and have a negative spike while they are leaving towards the sunlight.

Figure 5.2 shows two types of the superimposed artifacts corresponding to eclipse crossing periods for an arbitrary month. In this figure, the waveforms are superimposed at the mid time epoch of the transition period, i.e. the time that at least one of the satellites is in penumbra. It is convenient to categorized these errors into positive and negative waveforms. The positive waveform describes a waveform with a large positive peak and the negative waveform is a waveform with a large negative peak. Both types of waveforms are characterized by three major peaks. The positive waveform starts with the first negative peak ranging from 60 to 50 seconds before the reference time,

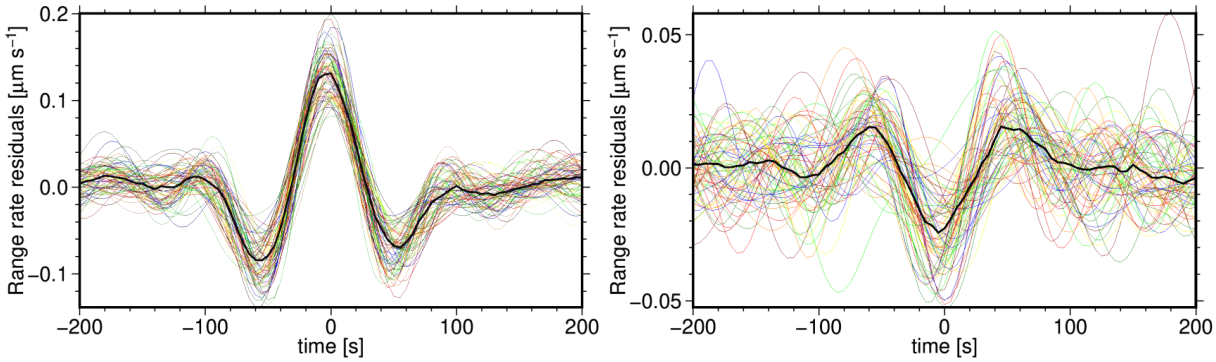

Figure 5.2.: The two types of waveforms occurring in the range-rate residuals from May 2013 in frequency range of 3 to 10mHz during eclipse transition events: (a) positive and (b) negative waveforms. The black line shows the mean model of the superimposed waveforms.

followed by a major positive peak approximately at the reference time, and ends with the second negative peak from 50 to 60 seconds. Similarly, the negative waveform has two minor positive peaks ranging from 60 to 40 seconds before and after the reference time, and one major negative peak around the reference time. The both waveform types last 200 seconds in average. This study finds that during one month, the duration of the waveforms is constant, but the amplitude of the peaks are varying. This applies for both positive and negative waveforms.

From the obtained residuals with a sufficient number of eclipse transition events, one can resolve a mean model for both waveform types and reduce the models from the observations. However, the mean models only describe the mean of a part of these artifacts that would end up in the residuals, and not the part affecting the gravity field parameters. In order to characterize the complete artifact with a set of parameters, the modeling needs to be set-up in the gravity field estimation scheme.

5.2.1. Eclipse transition event detection

To avoid including gravitational signals as well as other unknown effects into the models, eclipse transition events need to be identified beforehand in the monthly time-series. As mentioned before, the parametric model can be set at mid time epoch of the transition period with a margin of 100 seconds, as shown in Figure 5.3. The transition period is determined based on the physical shadow factor of each satellite (cf. Section 3.2.2). As entering or leaving the shadow area results in either positive

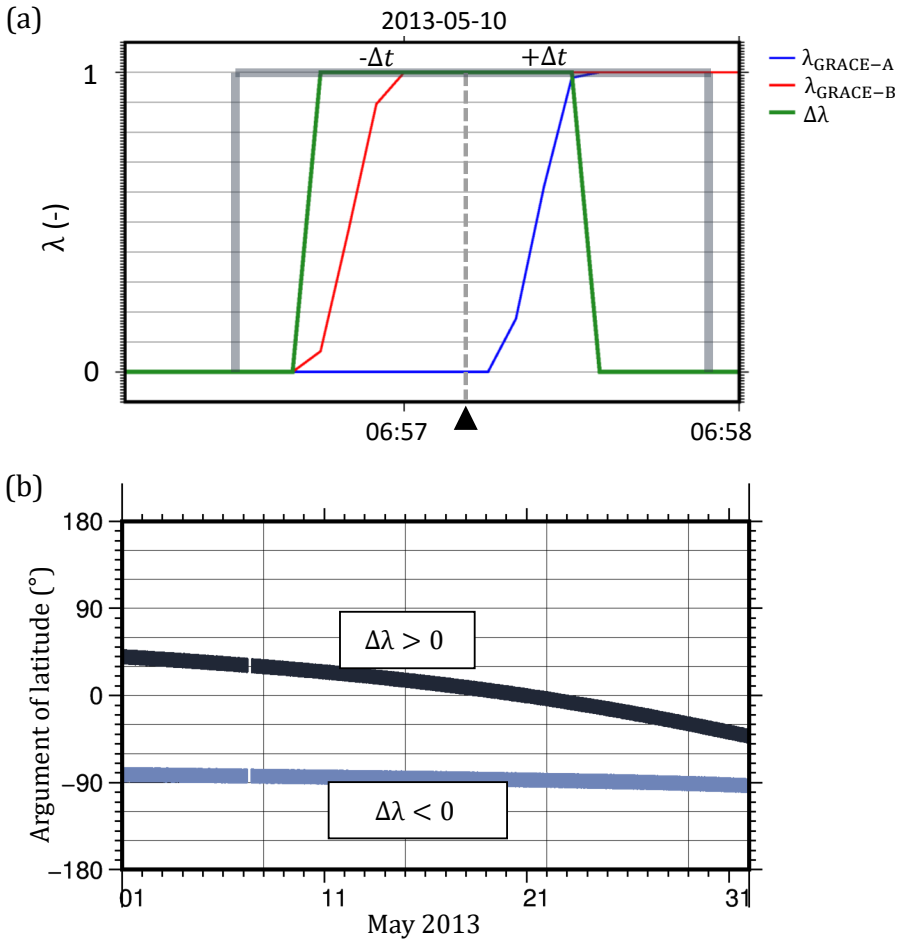

Figure 5.3.: (a) Mission transition period, defined as the time period, when at least one satellite is in penumbra. (b) Two categories of transition period: the periods when the satellites are entering the shadow or entering the sunlight. For each of these types, one parametric model is considered.

or negative waveforms, two different parametric models are considered, as shown in Figure 5.3.

5.2.2. Parametric model and characterization

As displayed in Figure 5.2, the shape of the waveforms can be partially determined from a sufficient number of their representatives in the postfit residuals. To characterize and mitigate these disturbances, they can be best modeled by a parametric model consisting of two parts, schematically described in Figure 5.4. First, the waveform $f(t)$ can be represented by a polynomial of degree n (cf. Section3.4.2), including at least three extreme points (thus $n > 4$), namely the two minor peaks and one major peaks

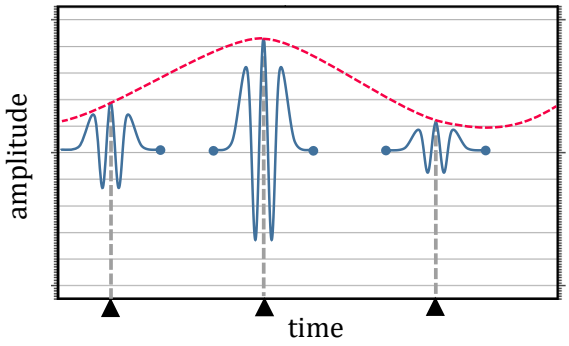

Figure 5.4.: The proposed parametric model, consisting of two parts: The changes of the waveform during each eclipse event is represented by a polynomial (Blue curve) and the magnitude of this waveform through a month is modeled by a uniform B-spline (red curve).

that can be seen in each mean model. Furthermore, the amplitude of the waveforms $B(t)$ which is varying throughout the month can be modeled with a uniform B-spline (cf. Section 3.4.1), to guarantee that the model is continuously differentiable within the month. For a B-spline of degree d with 2 knots at the beginning and at the end of the month, i.e. $d+2$ parameters, the complete model is described as follows:

$$f(t) = \sum_{i=0}^{d+1} b_i B_i(t) \cdot \sum_{j=0}^{n} p_j P_j(t), \tag{5.2.1}$$

which can be rewritten as

$$f(t) = \sum_{j=0}^{n} B_0(t) P_j(t)(b_0 p_k) + \ldots + \sum_{j=0}^{n} B_{d+1}(t) P_j(t)(b_{d+1} p_k). \tag{5.2.2}$$

Therefore, the combined parameters can be estimated from the observations $\boldsymbol{l}$ in the main LSA from

$$\begin{bmatrix} l(t_0) \\ \vdots \\ l(t_m) \end{bmatrix} = \begin{bmatrix} B_0(\tau_0)\boldsymbol{P}(\hat{\tau}_0) & \cdots & B_{d+1}(\tau_0)\boldsymbol{P}(\hat{\tau}_0) \\ \vdots & \ddots & \vdots \\ B_0(\tau_0)\boldsymbol{P}(\hat{\tau}_m) & \cdots & B_{d+1}(\tau_0)\boldsymbol{P}(\hat{\tau}_m) \end{bmatrix} \begin{bmatrix} b_0\boldsymbol{p} \\ \vdots \\ b_{d+1}\boldsymbol{p} \end{bmatrix}, \tag{5.2.3}$$

where $\boldsymbol{P}(\hat{\tau}) = \begin{bmatrix} P_0(\hat{\tau}), \cdots, P_n(\hat{\tau}) \end{bmatrix}$ and $\boldsymbol{p} = \begin{bmatrix} p_0, \cdots, p_n \end{bmatrix}^{\mathsf{T}}$.

5.2.3. Parameter adjustment

To mitigate the systematic errors due to eclipse transition, one needs to find the best fit for the parameters. The optimal choice of parameters would reduce the range-rate residuals in frequency range of 3 to 10 mHz, as well as improve the gravity field in the affected months. Therefore, in addition to comparing the range-rate residuals, it is important to define a criteria that determines whether a specific parametrization improves gravity field, and if so, how the specific scheme performs comparing to other choices.

One established practice to quantify the quality of gravity field solutions derived from GRACE is the temporal error root-mean-square (RMS) over the oceans (Bonin et al., 2012). This criteria is defined based on the fact that the observations only contain ocean signal related to the ocean tide and non-tidal atmosphere and ocean mass variations. As these two sources are modeled and reduced from the observations, it is expected that the gravity variations in most of the ocean area to be negligible. Therefore, the temporal RMS over the oceans mainly describes the errors in the observations and the estimation process and thus can be chosen as a convenient criteria. In this study, a 200-km Gaussian filter is applied to the solutions and trend and annual signals were reduced before computing the RMS values.

The choice of parameters is limited to two months, consisting of November 2008, when the satellites had an active thermal control, and May 2013, when the thermal control was switched off. In the first step, the B-spline degree is set to 3 and it remains constant, while the effect of increasing the polynomial degree is being studied.

Figure 5.5 displays reduction of ocean RMS from the solutions computed with a particular parametrization, w.r.t the ocean RMS of the preliminary solution, i.e. without any parametrization. For both months, positive percentages indicate overall improvement in the quality of solutions. However for November 2008, the improvements are very small, i.e. up to 0.5 percent. Nevertheless, the maximum improvement is achieved with degree 11, whereas for May 2013, degree 10 reaches the maximum improvement of 17.6 percent.

Figure 5.6 and 5.7 show the amplitude of the corresponding range-rate residuals in spectral domain. For November 2008, the lowest amplitude in the frequency range between 3 to 10 mHz is already achieved with degree 5, whereas for May 2013 the minimum range of amplitudes in this band is first achieved by degree 11 and then remains stable for degree 12. Therefore, to have a consistent parametrization throughout the mission, the polynomial degree needs to be set to 11.

In the second step, the polynomial degree is set to 11 and the effect of increasing the B-spline degree is studied. As this effect is small and not clearly visible in spatial

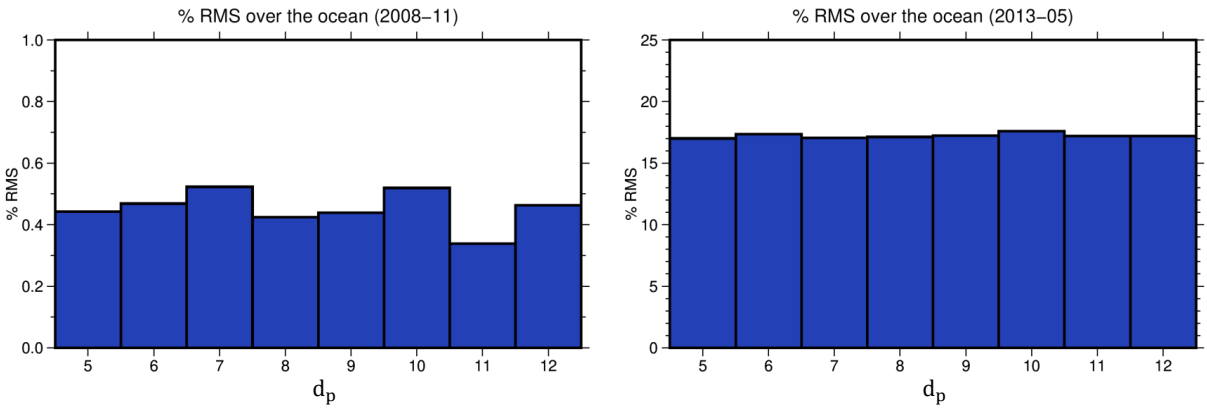

Figure 5.5.: Percentage of reduced ocean RMS in equivalent water height of ITSG-Grace2018 solutions with different polynomial degrees for eclipse transition waveforms. The results are shown for two representative months November 2008 (left) and May 2013 (right). Before computation of the RMS, the annual cycle and trend of GOCO06s were reduced and a 200 km Gaussian filter was applied to each solution. Furthermore, the C_{20} coefficient is excluded from all solutions.

and spectral domains, the results can be better presented in the orbital domain using argument of latitude plots. Figure 5.8 concludes that for November 2008, choosing a 1-degree B-spline, i.e. a linear function, is sufficient to model the artifacts. On the other hand, for May 2013, degree 5 can better model the variation of the signatures during the month. Therefore, for a consistent parametrization, a B-spline of degree 5 is chosen for the final model. With the final parametrization, the range rate residuals in frequency range of 3 to 10 mHz for November 2008 and May 2013 are reduced by 1.7 percent and 19.5 percent, respectively.

5.3. Modeling systematic errors: Sun intrusion to star camera

A similar approach can be taken for modeling the artifacts due to the Sun intrusion events (cf. Section 4.4). For these waveforms, the same parameters as the eclipse transition model can be selected, because both type of errors have the same behaviour in the same frequency range. However, to identify the time interval of these events, a closer look into the condition that triggers these artifacts is required.

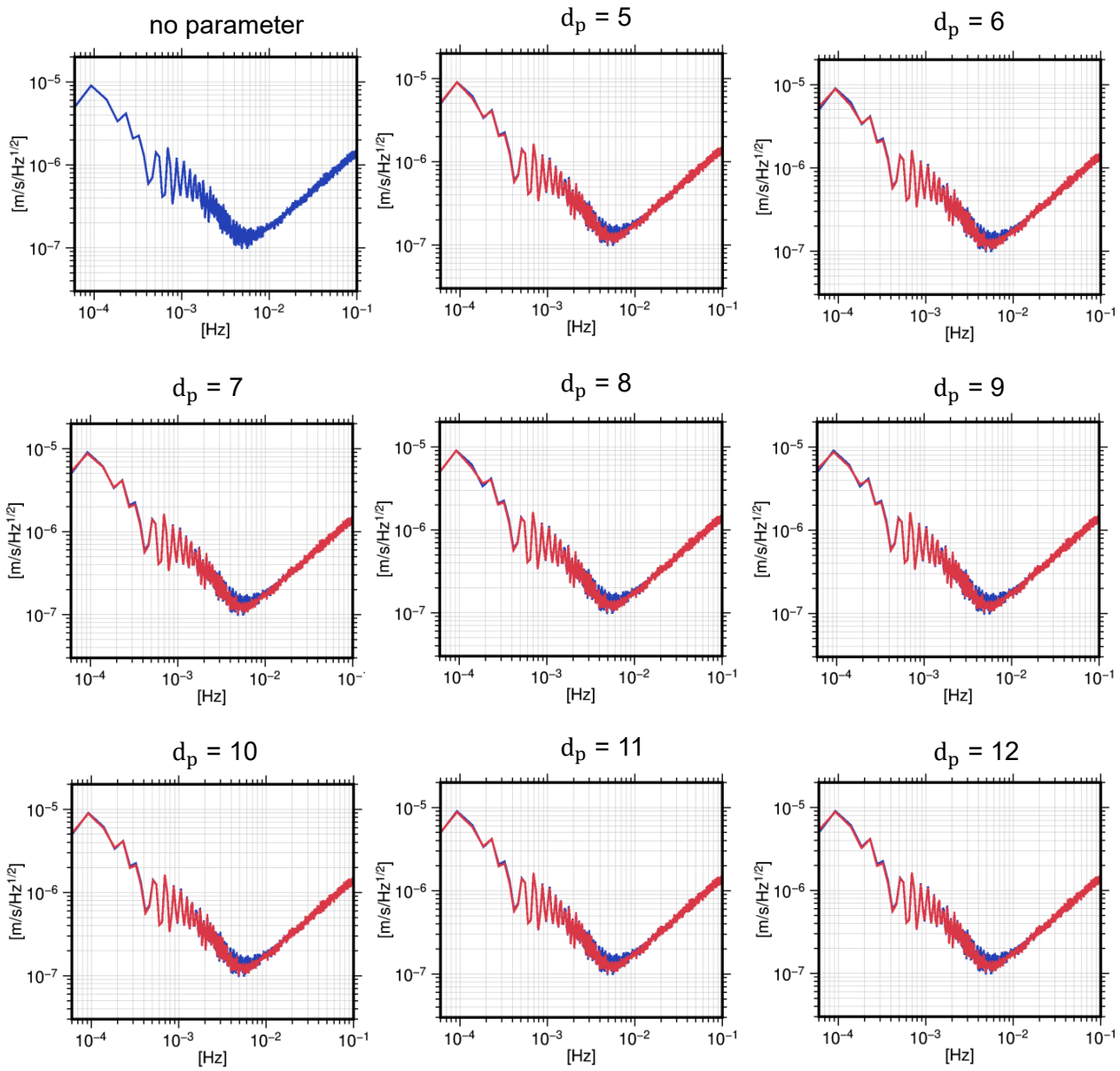

Figure 5.6.: $\sqrt{PSD}$ of the post-fit range-rate residuals from the ITSG-Grace2018 (prelim.) solution (blue) with no parametrization for eclipse transition events and the solutions with different polynomial degrees for eclipse transition waveforms (green) for November 2008. The minimum $\sqrt{PSD}$ has been reached with degree 5.

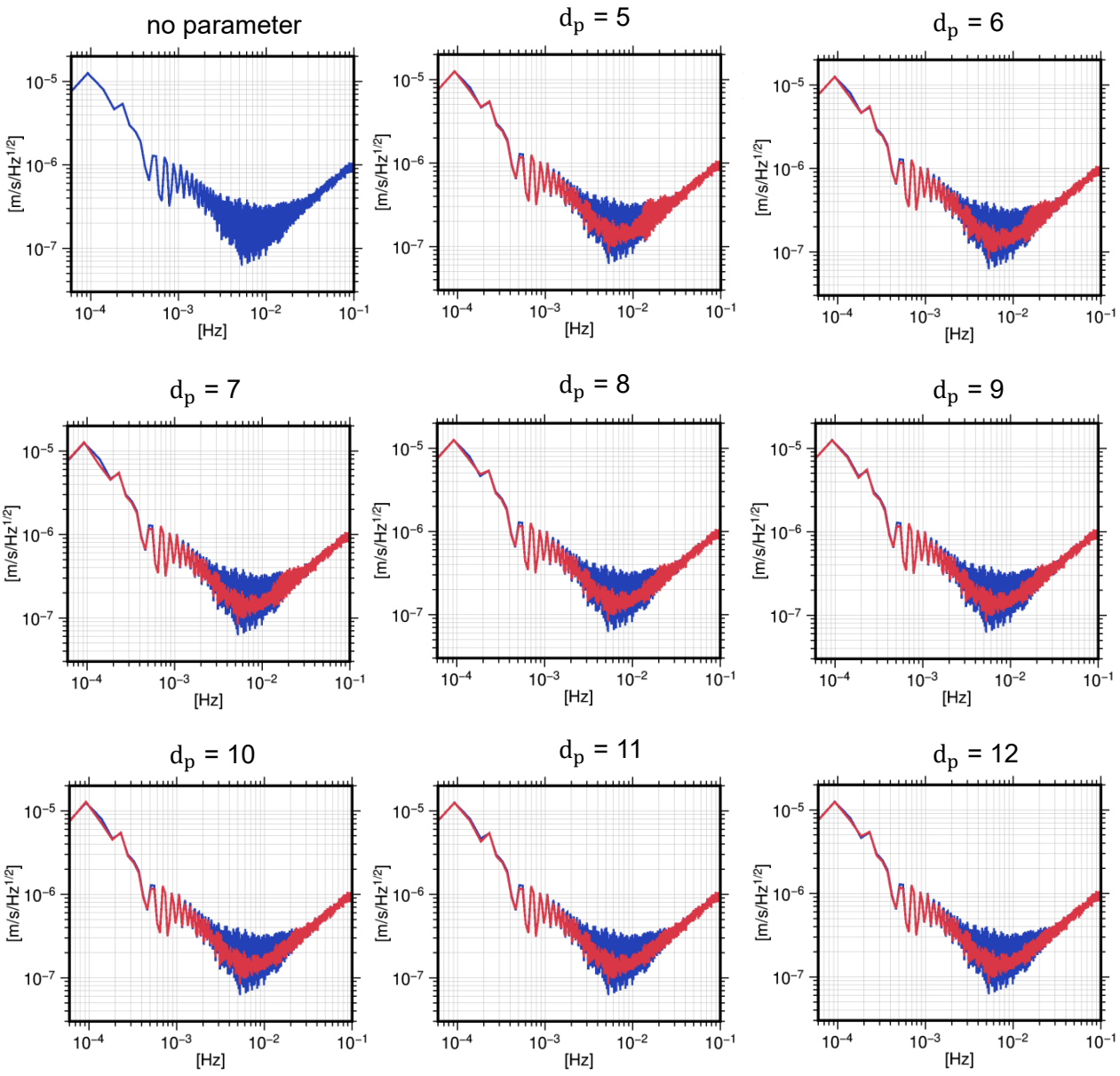

Figure 5.7.: $\sqrt{PSD}$ of the post-fit range-rate residuals from the preliminary ITSG-Grace2018 solution (blue) and the solutions with different polynomial degrees for eclipse transition waveforms (green) for May 2013. The minimum $\sqrt{PSD}$ has been reached with degree 11.

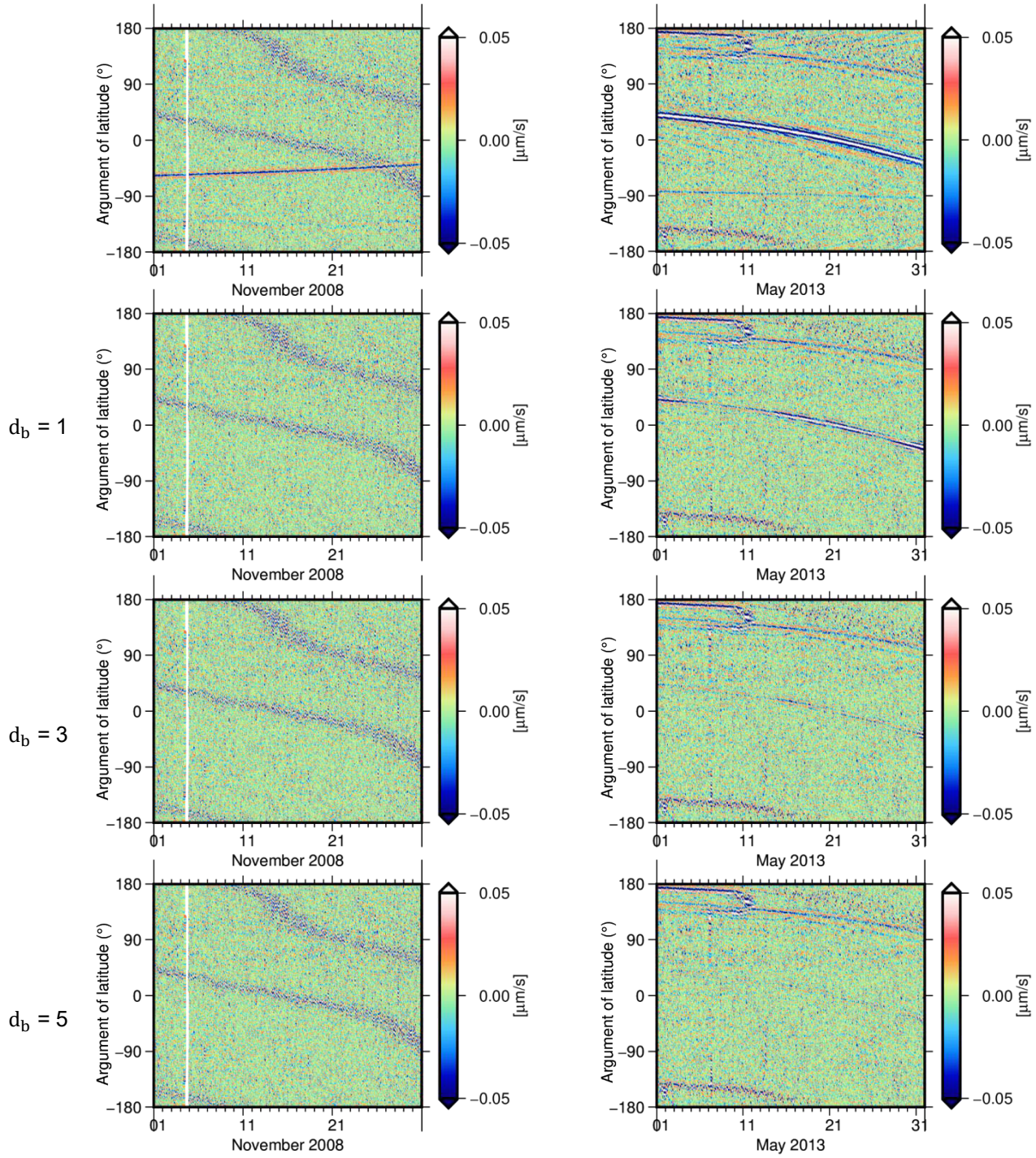

Figure 5.8.: Intermediate timescale details of the residuals obtained from the preliminary ITSG-Grace2018 solution with no parametrization (top panel) and the solutions with different B-spline degrees. The results are shown for two representative months November 2008 (left) and May 2013 (right).

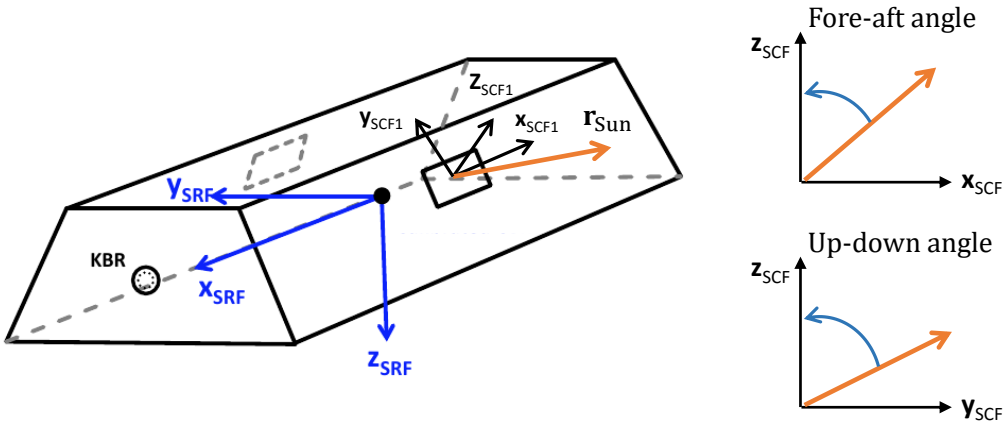

Figure 5.9.: Star camera head onboard a GRACE satellite with corresponding star camera frame, and the relative fore-aft and up-down angles in star camera FOV (Harvey et al., 2017a).

5.3.1. Relative angles and field of view

As described in Section 4.4, during each orbital path, occasionally one of two star cameras field of view (FoV) is blinded by the Sun. Under this condition, the blocked star camera head is temporary unavailable, and the attitude data is determined by the valid data from the other head. According to Harvey et al. (2017a), the change from combined attitude solution to a single head solution cause additional processing demand on IPU, which inevitably cause disturbances on the near-located KBR assembly. This transition period can be physically modeled by considering a time interval before and after the full blinding condition.

The star camera heads are placed on the side panels, with a zenith offset of $\pm 45°$. Figure 5.9 schematically shows the placement of star camera heads as well as the corresponding star camera frame w.r.t SRF. The rectangular FoV is defined in star camera frame in terms of the relative angles, including 19° fore-aft angle and 14° up-down angle. The definition of the relative angles can also be found in Figure 5.9.

The time interval of partial blinding can be determined with an initial outer ring for the FoV. Instead of using the actual FoV for the parametric model, a rectangular field with 20° fore-aft angle and 17° up-down angle is chosen, as shown in Figure 5.10, as it matches better with the pattern of the artifacts in the residuals.

Furthermore, the rectangular field is separated in six parts, as each part has a unique waveform in the residuals. The first four parts are considered for the horizontal edges where the up-down angle is close to $\pm 8.5° \pm \Delta\alpha$, with $\Delta\alpha$ being an angle margin:

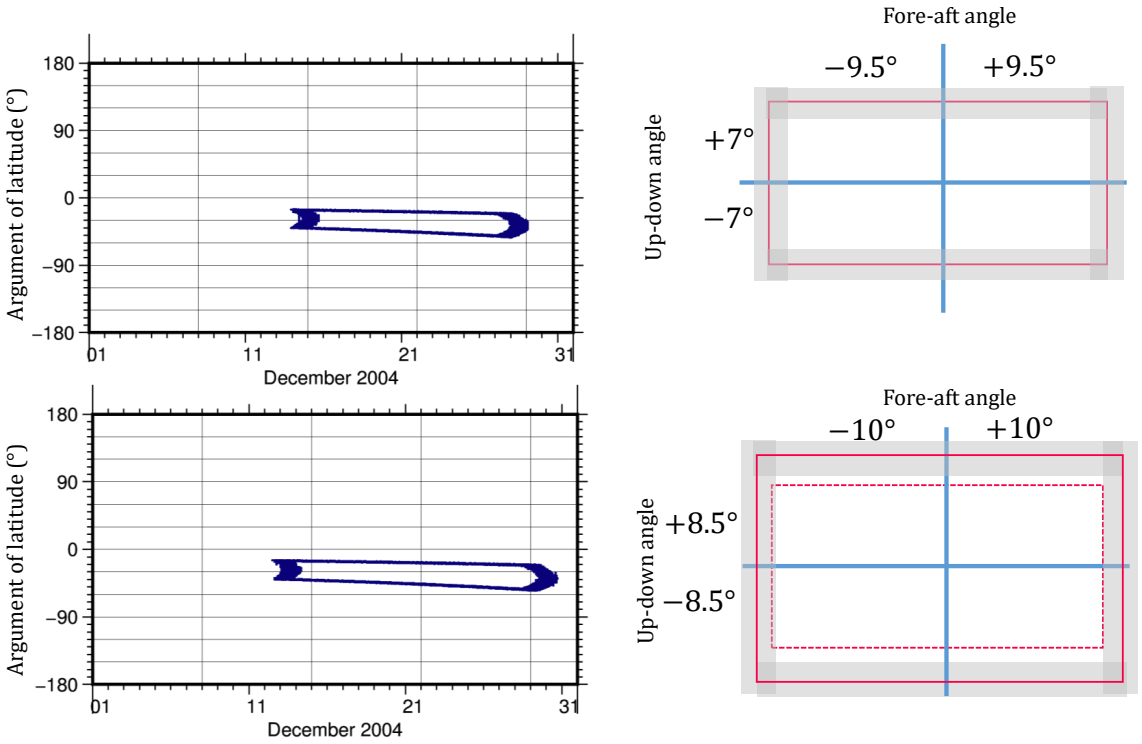

Figure 5.10.: The actual (top) and modeled (bottom) star camera FoVs, plotted w.r.t the GRACE-A argument of latitude for December 2004 (left panel) and their corresponding rectangular field (right panel).

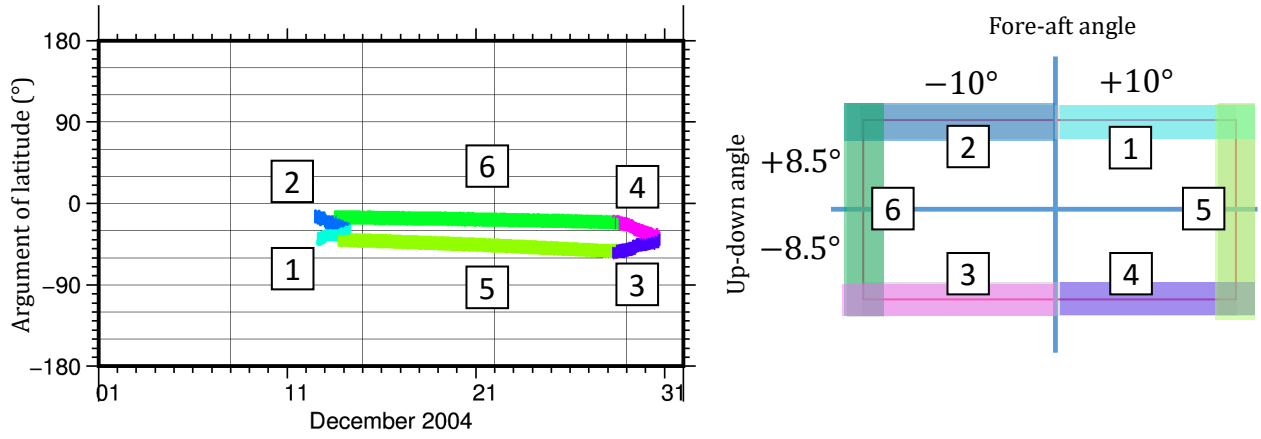

Figure 5.11.: The parametric model for sun intrusion events, plotted w.r.t the GRACE-A argument of latitude for December 2004. The model consist of 6 parts, with each part representing a complete or half of an edge of the FoV.

1: Positive up-down angle, Positive fore-aft angle,
2: Positive up-down angle, Negative fore-aft angle,
3: Negative up-down angle, Positive fore-aft angle,
4: Negative up-down angle, Negative fore-aft angle,

And the final two parts describe the vertical edges, where the fore-aft angle is close to $\pm 10^\circ \pm \Delta\alpha$, with $\Delta\alpha$ being an angle margin:

5: Positive fore-aft angle,
6: Negative fore-aft angle,

Figure 5.11 shows the time interval of the 6-folded model for an arbitrary month.

5.3.2. Parameter adjustment

Based on the pre-determined time intervals, six separate temporal functions are set-up in the observation equations. As the variation of the artifacts and their amplitude are consistent throughout the mission, it is sufficient to adjustment the model for one month. Therefore the parameters are established for December 2004, i.e. a month during high-quality data period of GRACE. In this month, with a low noise on ACC and SCA data, the KBR systematic errors are isolated. Therefore, after mitigating the eclipse transition errors, the effect of the under-study parametrization for Sun intrusion events can be better understood. As mentioned before, polynomial and B-spline degree have been chosen identical to the eclipse transition models, with $d_p = 11$

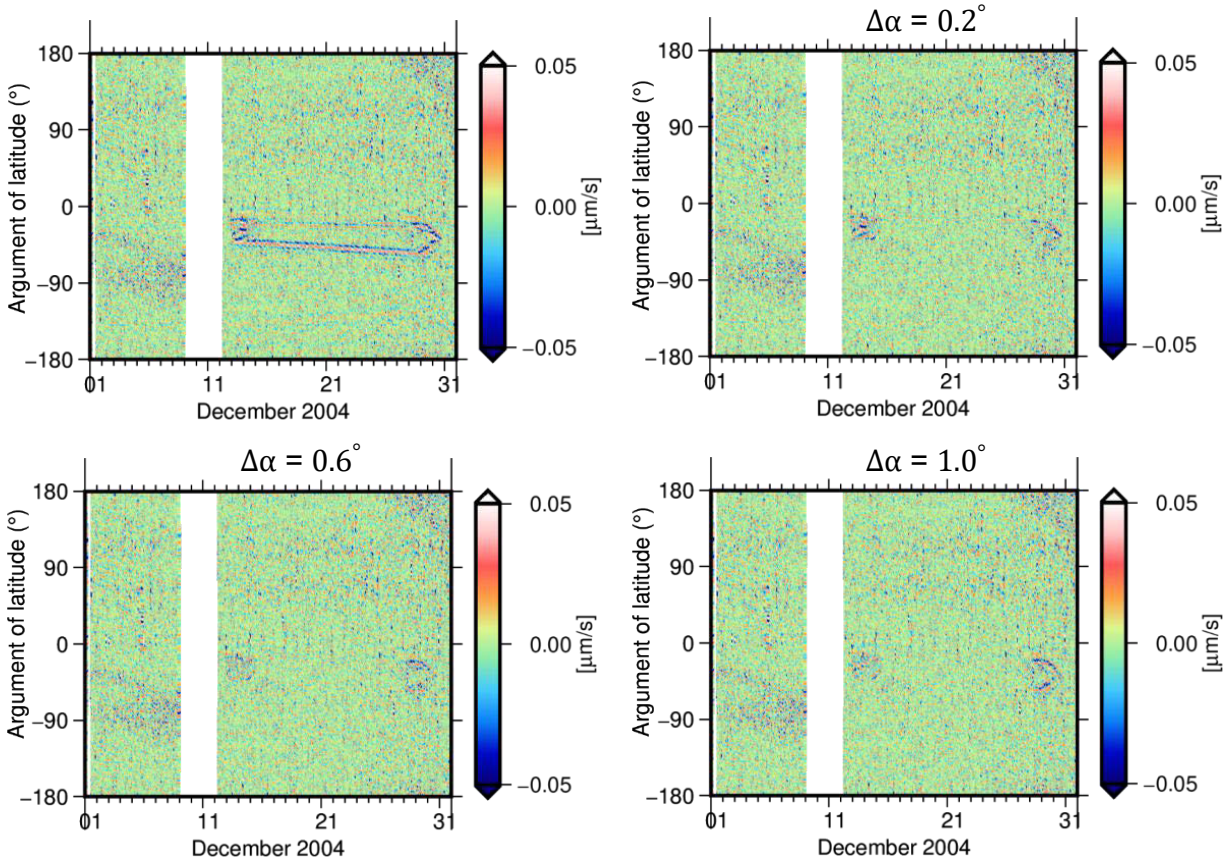

Figure 5.12.: Intermediate timescale details of the residuals obtained from ITSG-Grace2018 solution with no parametrization (top panel left) and the solutions with different $\Delta\alpha$. The results are shown for December 2004.

and $d_b = 5$. Keeping these parameters constant, the modeling is focused on the effect of $\Delta\alpha$. Figure 5.12 shows the impact of increasing $\Delta\alpha$ on the range-rate residuals. It can be concluded that choosing a $\Delta\alpha = 0.6°$, is the best fit for modeling the partial blinding condition, as increasing the angle margin introduce more artifacts to the observations. Using the final parametrization, the range-rate residuals in frequency range of 3 to 10 mHz for December 2004 are reduced by 2 percent.

5.4. Impact on gravity field

The developed method for modeling the KBR systematic errors, described in Section 5.2 and Section 5.3, has been implemented in ITSG-Grace2018 model. To study the

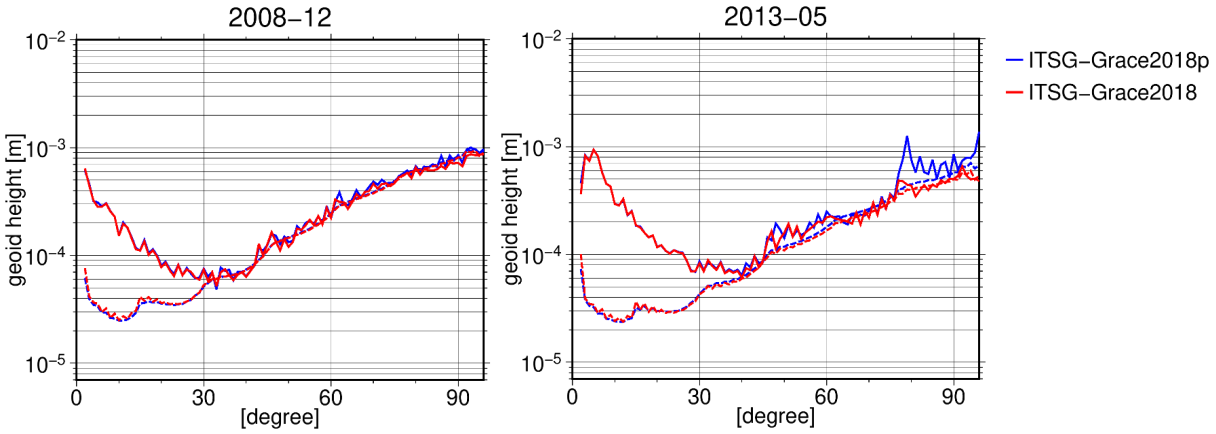

Figure 5.13.: Degree amplitudes of coefficient differences of the ITSG-Grace2018p and ITSG-Grace2018 solutions for December 2008 (left) and May 2013 (right) w.r.t the GOCO06s model.

impact of this method, this section compares the full degree and order gravity field solutions computed with no KBR parameter for the aforementioned errors, denoted as preliminary solutions or ITSG-Grace2018p, and with the final solutions, denoted as ITSG-Grace2018, based on the full parametrization scheme.

5.4.1. Degree amplitudes

Figure 5.13 shows degree amplitudes for two representative months, December 2008 and May 2013. For December 2008, which is a representative of the months with high quality data, the solution computed based on full parametrization scheme is almost identical to the preliminary solution, with small improvement for degrees over 60.

The improvement is more pronounced for May 2013 in degree and order above 40. The full parametrization scheme shows much smaller amplitudes at very high degrees, where noise is expected to dominate the recovered signal. In general, this can be seen for most of the months affected by the eclipse transition errors, which are not shown here.

5.4.2. Spatial domain

Figures 5.14 shows equivalent water height maps for the same two representative months from different GRACE period. The reference static field, trend, and annual signals from the GOCO06s model were removed from the monthly solutions. A Gaussian filter was applied with 250 km radius to remove high-frequency strips. It can

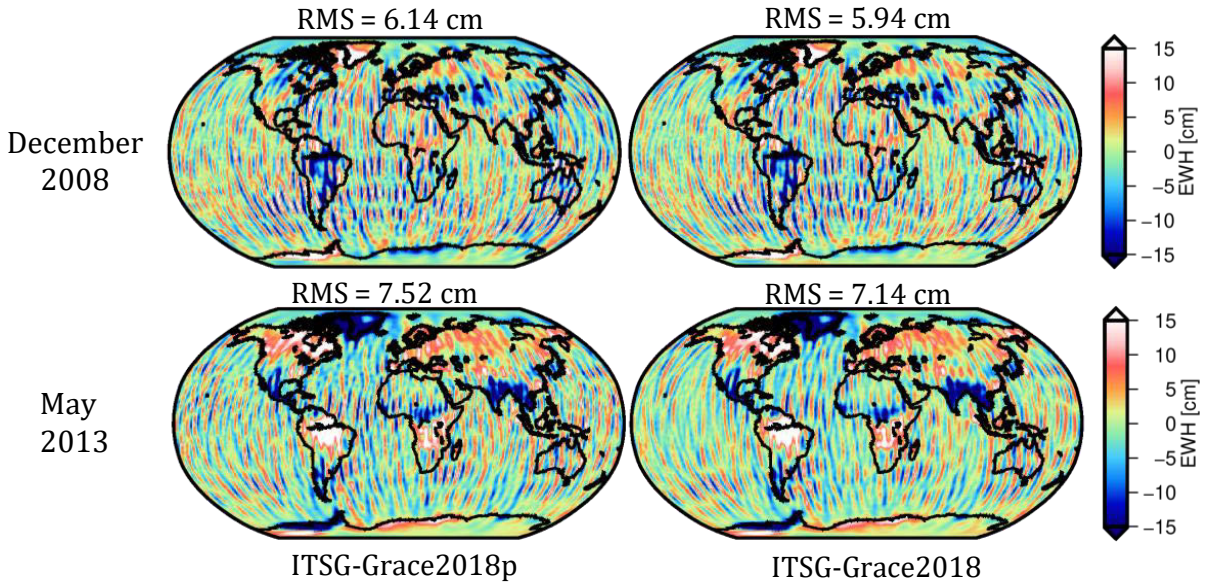

Figure 5.14.: Temporal RMS of the ITSG-Grace2018p and ITSG-Grace2018 solutions for December 2008 and MAy 2013. Before computation of the RMS, the static field, annual cycle and trend of GOCO06s were reduced and a 250 km Gaussian filter was applied to each solution.

be seen that for May 2013, a majority of north-south strips, in particular in the ocean area, is resolved with the proposed KBR parametrization.

5.4.3. Ocean RMS

Figure 5.15 shows the differences between corresponding time-series of ocean RMS for the two set of solutions in percentage. Before computing the RMS, the annual cycle and trend of GOCO06s were reduced and a 300 km Gaussian filter was applied to each solution. Furthermore, the C20 coefficient is excluded from all solutions. In this figure, the positive values show a reduction in RMS of the final solutions. Note that the last seven months of GRACE are excluded, due to the reduced quality of the gravity fields.

For most of the months, the time-series derived from the full parametrization scheme shows reduction of noise level. The benefit of the parametrization is significant for the months after 2012, with a maximum of 17 percent reduced RMS for May 2013. On the other hands, for a number of months, the parametrization slightly increases the RMS over the ocean. The negative values only amounts to 2 percent in average, equivalent to 1-2 mm. This is not a significant change in the quality of the gravity fields for these months.

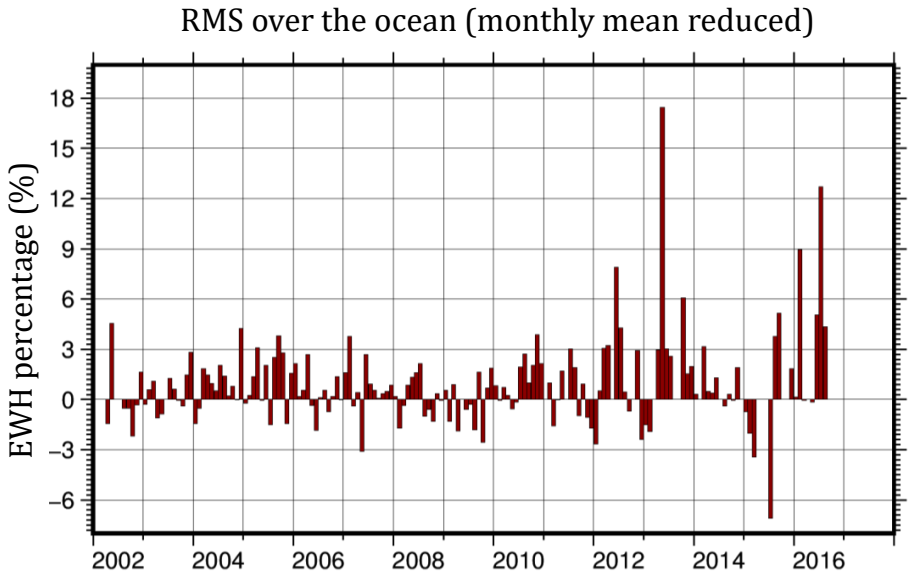

Figure 5.15.: Percentage of differences between temporal RMS of the ITSG-Grace2018p and final ITSG-Grace2018 solutions. The positive values indicates reduction of RMS values in the final solution.

5.5. Summary

The aim of this chapter was to mitigate the investigated KBR systematic errors in Chapter 4. These errors cannot be described by using the stochastic noise model estimated in ITSG-Grace2018, nor can they be calibrated at the observation level, as they are superimposed with the actual gravity signal. To reduce these errors from the observations, a parametric model is developed and tuned for each type of these disturbances.

For the ITSG-Grace2018 release, the proposed parametrization not only contributes to residual reduction at these specified events, but also improves the estimates of gravity field parameters. Depending on the month under study, the proposed parametrization improves the solution up to 17 percent RMS over the oceans.

Concerning the proposed parametrization approach, further investigation is required for more realistic set-up. As previously mentioned, the proposed approach tries to mitigate the impact of the systematic errors on the gravity field recovery and cannot completely eliminate these errors. Therefore, their effect is not perfectly resolved for every month. However, further improvement in the model would have a negligible effect on the gravity field solutions recovered.

Single accelerometer gravity field recovery

6

Attribution This chapter of the dissertation which describes a novel approach for recovery of the degraded GRACE-D accelerometer data, is a revised edition of the publication Behzadpour et al. (2021) by the author. This chapter discusses the methodology and mainly focuses on the impact of the synthetic accelerometer data on the gravity field solutions, diving into more details explained in Section 5.3 of the respective paper.

GRACE-FO mission was launched in May 2018 to continue GRACE mission objective, i.e. to observe large-scale mass redistribution in the Earth system. Shortly after launch, the noise on GRACE-D accelerometer measurements increased, resulting in systematic data degradation. As a result, GRACE-D data was required to be replaced by synthetic data obtained from GRACE-C measurement, a procedure known as data transplant.

This chapter describes a novel method for recovering GRACE-D accelerometer data, developed at TUG. The novelty of the approach is to use the state-of-the-art non-gravitational force models in the recovery process. This allows for the computation of an improved calibrated accelerometer data (ACT) product, which reduces the ACC corresponding error in the recovered gravity field.

6.1. Introduction

Each individual spacecraft of GRACE-FO mission (Landerer et al., 2020) is equipped with an on-board accelerometer that provides accurate measurements of the non-gravitational forces, such as drag, SRP, and ERP. These measurements are required to separate any non-gravitational effect from the sought-after gravitational perturbations on the satellite motion. Therefore, accuracy in the accelerometers data, denoted as ACC products, is critical to the gravity field recovery and significantly affects the quality of inter-satellite ranging measurement capabilities.

According to McCullough et al. (2019), the ACC measurements from both satellites are contaminated by various sources of noise. As a result, the standard processing established for GRACE Level-1A to Level-1B conversion (Wu et al., 2006) does not

provide accurate outputs for gravity field recovery. For this reason, the GRACE-FO Science Data System (SDS) team alternated the standard processing and introduced a series of calibration processes for each satellite. Therefore, instead of ACC1B, the calibrated GRACE-FO accelerometer data (ACT1B) products are provided for the purpose of gravity field determination (Harvey et al., 2022; McCullough et al., 2019).

For the early days of the mission, i.e. until 2018-06-21, the same calibration technique is applied to both accelerometer data. This includes extracting large spurious accelerations, known as Phantom accelerations, from the data and replacing improper thruster response accelerations with model-based responses.

From 2018-06-21, GRACE-D ACC was observed to have substantially increased noise on all three axes, thus the measured data could not be used directly and was subject to further investigation. Therefore, for the initial data release, denoted as RL04, the SDS replaced the original GRACE-D ACC data with synthetic data, the so-called transplant data.

The SDS transplant data are derived from the GRACE-C accelerometer measurements, assuming that the co-orbiting satellites experience similar non-gravitational accelerations, referenced to their body frame, with a short delay of 25-30 seconds. Therefore, the GRACE-D accelerations can be derived from the available accelerometer measurements from GRACE-C using time and attitude corrections, to account for the distance between the two satellites and the orientation differences relative to each other.

The ACC data transplant was originally developed for the GRACE mission (Save et al., 2006). The demand for a single accelerometer solution initially raised in the beginning of the mission, namely in 2002 and 2003. During this time, only GRACE-A accelerometer data was available for several weeks (Save et al., 2006). Similar situation happened at the end of the mission, with the GRACE-B accelerometer being shut down due to the reduced battery capacity. For the final months, Bandikova et al. (2019) improved the transplant approach, by introducing a set of models for residual accelerations due to thruster activities. Instead of using a statistical estimation (McCullough et al., 2015; U. Meyer et al., 2011), Bandikova et al. (2019) determined the dynamic system of each thruster and computed the corresponding impulse response they induce on all three axes. This approach improved the resulting gravity field substantially, and therefore, ACC transplant data became a part of the official Level-1B products during the final months.

The main assumption of the original transplant procedure is the equivalence of the non-gravitational forces acting on each satellite in the same orbit position. U. Meyer et al. (2011) previously evaluated this assumption for GRACE mission, when both accelerometers operated nominally and provided high-quality data. They showed that the assumption does not hold for two specific conditions: first when for a short

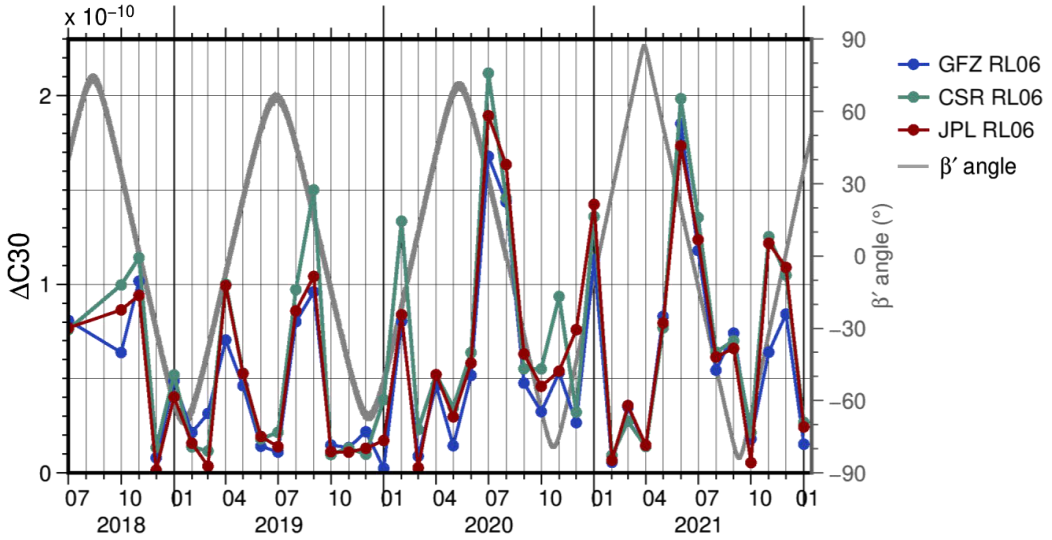

Figure 6.1.: Absolute value of the difference between GRACE-FO derived and SLR derived C_{30} coefficient. During the periods with low β' angle ($\beta' \sim 0°$), GRACE-FO derived values exhibit large offsets w.r.t SLR derived values.

period of time, satellites are transiting through Earth's shadow, as the SRP changes for each satellite at the same position, and second, when satellites are under direct Sun exposure, i.e. when β' angle of the orbit is close to zero. During these periods, each satellite experiences different drag force, due to high fluctuations in the atmosphere density. Thus, the current solution for GRACE-D ACT data has large errors under these conditions.

The resulting Level-2 data from SDS ACT data proves this hypothesis. The monthly gravity fields during low angle condition ($\beta' \sim 0°$) exhibit higher noises and the low degree zonal harmonics, in particular C_{30}, are affected by the current transplant approach. Figure 6.1 shows the absolute difference between C_{30} values reported in SDS Level-2 products and SLR-derived values, reported in Technical-Note 14 (TN-14; Loomis et al. (2020)). It is clear that the occurring maximum values are correlated with $\beta' \sim 0°$.

The main goal of this chapter is to propose a new method for recovering GRACE-D accelerometer data that incorporates non-gravitational force models, resulting in an alternative ACT1B product, denoted as TUG ACT1B. In the following, the details of the alternative approach and resulting data products as well as their impact on the gravity field are discussed.

6.2. GRACE-FO ACC data products

GRACE-FO accelerometer data are reported in three types of science data products:

6.2.1. ACC1A

The ACC Level-1A (ACC1A) data are the raw 10-Hz linear and angular acceleration measurements. These products reported in accelerometer reference frame (cf. Appendix A), whose origin is the center of mass of the proof mass and the axes are parallel to SRF. The ACC1A data are generated on a daily basis, in the time frame determined by the on-board computer (OBC).

6.2.2. ACT1A

Early studies on ACC1A data revealed different noise characteristics on the measurements of each accelerometer. Therefore, to obtain an optimal gravity field, each set of ACC1A data required a specific series of calibration processes. This results in the calibrated accelerometer data (ACT1A) products (McCullough et al., 2019).

In case of GRACE-C and early days of GRACE-D, the calibration process includes removing spurious phantom accelerations and replacing un-realistic thruster responses with model-derived values. For GRACE-D ACC data, however, these processing steps were not sufficient after the noise elevation on 2018-06-21. As a result, the initial release of GRACE-D ACT1A data contained transplant data from GRACE-C and the degraded measurements became a subject for further investigations (Harvey et al., 2022; McCullough et al., 2019). ACT1A data have similar format to ACC1A, generated on a daily basis with 10-Hz sampling, reported in accelerometer frame and OBC time. It should be mentioned that ACT1A data only include linear accelerations and the angular accelerations are set to zero from this level.

6.2.3. ACT1B

For GRACE-FO, ACT Level-1B (ACT1B) is the final Level-1 product which serves as input for the gravity field recovery. ACT1B data have 1-Hz sampling, given in SRF and GPS time. In order to derive the final product, ACT1A accelerations are edited, converted and filtered by the standard GRACE Level-1A to Level-1B processing (Wu et al., 2006). This processing is explained in details in Section 6.3.

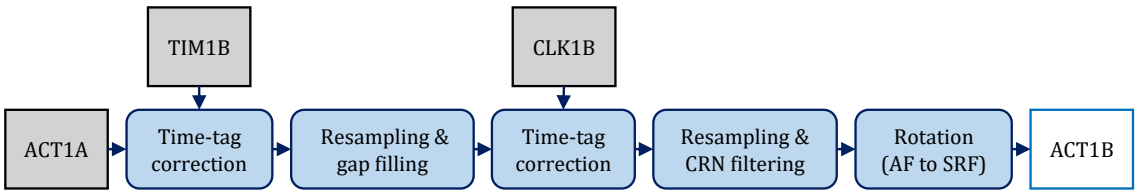

Figure 6.2.: Schematic view of ACT1A processing. The processing involves a series of editing, re-sampling, filtering as well as frame and time conversions.

6.3. ACT Level1-A processing

The GRACE-FO initial data release included Level-1A data products, for the first time. This is an opportunity for all processing centers to set-up an alternative Level-1A processing, based on Wu et al. (2006). The processing of linear accelerations from Level-1A (ACT1A) to Level-1B (ACT1B) accelerometers is explained in the following.

The process can be divided into 5 steps, as shown in Figure 6.2. Initially, Level-1A accelerometer (ACT1A), clock (CLK1B), and time (TIM1B) data products are read and converted into internal formats. During the conversion, any flagged data, tagged with "no pulse sync" or "invalid timetag", are excluded. The time transformation starts with the conversion of time-tags from OBC time to receiver time, using the TIM1B data product. The data are then re-sampled to integer multiples of 0.1 s (10 Hz) with linear interpolation. The data gaps are also filled with up to 200 data points on each side of the gap using cubic interpolation. There is no filling if the data gap is more than 100 s. The details of the linear interpolation algorithm is explained in Wu et al. (2006).

As the second time correction, the GPS time correction is derived. The accelerometer time tags, being in receiver time at this stage, are converted to GPS time. This has been done by linearly interpolating the clock corrections from the CLK1B data product. If no valid clock correction data exists for a given time span, the clock corrections are extrapolated to ensure the continuity of the ACC data. This time correction step also is followed by a re-sampling process. The accelerations are again re-sampled to integer multiples of 0.1 s using a Lagrange quadratic interpolation over the nearest 3 data points. The details of the Lagrange interpolation algorithm is explained in Wu et al. (2006).

At this point, the output is ready for filtering as the sampling is equidistant. The filtering is carried out with a digital CRN filter of 7th order self-convolution with 35 mHz bandwidth, covering 140.7 s around the data epochs. After filtering, the sampling is reduced from 0.1 s to 1 s.The processing is finished with a reference frame transformation from AF to SRF.

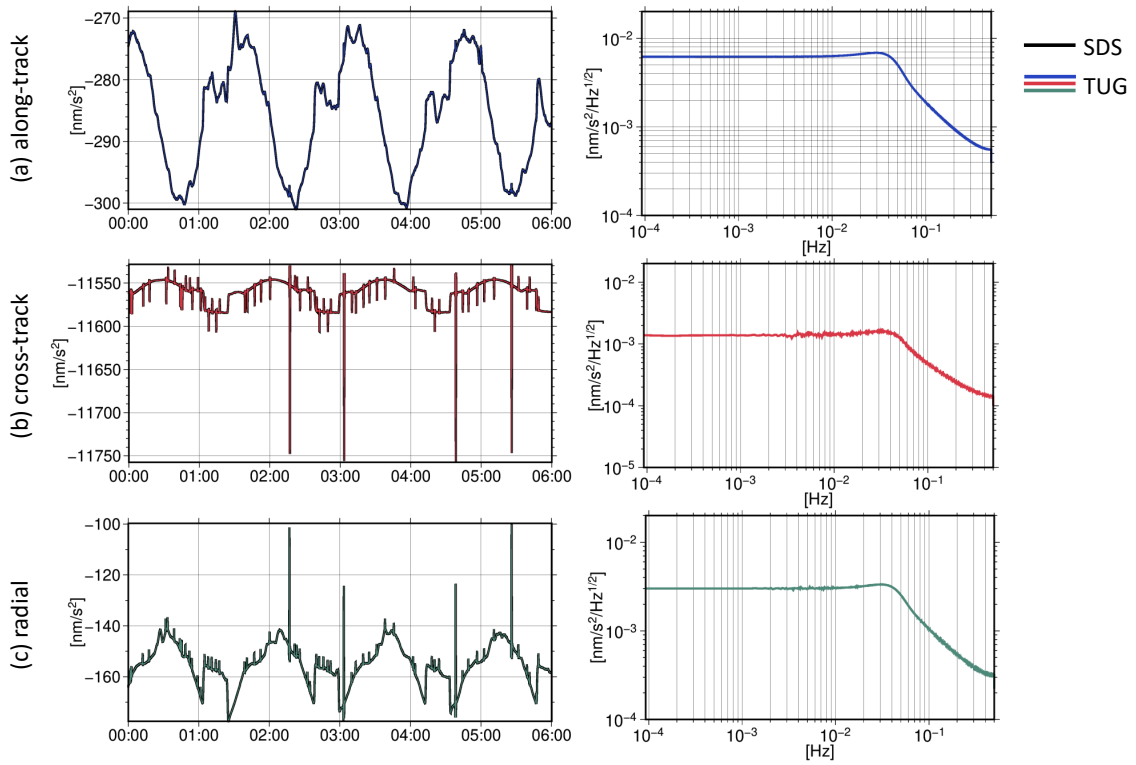

Figure 6.3.: Validation of the GRACE-C TUG ACT1B and the SDS ACT1B on 2019-01-01. The left panels compare the time-series and the right panels compare $\sqrt{PSD}$ of their differences in (a) along-track, (b) cross-track, and (c) radial directions.

During the course of this study, each step of the described algorithm has been implemented in GROOPS. As a result, in addition to the officially released product, an independent ACT1B product, denoted as TUG ACT1B, is obtained. Figure 6.3 compares these products with the official SDS ACT1B data. The time-series of both products match perfectly on each axis and their differences are negligible, as they are more than one order of magnitude smaller than the instrument noise (cf. Section 2.3). This validates the GROOPS implementation of the process, which is an important milestone for the rest of this study.

6.4. GRACE-D ACC recovery

In this section, the novel recovery process for linear accelerations from GRACE-C ACT1A to GRACE-D ACT1B is explained. The process is summarized in Figure 6.4. In addition to the data products mentioned in Section 6.3, the following data products also serve as input to this process:

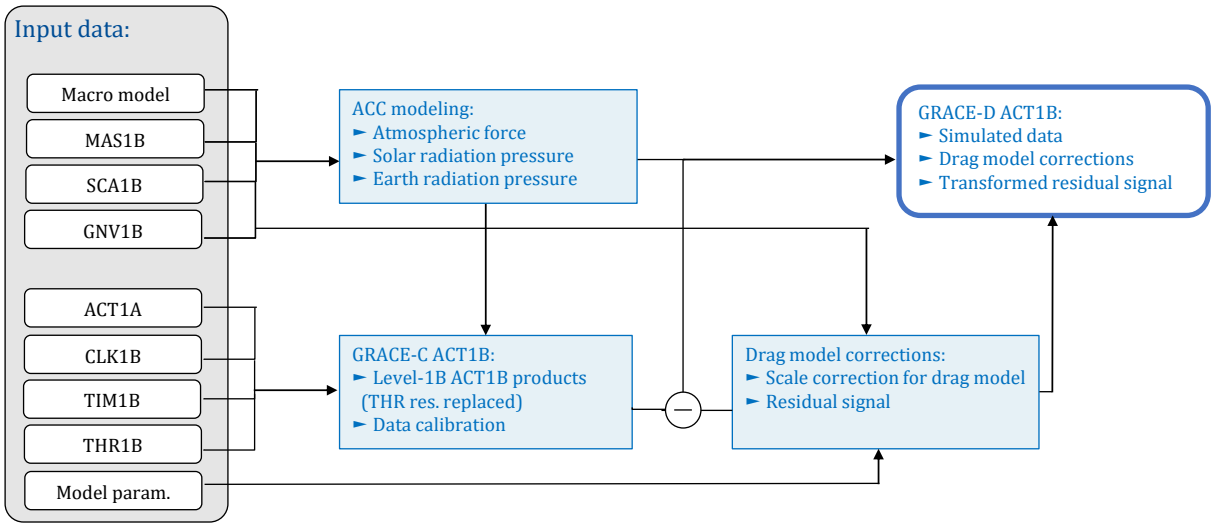

Figure 6.4.: Schematic overview of the proposed method for GRACE-D accelerometer data recovery.

GNV1B 1-Hz satellite position and velocity in Terrestrial Reference Frame (TRF) and GPS time,
SCA1B 1-Hz Attitude quaternion data for rotation from Inertial Frame to SRF,
THR1B Thruster activation time and firing duration in GPS time.

In the first step, the standard Level-1A processing (cf. Section 6.3) is performed on the daily GRACE-C ACT1A with an additional step: Before filtering the data with the CRN filter, residual accelerations due to thruster activities need to be removed. This is because these accelerations only correspond to the thruster firing events on GRACE-C. Therefore, these events are marked with GRACE-C THR1B products and are removed with a margin of 1 s. The resulting gaps are then filled with linear interpolation.

6.4.1. Calibration and Model reduction

The next step is to simulate linear accelerations, according to force models mentioned in Section 3.2. The simulated data are computed for both satellites. As GRACE-FO GNV1B and SCA1B data have 1-Hz sampling, the resulting simulated data also have the same sampling. Using these simulated data, GRACE-C ACT1B data can be calibrated with a constant daily bias on each axis, following the first step of the calibration approach introduced by Klinger and Mayer-Gürr (2016b). Figure 6.5 compares the simulated data and the bias-corrected ACT1B for GRACE-C on two different days with different β' angles. In general, there is a good agreement between the simulated and the

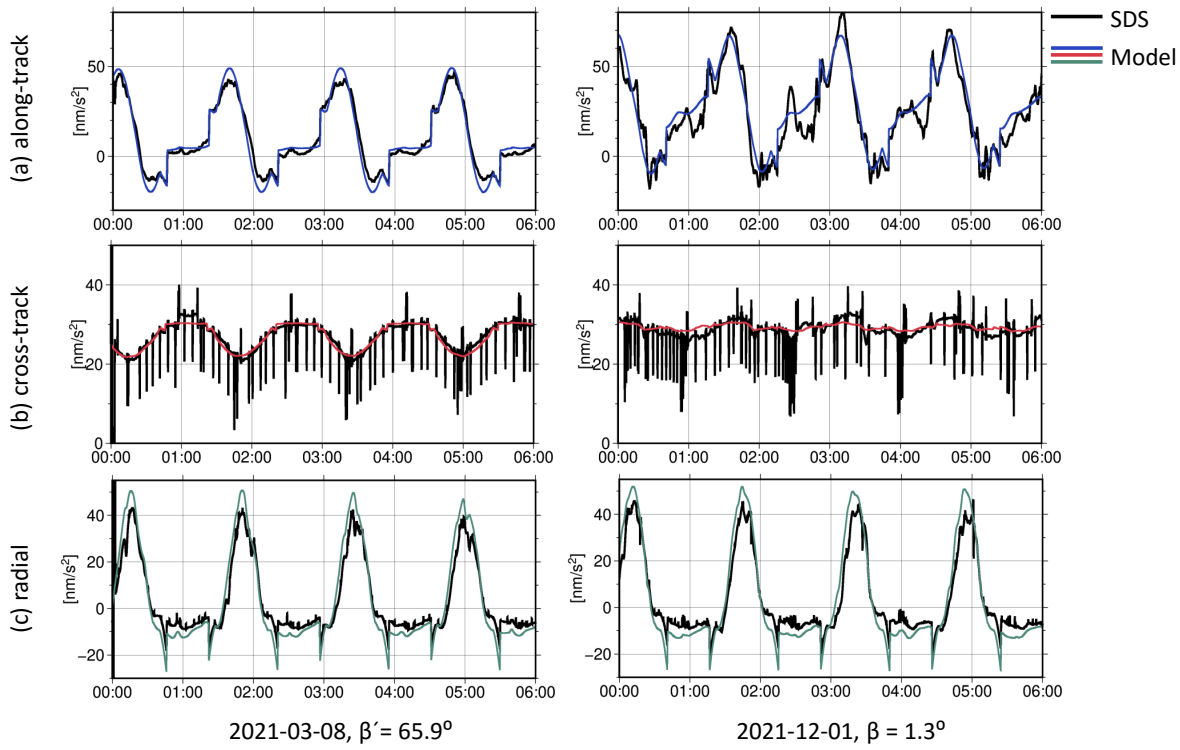

Figure 6.5.: Comparison between bias-corrected GRACE-C ACT1B and simulated data in (a) along-track, (b) cross-track, and (c) radial directions on 2021-03-08 (left) and 2021-12-01 (right).

measured data. However, under $\beta' \sim 0°$ condition, when satellite experiences higher solar radiation pressure, the simulated data deviate more from the measurements.

The difference between the calibrated ACT1B and the modeled data is basically the part of the signal which could not be explained by the models. Therefore, to fully exploit the information obtained by the GRACE-C accelerometer, this part of signal needs to be transferred to the GRACE-D frame. To this end, the simulated data $\boldsymbol{a}_{model}$ are subtracted from the calibrated GRACE-C data $\boldsymbol{a}_{cal}$,

$$\Delta\boldsymbol{a} = \boldsymbol{a}_{cal} - \boldsymbol{a}_{model}. \tag{6.4.1}$$

which gives the unmodeled acceleration signal $\Delta\boldsymbol{a}$.

6.4.2. Time correction

To transfer the unmodeled accelerations from GRACE-C to GRACE-D, a transfer time correction is required. This is basically the time difference between GRACE-C passing

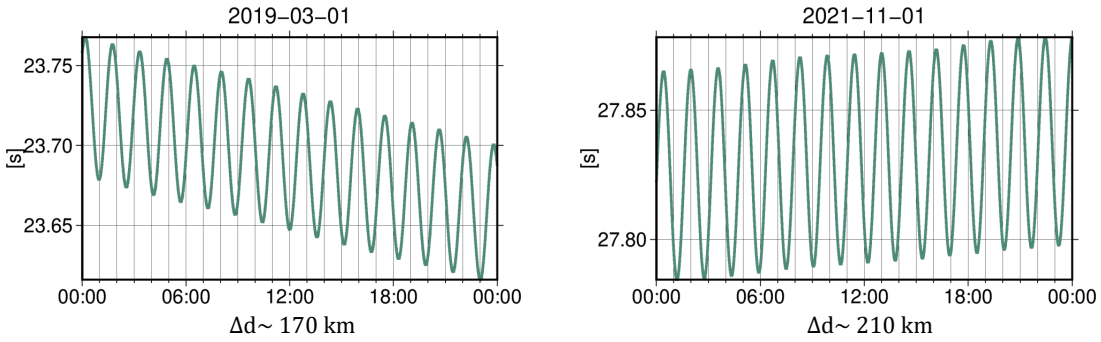

Figure 6.6.: Time correction from GRACE-C to GRACE-D on 2019-03-01 (left) and 2021-11-01 (right). Transfer time correction increases with the increasing distance between the two satellites.

at one orbital point and GRACE-D passing through the same. The same correction is also necessary for other GRACE-C Level-1B data, namely GNV1B and SCA1B, for the next steps. The transfer time correction at each epoch t_i is derived as follows:

Let each satellite positions and velocities be given as $\boldsymbol{r}_{C/D}(t_i)$ and $\dot{\boldsymbol{r}}_{C/D}(t_i)$ in inertial frame respectively. The distance between two satellites at each epoch can be obtained by:

$$\Delta d = |\boldsymbol{r}_C(t_i) - \boldsymbol{r}_D(t_i)| \,. \tag{6.4.2}$$

Given the velocity $\dot{\boldsymbol{r}}_D(t_i)$, Δd divided by this velocity can be used to estimate the transfer time correction. Figure 6.6 shows the derived transfer time correction for two arbitrary days with different Δd. It is clear that the transfer time increases with expanding separation between the satellites.

6.4.3. Drag model correction

The unmodeled acceleration signal contains errors due to mismodeling drag force, SRP, ERP, as well as other unknown contributions. Since the drag force has the largest uncertainties among the non-gravitational forces acting on a LEO satellite (cf. Section 3.2), it is safe to assume that the unmodeled accelerations represent the unmodeled dynamics of the drag force model. Generally, this model has high uncertainties due to the errors in:

(a) state and attitude of the satellite,

(b) modeling the interaction of the satellite's surface and atmosphere molecules, which affects the drag coefficient,
(c) atmospheric density models.

The variations of drag coefficient and density cause an unknown multiplicative error $S_D = \rho \cdot C_D$, i.e. a scale factor consisting of atmospheric density ρ and drag coefficient C_D. To take these variations into account, a time variable scale factor can be estimated using the unmodeled acceleration and the simulated drag model, i.e eq. (3.2.1), for GRACE-C in a least square adjustment:

$$\Delta \boldsymbol{a} = \frac{\partial \boldsymbol{a}_D}{\partial S_D} \cdot S_D, \tag{6.4.3}$$

where

$$\frac{\partial \boldsymbol{a}_D}{\partial S_D} = -\frac{1}{2}\frac{A_i}{m} \left\| \boldsymbol{v}_{TAS} \right\|^2 \hat{\boldsymbol{v}}_{TAS}. \tag{6.4.4}$$

To model temporal variations of the scale factor, S_D is estimated daily, using uniform cubic basis splines (UCBS), defined by degree $d = 3$ and the number of knot intervals k (cf. section 3.4.1). Here, a knot interval length of 1 min is chosen, which results in 1440 knots for each daily interval. As a result, the scale estimation requires a total of $k + d = 1443$ parameters per interval. This choice introduces a reasonable number of parameters while maintaining the adjustment problem's computation cost and stability.

After estimating the scale factor, which will be directly applied to the GRACE-D drag model, the residual signal, remaining from the scale estimation process, is obtained. The residual signal is a part of the GRACE-C measurements that can be explained neither by the force models nor by the drag scale factor. Therefore, to prevent any signal loss, it needs to be directly transferred to the GRACE-D frame using an attitude correction.

6.4.4. Attitude correction

The residual signal is initially measured in GRACE-C body frame. To transfer the signal from GRACE-C to GRACE-D frame, an attitude correction is required. This is due to the fact that each satellite's orientation w.r.t its velocity vector is different. The measurement concept of KBR requires precise alignment of each satellite's KBR

antenna towards each other, in the direction of LOS. Since the antenna is located on the front panel of each satellite, the leading satellite is rotated by 180° around its z-axis. In addition, both satellites fly with a pitch offset of about 1° w.r.t the LOS, to ensure precise inter-satellite pointing.

To transfer accelerations from GRACE-C to the GRACE-D frame, time-corrected GRACE-C SCA1B can be used to calculate the rotation matrix from GRACE-C SRF to the inertial frame. In the next step, the inverse rotation matrix, obtained from GRACE-D SCA1B data, is applied to rotate the data from inertial frame to GRACE-D SRF.

Note that using the actual data for attitude correction, introduces the attitude noise into the transplant procedure. Bandikova et al. (2019) mention that this approach is not feasible for GRACE data transplant, as high-frequency noise on the star camera data is much higher than the accelerometer data. As a result, they suggest an approximation method that estimates the attitude correction with a 180° yaw and a 3.2° pitch rotation.

However, the aforementioned attitude noise is not a problem for GRACE-FO. Each GRACE-FO satellite has three star cameras and one angular rate sensing inertial measurement unit (IMU) as attitude sensors. Using a Kalman filter, these attitude data are merged to produce an optimal attitude product (Harvey & Sakumura, 2019). This approach, according to Landerer et al. (2020), reduces noise level by about 2 orders of magnitude less than GRACE. Therefore, it enables the direct use of attitude data to transfer residual accelerations to the GRACE-D frame. The transformed residuals are added to the GRACE-D original force models and drag correction to achieve the GRACE-D recovered accelerometer. At the final step, GRACE-D modeled responses to attitude thruster firings are added to the GRACE-D recovered data, which will be discussed in the following.

6.4.5. Thruster spikes

The purpose of the cold-gas thruster system is to control the satellite's attitude. With an optimal design, this system should have no effect on the linear accelerometer data. The influence of cold-gas thruster activation, however, is clearly obvious in the ACC1A data acquired from both GRACE and GRACE-FO satellites (Frommknecht, 2007; McCullough et al., 2019; U. Meyer et al., 2011; Peterseim, 2014). U. Meyer et al. (2011) showed that the thruster spikes are actual accelerations rather than an anomaly in the data, and therefore have an important role in precise orbit determination and gravity field modeling.

According to Peterseim (2014), there are two possible explanations for why thruster events can be mapped into linear accelerometer data:

(a) A possible offset in the center of mass of the accelerometer proof-mass w.r.t the satellite's center of mass (CoM) induces linear accelerations during thruster activities. However, this hypothesis is less likely due to the regularly performed CoM maneuvers. These maneuvers keep the proof-mass within 100 micrometers of the satellite's CoM. Therefore, except for the two orbit maintenance thrusters, all attitude thrusters should only exert a torque on the satellite, resulting in only angular accelerations rather than linear accelerations.
(b) The most probable reason is a possible misalignment between the pairs of thrusters, or differences in their generated thrust or pulsing time.

From beginning of the mission, both accelerometers of GRACE-FO show unrealistic responses to thruster impulses, particularly roll thruster firings (McCullough et al., 2019). Figure 6.7 shows varying responses of both accelerometers to negative roll thruster firing with 50 ms duration. In contrast to GRACE, which shows consistent thruster responses, one cannot see such deterministic behaviour for GRACE-FO accelerometers. Early studies also showed higher errors on the gravity field solutions due to these inconsistent responses, proving that these accelerations are, in fact, unrealistic. Harvey et al. (2022) suggest that the inaccurate impulse responses are caused by aliasing in the analog–digital converter, although this hypothesis is subject to further studies.

The accelerometers respond more realistically to long thruster firings. Therefore, SDS developed a model for Level-1A thruster responses, using the steady-state response at long firings. To improve the results, they also operated a series of "plateau tests" on both satellites, which are manual thruster firings with duration of 1 s. The developed model defines the amplitude of a unit pulse function, specified for each thruster type and each direction, as shown in Table 6.1.

It is also possible to obtain a Level-1B thruster response dataset. To this aim, in the TUG transplant approach, two processed GRACE-D ACT1B time-series are computed: For the first data, the standard Level-1A processing is applied to GRACE-D ACT1A data provided by SDS. For the second one, during the similar processing and before filtering, thruster events are removed with a margin of 1 s and the corresponding gaps are filled with linear interpolation. The difference between these two data gives thruster firing responses with 1 s sampling. These data can then be combined with the other components, including simulated data, drag model corrections, and residual signal, to create the final TUG transplant product.

Table 6.1.: GRACE-C and GRACE-D thruster response model.

Thruster type	**Direction**	**Value** (nm/s^2)	
		GRACE-C	GRACE-D
Positive Roll			
	SRF x	1.50×10^{-8}	-3.00×10^{-8}
	SRF y	-2.50×10^{-6}	-3.70×10^{-6}
	SRF z	6.00×10^{-7}	6.00×10^{-7}
Negative Roll			
	SRF x	-2.00×10^{-8}	-4.00×10^{-8}
	SRF y	-2.30×10^{-6}	-3.90×10^{-6}
	SRF z	5.50×10^{-7}	6.80×10^{-7}
Positive Pitch			
	SRF x	0.00	5.5×10^{-8}
	SRF y	7.60×10^{-8}	3.33×10^{-8}
	SRF z	-2.30×10^{-6}	-3.50×10^{-6}
Negative Pitch			
	SRF x	-1.09×10^{-7}	-1.19×10^{-7}
	SRF y	-3.75×10^{-8}	0.00
	SRF z	1.55×10^{-6}	3.5×10^{-6}
Positive Yaw			
	SRF x	-0.70×10^{-8}	1.14×10^{-7}
	SRF y	2.00×10^{-6}	4.0×10^{-6}
	SRF z	5.71×10^{-7}	6.0×10^{-7}
Negative Yaw			
	SRF x	-2.20×10^{-8}	1.23×10^{-7}
	SRF y	3.00×10^{-6}	-3.8×10^{-6}
	SRF z	5.30×10^{-7}	5.7×10^{-7}

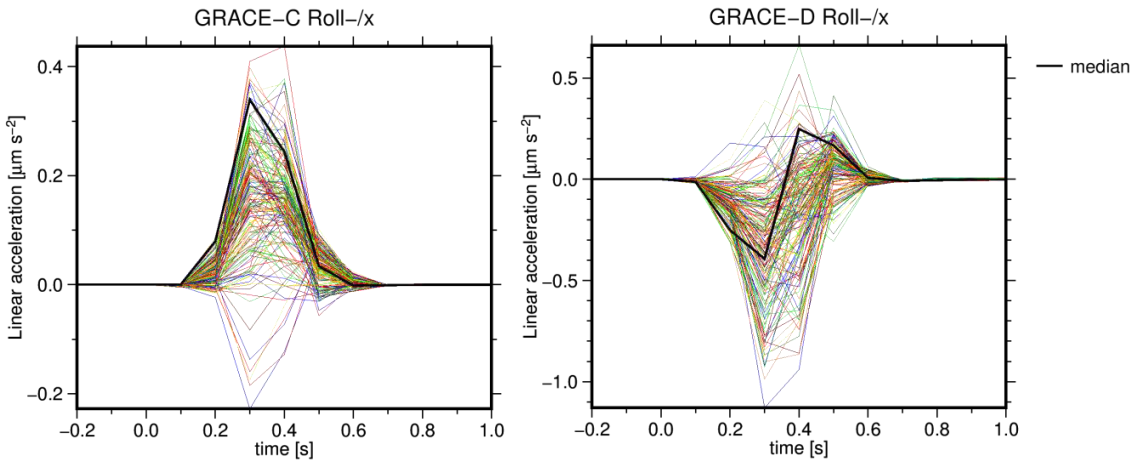

Figure 6.7.: Ensemble of impulse responses associated with negative roll thruster activities in GRACE-C (left) and GRACE-D (right) accelerometer data from June 2018. Both accelerometers show inconsistent thruster responses.

6.5. Alternative ACT products

In this section, the difference between TUG and official SDS ACT1B datasets in time and frequency domain are discussed.

Figure 6.8 compares the two products in terms of their time-series and root PSD of their differences on an arbitrary day, under indirect sunlight condition ($\beta' = 65.9°$). On such orbital configuration, TUG data shows general agreement with the official data in time domain. Therefore, under this orbital condition, TUG ACT1B, obtained with an independent approach, validates the SDS data. Comparison in frequency domain reveals the main differences between the two datasets on each axis at the multiples of orbital frequency or cycle-per-revolution (cpr) frequency. Figure 6.9 shows the same comparison, this time for an arbitrary day, under direct sunlight condition ($\beta' = 1.3°$). Here, the difference between the two products in frequencies below 3 mHz are increases. Specifically in radial and along-track directions, there are major peaks visible at 1-3 cpr frequency. For frequencies over 3 mHz, both datasets are in good agreement as in this frequency range thruster responses are dominant and TUG uses the same model as SDS to generate thruster spikes.

The extent of the differences between the SDS and TUG data is dependent on orbit configuration w.r.t the Sun, i.e. β' angle, as seen in Figure 6.10. When satellites are directly illuminated by the Sun, i.e. $\beta' \sim 0°$, the two data products show differences up to 3 nm/s^2 in radial and along-track directions.

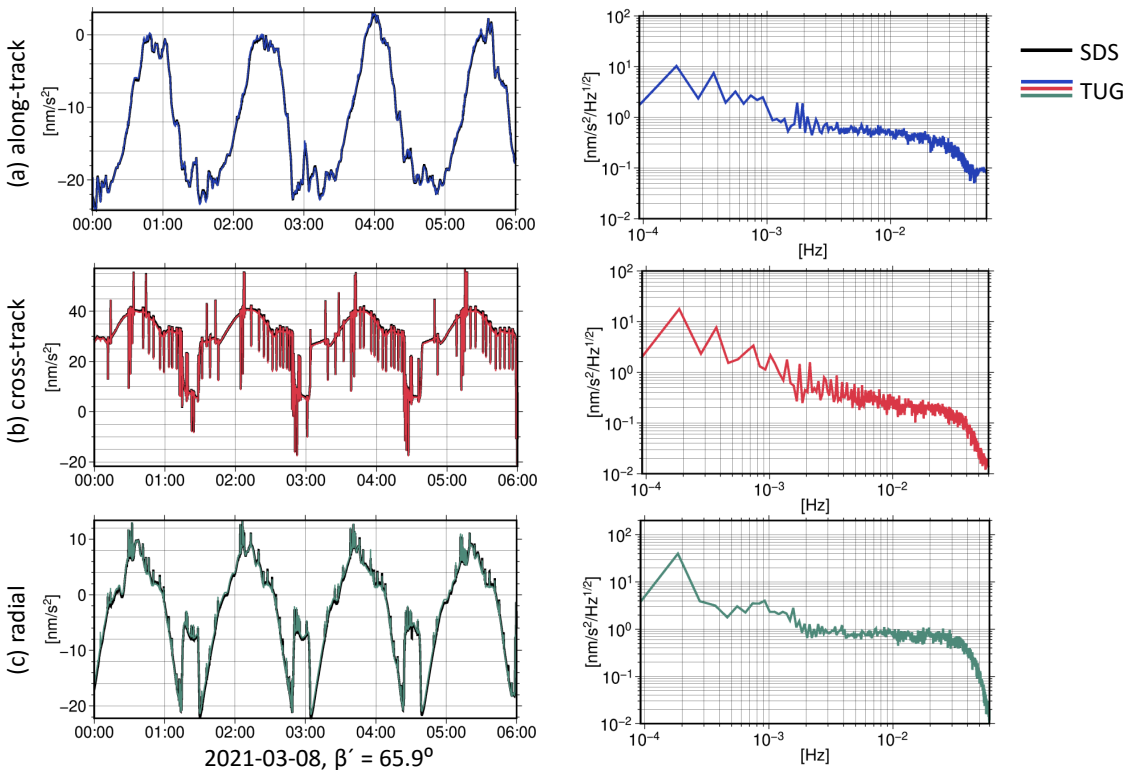

Figure 6.8.: GRACE-D TUG and SDS ACT1B on 2021-03-08 ($\beta' = 65.9°$). The panels on the left compare the two datasets in time domain in (a) along-track, (b) cross-track, and (c) radial directions. The panels on the right reveals the difference between the two datasets in frequency domain.

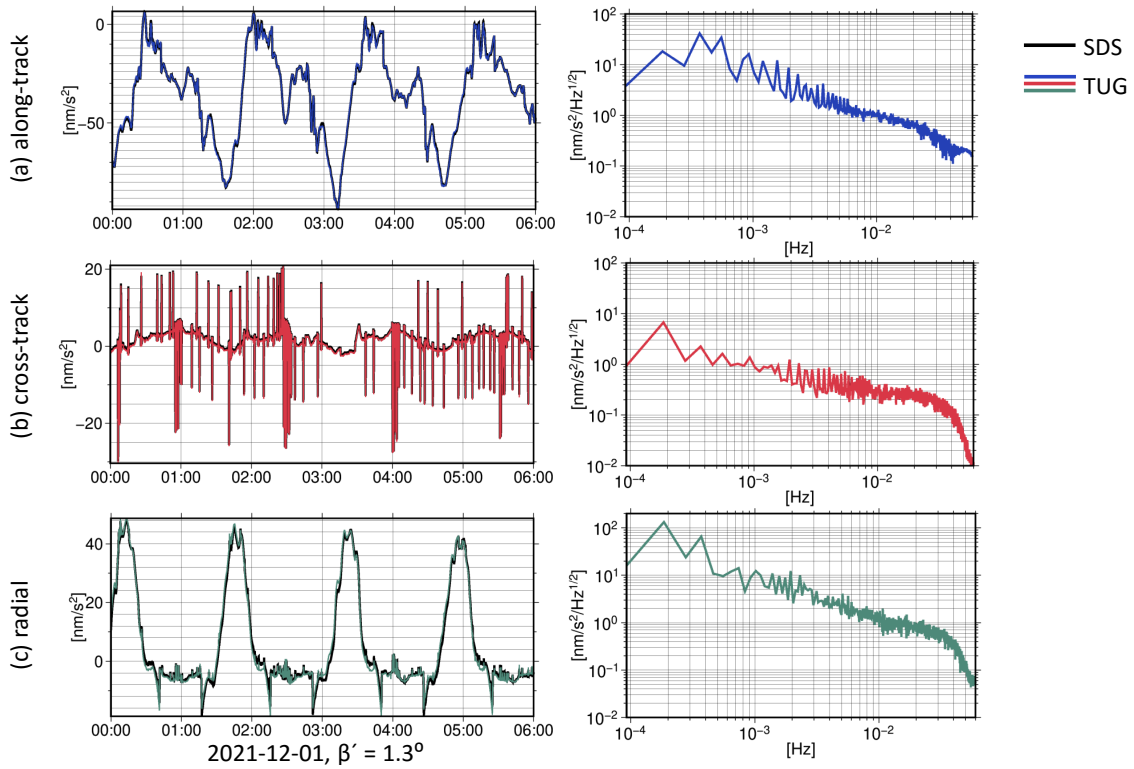

Figure 6.9.: GRACE-D TUG and SDS ACT1B on 2021-12-01 ($\beta' = 1.3°$). The panels on the left compare the two datasets in time domain in (a) along-track, (b) cross-track, and (c) radial directions. The panels on the right reveals the difference between the two datasets in frequency domain.

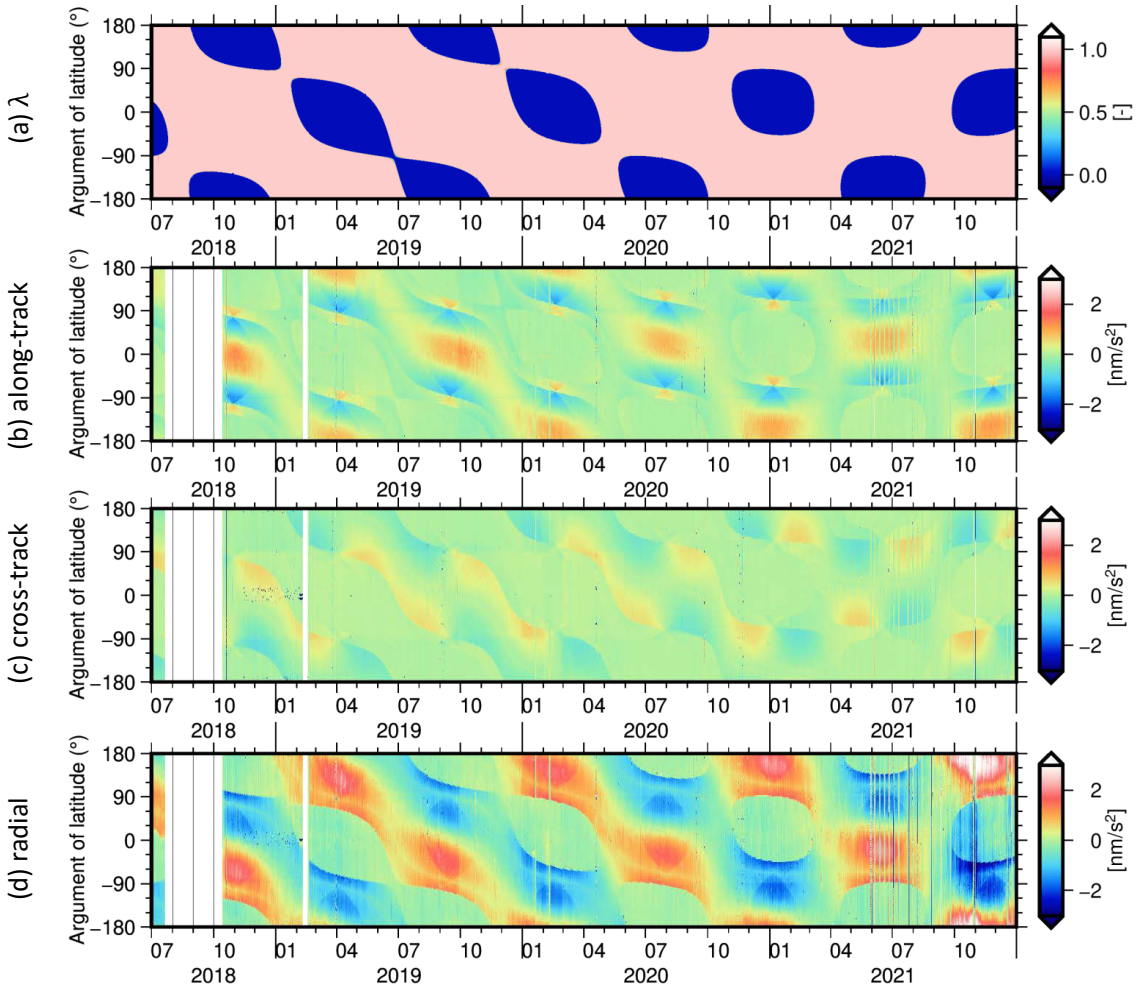

Figure 6.10.: Shadow factor λ (a) and differences between SDS and TUG ACT1B data in (b) along-track, (c) cross-track, and (d) radial directions, plotted w.r.t GRACE-C argument of latitude.

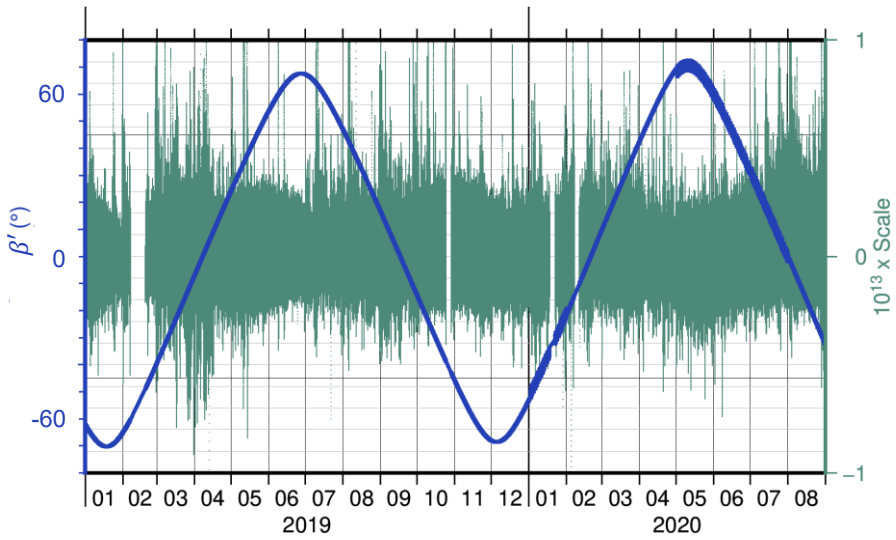

Figure 6.11.: Drag model scale factor compared with β' angle variations from January 2019 to August 2020.

6.5.1. Drag model scale

The proposed recovery process estimates drag model corrections in terms of scale factors, as described in Section 6.4.3. The timeseries of the estimated scale is illustrated in Figure 6.11. This figure indicates that the scale variations is affected by β' angle cycle. This dependency represents the large uncertainty in atmospheric density during periods of direct sunlight, with $|\beta'| < 30°$. At the same time, temperature fluctuations in atmosphere also affects the gas molecular behavior and, as a result, the drag coefficient. The variations in the drag coefficient also influence the calculated scale factors, as shown in Figure 6.12.

The estimated scale factors are also affected by high-frequency perturbations of the atmospheric density during geomagnetic storms, within a range of a few days or hours. To detect and quantify the severity of a geomagnetic storm, one needs to obtain information about the level of geomagnetic activity. While the geomagnetic activity is a measurement of the state of the Earth's magnetic field, it is mainly triggered by solar events.

As the beginning of GRACE-FO mission coincided with a period of solar minimum (2018-2020), such perturbations are rarely observed in the scale factors during this time. During this time, the most intense geomagnetic storm occurred on August 26, 2018, which had an impact on GRACE-C accelerometer measurements, according to Krauss et al. (2020). This period is not included in the scale time-series due to the data gaps in GRACE-D data. Nonetheless, a few minor geomagnetic storms caused atmospheric disruptions in 2019, which also influenced the scale factors. December 2019 is marked as the beginning of the 25th solar cycle. Since then, solar activity has steadily increased

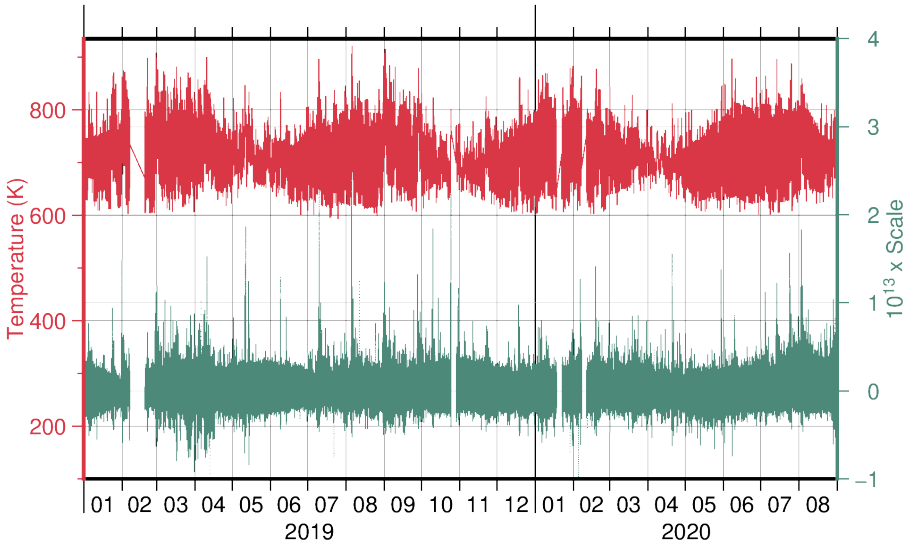

Figure 6.12.: Drag model scale factor compared with thermosphere temperature derived from JB2008 model from January 2019 to August 2020.

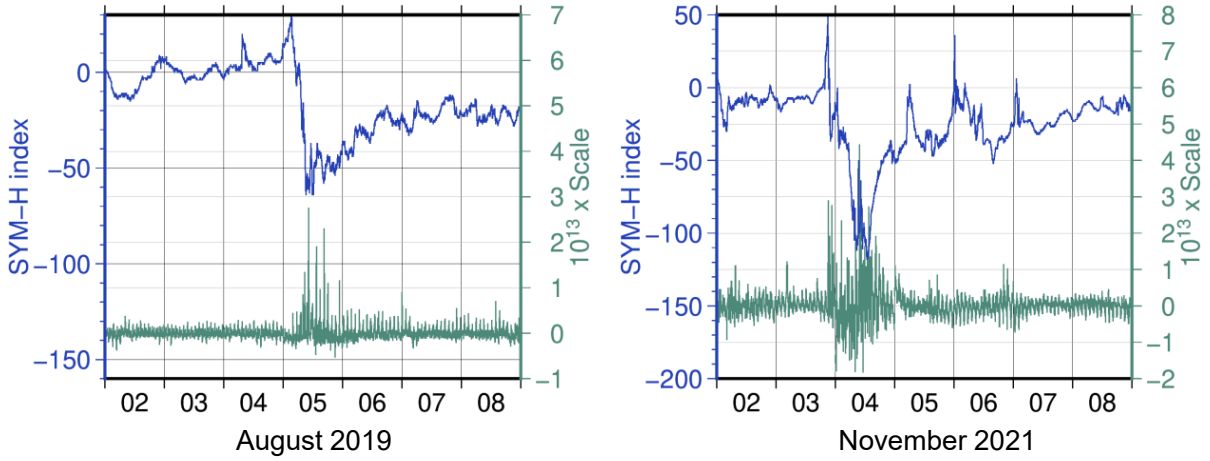

Figure 6.13.: Comparison of the estimated drag scale with the SYM-H index during two geomagnetic events in (a) August 2019 and (b) November 2021.

and more perturbation in atmospheric density and, therefore, in the scale factors can be observed.

There are several defined indices that state the level of geomagnetic activity. Among these indices, SYM-H index (Iyemori et al., 2010) is an adequate metric to study the impact of a geomagnetic storm on thermosphere. This index represents the severity of geomagnetic disturbances at mid-latitudes with a temporal resolution of 60 second. Figure 6.13 shows the estimated scale's time-series in comparison to the variations in this index for two selected event in August 2019 and November 2021. It can be concluded that the negative peaks in the SYM-H and variations in scale factor time-series have a clear link. This shows that the estimated scales can have a potential application in space weather and atmospheric research. In addition to solar event detection, the estimated scales may be used to analyze and improve current thermospheric models, along with observations from other satellite missions (e.g. Siemes et al., 2016).

6.6. Impact on gravity field

This section studies the impact of the alternative TUG ACT1B product on the monthly gravity field solutions using ITSG-Grace2018 scheme (Kvas et al., 2019). This analysis is based on recovered monthly solutions from July 2018 to December 2021. To focus on the accelerometer data, two gravity field scenarios are considered: (1) ITSG-Grace2018p, which stands for preliminary monthly solutions based on SDS ACT1B, serving as a benchmark, and (2) final ITSG-Grace2018 solutions based on TUG ACT1B.

6.6.1. Degree amplitudes

Figure 6.14 shows the degree amplitudes for three consecutive months, from January to March 2020, within one β' cycle. The corresponding degree amplitudes are plotted w.r.t the static gravity field GOCO06s. For February and March 2020, using TUG ACT1B visibly reduces noise level for degrees over 40. This confirms that the differences observed in both ACT products during these months are, in fact, due to the drawbacks of the SDS transplant approach. On the other hand, for January 2020, and generally most of the months with $|\beta'| > 30$, both products deliver approximately similar solutions.

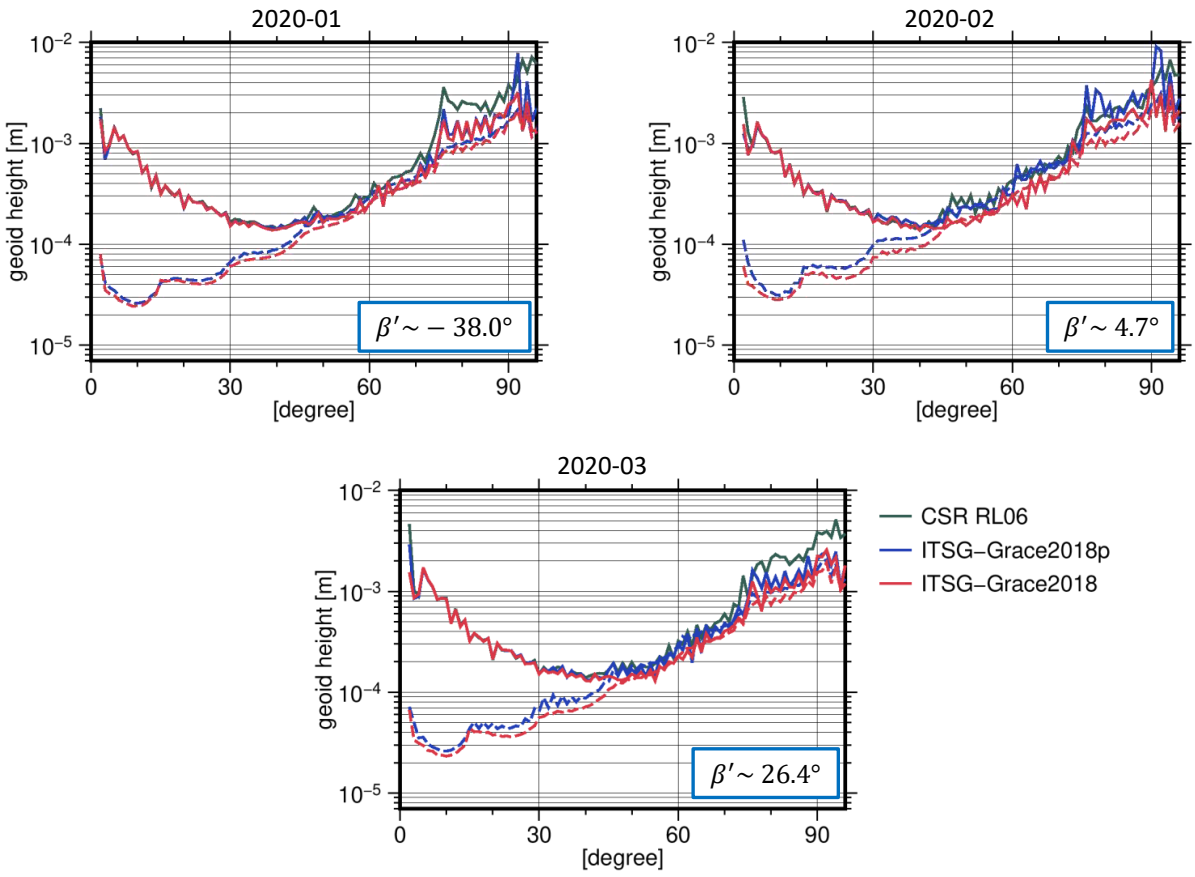

Figure 6.14.: Degree amplitudes of the CSR RL06, ITSG-Grace2018p, and ITSG-Grace2018 solutions for January, February, and March 2020 w.r.t the GOCO06s model.

6.6.2. Spatial domain

Figure 6.15 exhibits the impact of TUG ACT1B in the spatial domain for the selected months. For both solutions, EWH grids are generated w.r.t the GOCO06s model. Additionally, a Gaussian filter with 300 km radius is applied to the EWH grids. For the final ITSG-Grace2018 solution, the global RMS values are reduced up to 4 percent w.r.t the preliminary solution. In addition to a significant reduction of the north-south strips in all three months, the impact on low degree zonals, mainly C_{20} and C_{30}, is visible in February and March solutions.

Figure 6.16 displays ocean RMS of CSR RL06, ITSG-Grace2018p, and ITSG-Grace2018 solutions from July 2018 to December 2021. Except for October 2018 and February 2019, when only less than 10 and 14 days data is available respectively, ITSG-Grace2018 solutions generally show less noise, compared to CSR RL06. To quantify the impact of the ACT product, Figure 6.17 shows the differences between corresponding time-series of ocean RMS for the two set of solutions in percentage, with positive values indicating

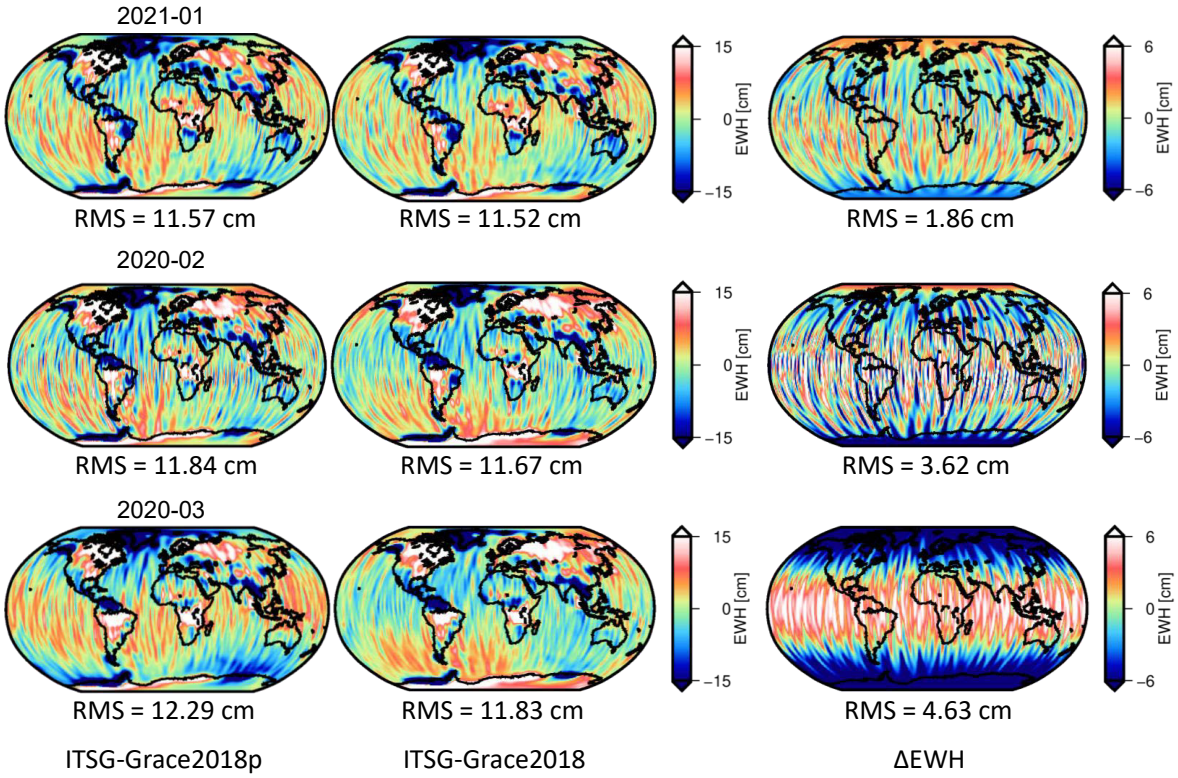

Figure 6.15.: EWH of the ITSG-Grace2018p, ITSG-Grace2018, and the difference between the solutions for January, February, and March 2020 w.r.t the GOCO06s model. A 300 km Gaussian filter is also applied.

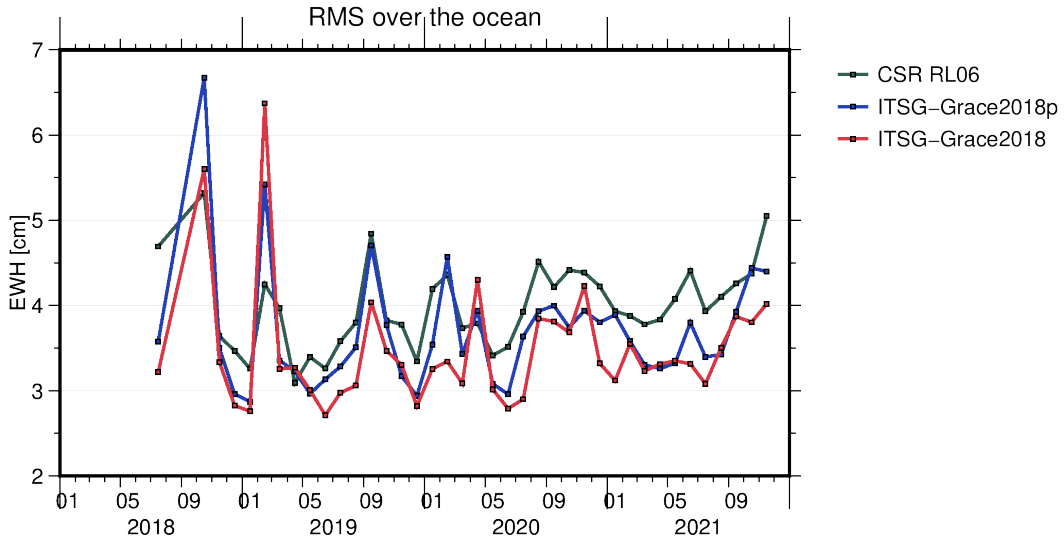

Figure 6.16.: Ocean RMS time-series in equivalent water height (EWH) for the CSR RL06, ITSG-Grace2018p, and final ITSG-Grace2018 solutions. Before computing the RMS values, the annual cycle and trend of GOCO06s were reduced and a 300-km Gaussian filter was applied.

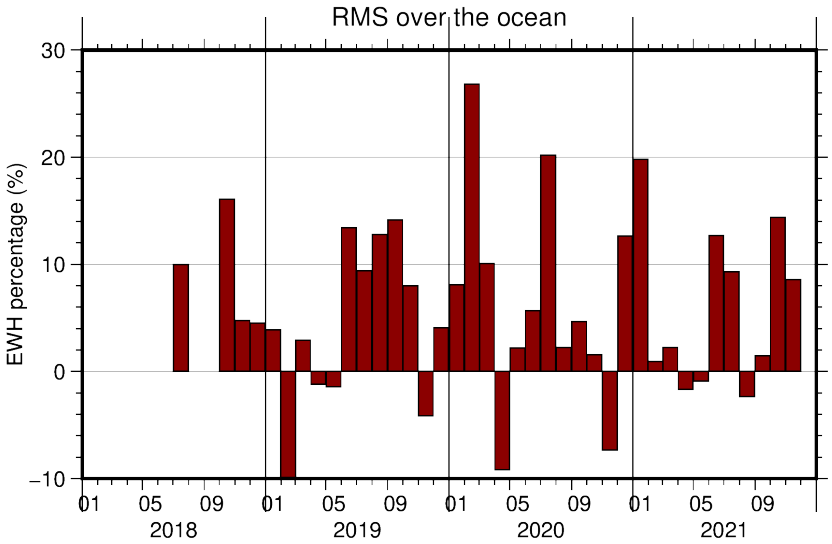

Figure 6.17.: Percentage of differences between temporal RMS of the ITSG-Grace2018p and final ITSG-Grace2018 solutions. The positive values indicates reduction of RMS values in the final solution.

RMS decrease in the final solutions. ITSG-Grace2018 reaches up to 26 percent noise reduction by using the alternative ACT product. With excluding February 2019 from the time-series, one can also see that for November 2019, April 2020, and November 2020 using TUG ACT1B data degrades the solutions 4-8 percent. However, for rest of the months, the obtained results strongly support the use of the alternative transplant approach.

6.6.3. Post-fit range rate residuals

Figure 6.18 shows the root power spectral densities of the post-fit range rate residuals from ITSG-Grace2018p and ITSG-Grace2018 solutions. It can be concluded that using TUG ACT1B attenuates the strong 2 cpr and 3 cpr signals that existed in the preliminary scenario. This clearly indicates the general improvement of gravity field solutions, as well as better estimation of low degree coefficients, especially C_{20} and C_{30}.

6.6.4. Low-degree zonal coefficients

In the following, the impact of the use alternative ACT product on the C_{20} and C_{30} coefficients are studied. According to Kim (2000), non-gravitational accelerations exhibit strong orbital frequencies, i.e. 1-3 cpr frequencies, and these frequencies have the similar characteristics to the corresponding frequency of the resonant gravity field coefficient. As a result, accelerometer errors directly affect low degree zonal

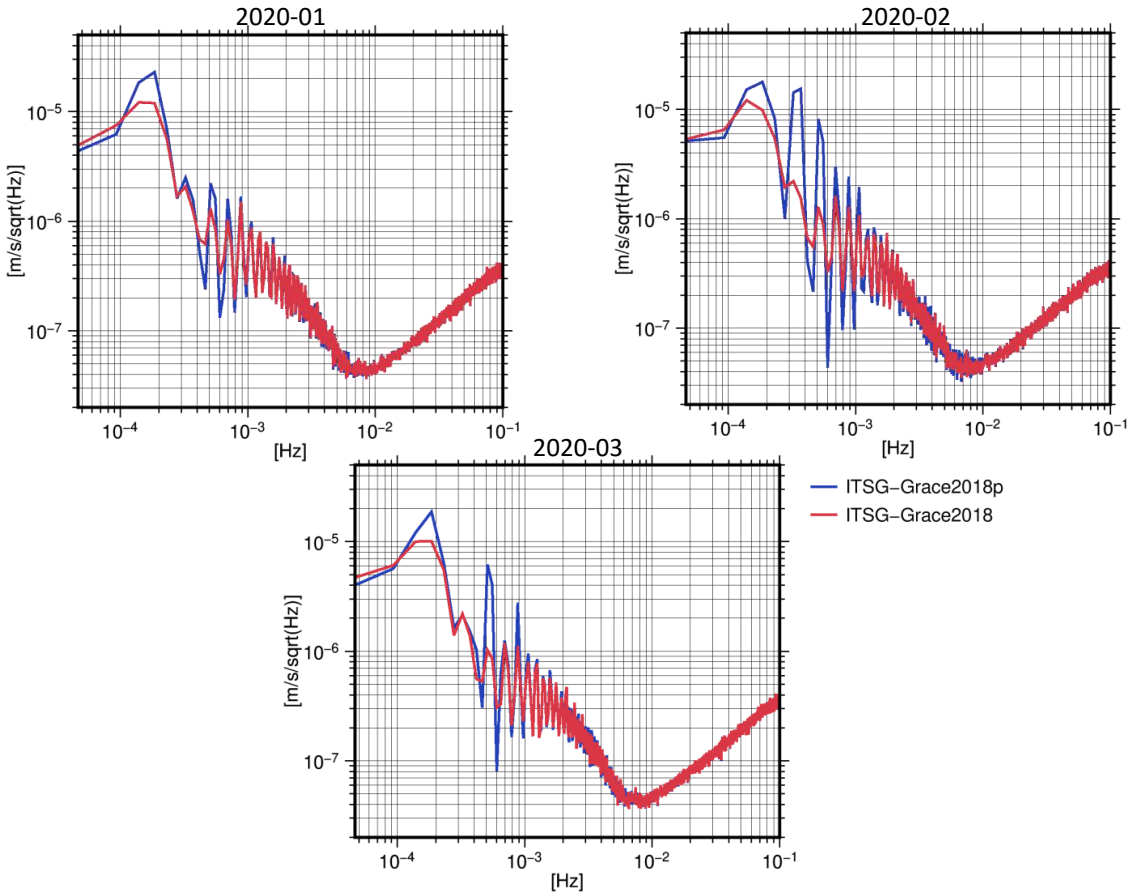

Figure 6.18.: $\sqrt{PSD}$ of the post-fit range rate residuals from the ITSG-Grace2018p and ITSG-Grace2018 solutions for January, February, March 2020.

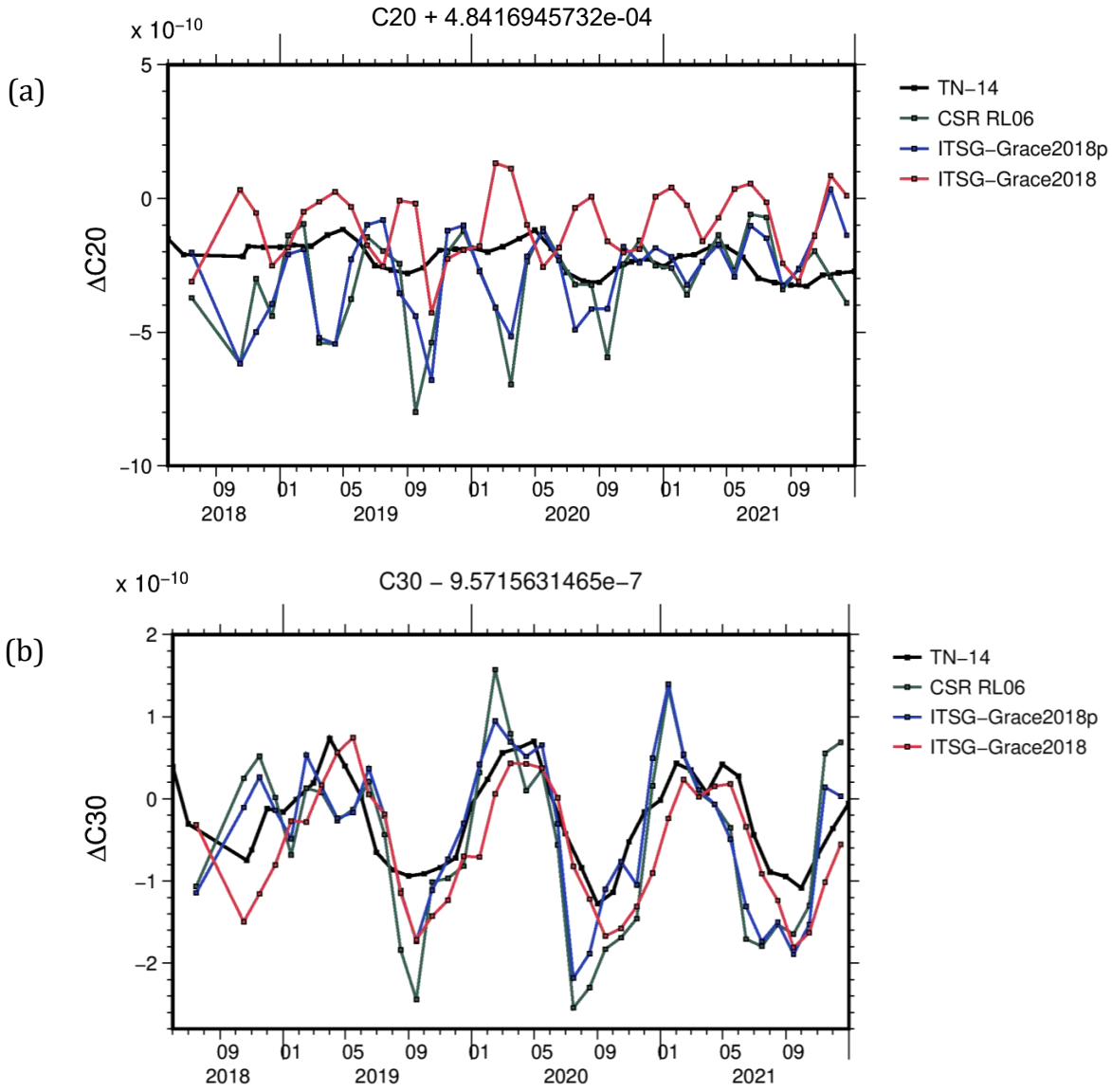

Figure 6.19.: (a) C_{20} and (b) C_{30} time-series from CSR RL06, ITSG-Grace2018p, and ITSG-Grace2018 solutions. The GRACE-FO estimates are compared with the recommended SLR derived values in Technical Note-14.

coefficients during gravity field recovery. Figure 6.19 compares the monthly estimates of these coefficients, derived from the two scenarios, and SLR-derived values. In case of C_{20} coefficients, it can be seen that the preliminary offset in the estimates from ITSG-Grace2018 solutions has reduced w.r.t the TN-14 values. Nevertheless, the C_{20} coefficients, similar to their estimates from GRACE observations, still have a strong 161-day signal and should be replaced with C_{20} estimates of SLR data.

The C_{30} time-series is also shown in 6.19b. This figure shows a high correlation between ITSG-Grace2018 estimates and SLR estimates of C_{30} coefficients. This validates the hypothesis that the estimates of the C_{30} coefficients are greatly improved by suppressing 2 cpr and 3 cpr signals in the alternative transplant data. As expected, the improvement is most noticeable during the low β' months.

6.7. Summary

The benefits of adding non-gravitational force models and applying drag model adjustments inside GRACE-D ACC recovery are demonstrated in this chapter. Higher degrees of the recovered monthly gravity field solutions, as well as low zonal degrees 2 and 3, are better estimated using the alternative ACT product.

It was demonstrated that non-gravitational forces, specifically the corrected drag model, may recover a portion of the acceleration signal that is lost in the direct transplant technique in both radial and along-track directions. The amount of this missing signal is dependent on the β' angle and peaks during direct Sun exposure. This signal is approximately zero when satellites are travelling through the Earth's shadow.

In addition, it was shown that the drag model scale adjustment primarily reflects physical characterizations of changing thermosphere density. This covers both long-term variations caused by direct sunlight and short-term variations caused by geomagnetic storms. As a result, the alternative approach not only improves the quality of the gravity field, but also provides valuable information about satellite interactions with their surroundings. It is worth noting that, in addition to the effects stated, the estimations are likely to include other factors, such as differences in radiation pressure models, which are not properly modeled.

Conclusion and Outlook

7

This dissertation contributes to the ongoing efforts to improve the accuracy of monthly gravity field solutions derived from GRACE and GRACE-FO. The presented results, advances the state-of-the-art processing chain of ITSG-Grace2018, which has been computed at TUG. The proposed KBR parametrization presented in Chapter 5 and the alternative accelerometer data product described in Chapter 6 considerably improves the gravity field solutions.

Chapter 4 showed that the post-fit range rate residuals have a non-stationary behaviour, i.e. their frequency components are dynamic and vary over time. It is therefore convenient to analyse the noise in the framework of non-stationary processes and deploy wavelets for the analysis of the non-stationary time series. The Discrete Wavelet Transform (DWT) was applied for a better decomposition of the post-fit residuals which in particular improved understanding of the superimposed signals in the mHz frequency range. This frequency range is of special importance as, on one hand, it contains valuable gravity field signals and on the other hand, it receives the highest weight during the adjustment process. Therefore, even a minor error contributor in this range can bring observable impact to the solution.

The efforts in mitigating KBR systematic errors, described in Chapter 5, has proved this importance. Although the parametrization cannot fully resolve these errors over the complete GRACE period, it can certainly reduce their impact on the higher degrees (> 60) of gravity fields for a majority of months.

Chapter 6 discussed the role of synthesized accelerometer data in GRACE-FO gravity field recovery. First and foremost, it showed that the accuracy of the accelerometer measurements is critical for the gravity field recovery, and how any large inaccuracies would degrade the quality of recovered solutions. This followed by the hypothesis regarding the shortcoming of current official ACT1B products RL04, in recovering the full non-gravitational signal. Once the force models were implemented in the recovery processing, a significant improvement was observed in the accuracy of the gravity fields.

In summary, this research highlights the efforts in detecting and resolving the remaining instrumental errors in GRACE/GRACE-FO processing. The presented results proved the benefits of public release of GRACE-FO Level-1A data and shows the same

potential for GRACE data. The independent studies on alternative Level-1B products lead to alter the understanding of GRACE sensors and their required improvements for future gravity field missions.

7.1. Outlook

Currently, the main limiting factors in the operational GRACE-FO solutions are errors in the accelerometer transplant approach and modeling high-frequency temporal gravity variations (Flechtner et al., 2016). The Level-2 processing can potentially benefit from an updated AOD1B product which models the high-frequency temporal gravity variations. There have already been efforts toward improving these products with the upcoming RL07 (Shihora & Dobslaw, 2020).

Extending the presented results in this research may also further improve the temporal gravity field models of GRACE-FO or any future GRACE-type mission. In the following, the potential improvements and applications of the applied methodologies are discussed.

7.1.1. GRACE-FO KBR and LRI systematic errors

The presence of the introduced KBR systematic errors and the possibility of their elimination in Level-1A data can be further investigated in GRACE-FO processing. This can be accomplished by exploiting the unique instrumentation of GRACE-FO, i.e. with the independent ranging measurements of the LRI system. This additional measurement provides supplementary observations, which enable a cross-instrument validation with the KBR system.

The applied GRACE residual analysis approach can easily be adapted to the GRACE-FO processing. In addition to KBR-based solutions, residual analysis may reveal unknown systematic effects in LRI-based gravity fields. The method is also potentially helpful for further investigation of the already-studied LRI systematic errors such as phase jumps and scale factor (Misfeldt, 2019).

7.1.2. GRACE-FO improved transplant data

The transplant procedure can be further improved by improving the non-gravitational force models as well as the thruster spike models. As demonstrated by GRACE mission (Bandikova et al., 2019), adding more realistic thruster responses in transplant data significantly reduces noise levels in degrees over 15.

To improve the thruster responses, one can set empirical parameters to estimate these models together with the gravity parameters. On the other hand, it is also possible to obtain precise spike models, e.g. by incorporating the pressure readings from thruster regulators. This is an ongoing study by Harvey et al. (2022) for the upcoming release of data. Another remaining issue is that the alternative transplant data is based on bias-corrected GRACE-C observations, therefore, contain unknown GRACE-C specific ACC scales. To improve gravity field, the accelerometer scale and bias must be modeled and co-estimated to minimize degradation of the recovered solutions.

As also suggested by Bandikova et al. (2019), transplant data cannot reach the accuracy level of real measurements. Therefore, efforts need to be continued toward understanding and using the original GRACE-D accelerometer data.

Appendices

A. Reference frames

The GRACE data are processed and provided in several reference frames, depending on the data level and the corresponding instrument. The definitions of the most relevant reference frames utilized in the framework of this dissertation are summarized in this section. For more details of all GRACE reference frames, the reader is referred to Case et al. (2010) and Bettadpur (2012). Figure A.1 shows the alignment of the main GRACE body-fix frames, utilized in this dissertation.

A.1. Science Reference Frame

This reference frame specifies all Level-1B data products. The origin of the science reference frame (SRF) is defined to be located at the satellite center of mass. The axes are aligned with the measurement axes of the accelerometer (cf. Appendix A.2), with x-axis being parallel to the roll axis of the satellite and the z-axis being parallel to the nadir direction. The y-axis completes a right-handed triad.

A.2. Accelerometer Frame

The Accelerometer Frame (AF) is realized by reference marks on the surface of the ACC, with its origin at the center of mass of the proof mass. The accelerometer is positioned in such a way that:

$$\begin{aligned} \boldsymbol{x}_{AF} &= \boldsymbol{y}_{SRF}, \\ \boldsymbol{y}_{AF} &= \boldsymbol{z}_{SRF}, \\ \boldsymbol{z}_{AF} &= \boldsymbol{x}_{SRF}. \end{aligned} \tag{A.1}$$

A.3. Star Camera Frame

GRACE satellites are equipped with two heads of start camera. For each of these heads, the respective star camera frame (SCF) is defined. The origin of each frame is located at the center of camera field of view (FoV). The x-axes are aligned with the x-axis of the SRF and the z-axis of each SCF is towards the focal point of the star camera head.

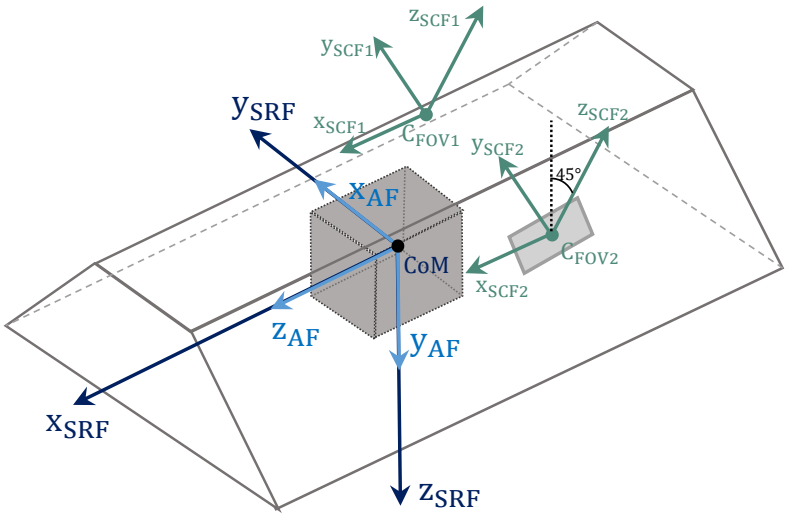

Figure A.1.: The alignment of GRACE body-fix reference frames including accelerometer frame (AF), science reference frame (SRF), and star camera frame (SCF).

A.4. Inertial Reference Frame

The International Celestial Reference Frame (ICRF), as realized by the J2000.0 equatorial coordinates, is referred to as the inertial reference frame. The ICRF origin defined at the Earth's Center of Mass. The x-axis points to the vernal equinox and the z-axis corresponds to the Earth's rotation axis and points towards the North Pole. The y-axis completes a right-handed triad. For more detailed definition, the reader is referred to Petit and Luzum (2010).

A.5. Terrestrial Reference Frame

The earth-fixed Terrestrial Reference Frame (TRF) is the International Terrestrial Reference Frame (ITRF), which is defined by the IERS (Petit & Luzum, 2010). This reference frame is realized by a network of observation: Very Long Baseline Interferometry (VLBI), Satellite Laser Ranging (SLR), GNSS, and Doppler Orbitography and Radio Positioning Integrated by Satellite (DORIS).

B. Orbit geometry

B.1. Orbital elements

The classical orbital elements, also known as Keplerian orbital elements, are used to quantify the main characteristics of an orbit. The first five elements define the orbit, whereas the sixth element determines the position of satellite in the orbit. The six orbital elements are as follows:

Semi-major axis (a) This parameter defines the size of an elliptical orbit. The long axis of the ellipse is called the major axis, and the shorter one is the minor axis. The semi-major axis, or half of the major axis, is used to define the size of the ellipse.

Eccentricity (e) This dimensionless parameter determines the amount by which an elliptical orbit deviates from a perfect circle, with a value of 0 defining circular orbit and values between 0 and 1 forming an elliptic orbit.

Longitude of ascending node (Ω) As shown in Figure B.1, the ascending node is where a satellite's orbit crosses the Earth's equator when traveling from south to north. The longitude of the ascending node is defined with reference to the fundamental plane, i.e. Earth's equatorial plane, and the principal direction, i.e. the vernal equinox direction.

Inclination (i) Inclination angle is the vertical tilt of the ellipse w.r.t the fundamental plane, measured at the ascending node. This angle is measured perpendicular to the line of nodes, i.e. the line of intersection between orbital plane and fundamental plane.

Argument of perigee (ω) This angle defines the location of orbit's perigee w.r.t the Earth's surface. This is the angle, formed in the orbital plane, from the ascending node to perigee.

True anomaly (ν) This angle defines the position of a satellite along a orbit. It is the angle between the direction of perigee and the current position of the satellite, in the orbital plane.

Note that ν is not defined for circular orbit since there is no perigee in such orbit. In this case, the argument of latitude, u, is used which indicates the location of the satellite in the orbit, measured between the ascending node vector and the current position, as shown in Figure B.1. For an elliptical orbit, this gives,

$$u = \omega + \nu. \tag{B.1}$$

According to Montenbruck and Gill, 2000, for the circular orbits eq. (B.1) can be written as:

$$u = \arctan\left(\frac{z/\sin i}{x\cos\Omega + y\sin\Omega}\right), \tag{B.2}$$

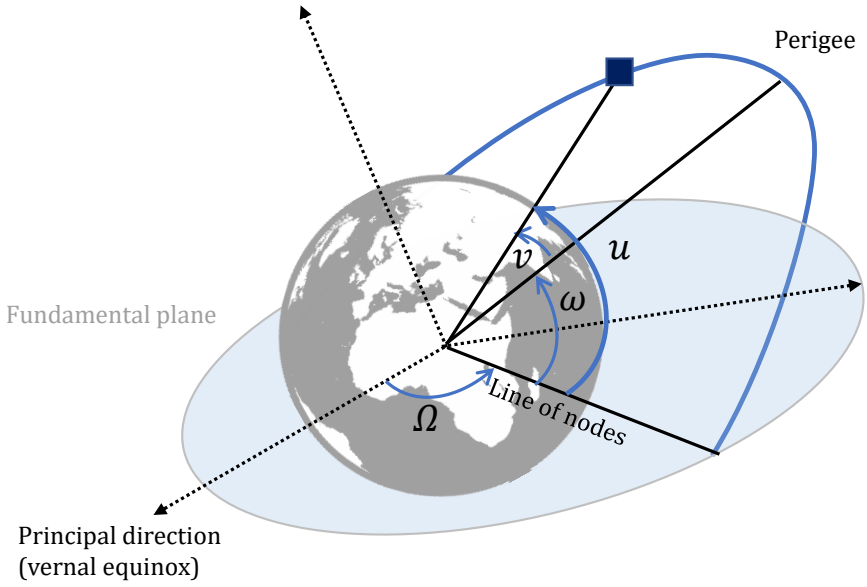

Figure B.1.: Definition of orbital elements including longitude of ascending node Ω, argument of perigee ω, true anomaly v, and argument of latitude u.

where x, y, and z are the coordinates of the satellite's position.

B.2. Beta prime angle

The β' angle is a measurement that is widely used to describe the orbital configuration relative to the Sun. It is a measure of how much time a satellite spends in direct sunshine, absorbing solar energy. The β' angle is calculated based on the satellite's orbital plane normal vector $\hat{\mathbf{n}}$ and the direction to the Sun $\hat{\mathbf{s}}$:

$$\beta' = \arccos\left(\frac{\hat{\mathbf{n}} \cdot \hat{\mathbf{s}}}{|\hat{\mathbf{n}}| \cdot |\hat{\mathbf{s}}|}\right) - 90^\circ, \tag{B.3}$$

β' angle is an important factor for operating a satellite because it determines how much solar energy the spacecraft receives. Figure B.2 schematically shows how the β' angle changes over time. In case of GRACE mission, approximately every five months the direction to the Sun is in the orbital plane, i.e. $\beta' = 0$. This is because the orbit has a precession of $\sim 1.1^\circ$ per day, or equivalently a 322 day period relative to the Sun. During this time, the satellites are in Earth's shadow up to 40 percent of their orbital period, and are exposed to direct sunlight during the rest. On the other hand, when $|\beta'| > 70$, they are exposed to sunlight all the time.

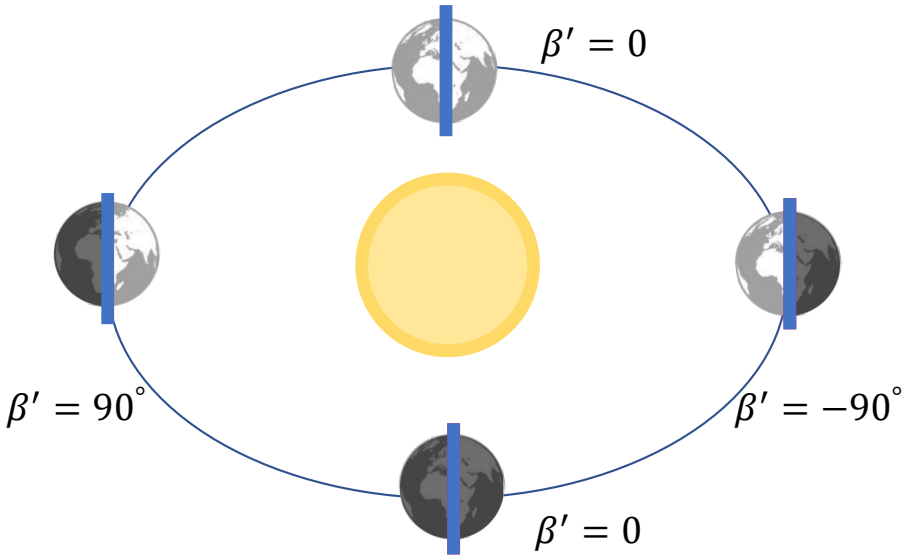

Figure B.2.: β' angle variations over time: $\beta' = 0$ indicates the periods when the Sun directly illuminates the satellites for approximately half of the orbit. When $|\beta'| = 90$, the Sun indirectly illuminates the satellites all the time.

Bibliography

Abich, K., Abramovici, A., Amparan, B., Baatzsch, A., Okihiro, B. B., Barr, D. C., Bize, M. P., Bogan, C., Braxmaier, C., Burke, M. J., Clark, K. C., Dahl, C., Dahl, K., Danzmann, K., Davis, M. A., de Vine, G., Dickson, J. A., Dubovitsky, S., Eckardt, A., … Zimmermann, M. (2019). In-orbit performance of the grace follow-on laser ranging interferometer. *Phys. Rev. Lett.*, *123*, 031101. https://doi.org/10.1103/PhysRevLett.123.031101 (cit. on p. 6)

Arfken, G. B., Weber, H. J., & Harris, F. E. (2013). *Mathematical methods for physicists*. Elsevier. https://doi.org/10.1016/c2009-0-30629-7. (Cit. on p. 35)

Bandikova, T., & Flury, J. (2014). Improvement of the GRACE star camera data based on the revision of the combination method. *Adv. Space Res.*, *54*(9), 1818–1827. https://doi.org/10.1016/j.asr.2014.07.004 (cit. on p. 44)

Bandikova, T., Flury, J., & Ko, U.-D. (2012). Characteristics and accuracies of the GRACE inter-satellite pointing. *Adv. Space Res.*, *50*(1), 123–135. https://doi.org/10.1016/j.asr.2012.03.011 (cit. on p. 54)

Bandikova, T., McCullough, C., Kruizinga, G. L., Save, H., & Christophe, B. (2019). GRACE accelerometer data transplant. *Advances in Space Research*, *64*(3), 623–644. https://doi.org/10.1016/j.asr.2019.05.021 (cit. on pp. 7, 82, 91, 108, 109)

Behzadpour, S., Mayer-Gürr, T., Flury, J., Klinger, B., & Goswami, S. (2019). Multiresolution wavelet analysis applied to GRACE range-rate residuals. *Geoscientific Instrumentation, Methods and Data Systems*, *8*(2), 197–207. https://doi.org/10.5194/gi-8-197-2019 (cit. on pp. 43, 50, 60)

Behzadpour, S., Mayer-Gürr, T., & Krauss, S. (2021). GRACE follow-on accelerometer data recovery. *Journal of Geophysical Research: Solid Earth*, *126*(5). https://doi.org/10.1029/2020jb021297 (cit. on p. 81)

Bettadpur, S. (2012). *Gravity recovery and climate experiment: Product specification document*. (tech. rep.). Center for Space Research, The University of Texas at Austin. (Cit. on pp. 22, 23, 113).

Björck, Å. (1996). *Numerical methods for least squares problems*. Society for Industrial; Applied Mathematics. https://doi.org/10.1137/1.9781611971484. (Cit. on p. 32)

Bonin, J. A., Bettadpur, S., & Tapley, B. D. (2012). High-frequency signal and noise estimates of CSR GRACE RL04. *Journal of Geodesy*, *86*(12), 1165–1177. https://doi.org/10.1007/s00190-012-0572-5 (cit. on pp. 44, 68)

Bowman, B., Tobiska, W. K., Marcos, F., Huang, C., Lin, C., & Burke, W. (2008). A new empirical thermospheric density model JB2008 using new solar and geomagnetic indices. *AIAA/AAS Astrodynamics Specialist Conference and Exhibit*. https://doi.org/10.2514/6.2008-6438 (cit. on p. 24)

Bruinsma, S. (2015). The DTM-2013 thermosphere model. *Journal of Space Weather and Space Climate*, *5*, A1. https://doi.org/10.1051/swsc/2015001 (cit. on p. 24)

Busch, P., Heinonen, T., & Lahti, P. (2007). Heisenberg's uncertainty principle. *Physics Reports*, *452*(6), 155–176. https://doi.org/10.1016/j.physrep.2007.05.006 (cit. on p. 38)

Carrere, L., Lyard, F., Cancet, M., & Guillot, A. (2015). FES 2014, a new tidal model on the global ocean with enhanced accuracy in shallow seas and in the Arctic region. *EGU General Assembly Conference Abstracts*, *17*, Article 5481, 5481 (cit. on p. 13).

Case, K., Kruizinga, G., & Wu, S.-C. (2010). *GRACE Level-1B Data Product User Handbook* (tech. rep. JPL D-22027). Jet Propulsion Laboratory, Pasadena, California. https://podaac-tools.jpl.nasa.gov/drive/files/allData/grace/docs/Handbook_1B_v1.3.pdf. (Cit. on pp. 5, 9, 21, 29, 113)

Chambers, D. P. (2006). Observing seasonal steric sea level variations with GRACE and satellite altimetry. *Journal of Geophysical Research*, *111*(C3). https://doi.org/10.1029/2005jc002914 (cit. on p. 2)

Chen, J. L., Wilson, C. R., & Tapley, B. D. (2010). The 2009 exceptional amazon flood and interannual terrestrial water storage change observed by GRACE. *Water Resources Research*, *46*(12). https://doi.org/10.1029/2010wr009383 (cit. on p. 2)

Christophe, B., Boulanger, D., Foulon, B., Huynh, P.-A., Lebat, V., Liorzou, F., & Perrot, E. (2015). A new generation of ultra-sensitive electrostatic accelerometers for grace follow-on and towards the next generation gravity missions. *Acta Astronautica*, *117*, 1–7. https://doi.org/10.1016/j.actaastro.2015.06.021 (cit. on p. 7)

Coumou, D., & Rahmstorf, S. (2012). A decade of weather extremes. *Nature Climate Change*, *2*(7), 491–496. https://doi.org/10.1038/nclimate1452 (cit. on p. 1)

Daubechies, I. (1992). *Ten Lectures on Wavelets*. Society for Industrial; Applied Mathematics. https://doi.org/10.1137/1.9781611970104. (Cit. on pp. 40, 46)

de Boor, C. (2001). *A practical guide to splines*. Springer Verlag. (Cit. on p. 35).

Desai, S. D. (2002). Observing the pole tide with satellite altimetry. *Journal of Geophysical Research*, *107*(C11). https://doi.org/10.1029/2001JC001224 (cit. on p. 13)

Dill, R. (2008). Hydrological model LSDM for operational Earth rotation and gravity field variations [Scientific Technical Report STR08/09]. http://publications.iass-potsdam.de/pubman/item/escidoc:8770:3/component/escidoc:18157/0809.pdf. (Cit. on p. 13)

Ditmar, P., da Encarnação, J. T., & Farahani, H. H. (2012). Understanding data noise in gravity field recovery on the basis of inter-satellite ranging measurements

acquired by the satellite gravimetry mission GRACE. *J. Geod.*, *86*(6), 441–465. https://doi.org/10.1007/s00190-011-0531-6 (cit. on pp. 44, 50, 62)

Dobslaw, H., Bergmann-Wolf, I., Dill, R., Poropat, L., Thomas, M., Dahle, C., Esselborn, S., König, R., & Flechtner, F. (2017). A new high-resolution model of non-tidal atmosphere and ocean mass variability for de-aliasing of satellite gravity observations: Aod1b rl06. *Geophysical Journal International*, *211*(1), 263–269. https://doi.org/10.1093/gji/ggx302 (cit. on pp. 13, 20)

Drob, D. P., Emmert, J. T., Meriwether, J. W., Makela, J. J., Doornbos, E., Conde, M., Hernandez, G., Noto, J., Zawdie, K. A., McDonald, S. E., Huba, J. D., & Klenzing, J. H. (2015). An update to the horizontal wind model (HWM): The quiet time thermosphere. *Earth and Space Science*, *2*(7), 301–319. https://doi.org/10.1002/2014ea000089 (cit. on p. 24)

Ellmer, M. (2018). *Contributions to GRACE gravity field recovery: Improvements in dynamic orbit integration, stochastic modelling of the antenna offset correction, and co-estimation of satellite orientations* (Doctoral dissertation). Institute of Geodesy, Graz University of Technology. (Cit. on pp. 14, 44, 56, 57).

Ellmer, M., & Mayer-Gürr, T. (2017). High precision dynamic orbit integration for spaceborne gravimetry in view of GRACE Follow-on. *Advances in Space Research*, *60*(1), 1–13. https://doi.org/https://doi.org/10.1016/j.asr.2017.04.015 (cit. on p. 12)

Emmert, J. T., Drob, D. P., Picone, J. M., Siskind, D. E., Jones, M., Mlynczak, M. G., Bernath, P. F., Chu, X., Doornbos, E., Funke, B., Goncharenko, L. P., Hervig, M. E., Schwartz, M. J., Sheese, P. E., Vargas, F., Williams, B. P., & Yuan, T. (2021). NRLMSIS 2.0: A whole-atmosphere empirical model of temperature and neutral species densities. *Earth and Space Science*, *8*(3). https://doi.org/10.1029/2020ea001321 (cit. on p. 24)

Flechtner, F., Dobslaw, H., & Fagiolini, E. (2015). AOD1B Product Description Document for Product Release 05 [Rev. 4.4]. ftp://isdcftp.gfz-potsdam.de/grace/DOCUMENTS/Level-1/GRACE_AOD1B_Product_Description_Document_for_RL05.pdf. (Cit. on p. 44)

Flechtner, F., Neumayer, K.-H., Dahle, C., Dobslaw, H., Fagiolini, E., Raimondo, J.-C., & Güntner, A. (2016). What can be expected from the GRACE-FO laser ranging interferometer for earth science applications? *Surveys in Geophysics*, *37*(2), 453–470. https://doi.org/10.1007/s10712-015-9338-y (cit. on p. 108)

Fliegel, H. F., & Gallini, T. E. (1996). Solar force modeling of block IIR global positioning system satellites. *Journal of Spacecraft and Rockets*, *33*(6), 863–866. https://doi.org/10.2514/3.26851 (cit. on p. 21)

Flury, J., Bettadpur, S., & Tapley, B. D. (2008). Precise accelerometry onboard the grace gravity field satellite mission. *Advances in Space Research*, *42*(8), 1414–1423. https://doi.org/10.1016/j.asr.2008.05.004 (cit. on p. 44)

Folkner, W., Williams, J., Boggs, D., Park, R., & Kuchynka, P. (2009). *The Planetary and Lunar Ephemeris DE421* (The Interplanetary Network Progress Report No. 42-178). Jet Propulsion Laboratory, Pasadena, California. http://ipnpr.jpl.nasa.gov/progress_report/42-178/178C.pdf. (Cit. on p. 13)

Frommknecht, B. (2007). *Integrated Sensor Analysis of the GRACE Mission* (Doctoral dissertation). Technischen Universität München. (Cit. on pp. 50, 91).

Goswami, S., Devaraju, B., Weigelt, M., & Mayer-Gürr, T. (2018). Analysis of GRACE range-rate residuals with focus on KBR instrument system noise. *Advances in Space Research*, *62*(2), 304–316. https://doi.org/https://doi.org/10.1016/j.asr.2018.04.036 (cit. on pp. 14, 44, 54, 62)

Harvey, N. (2016). GRACE star camera noise. *Adv. Space Res.*, *58*(3), 408–414. https://doi.org/10.1016/j.asr.2016.04.025 (cit. on p. 44)

Harvey, N., Dunn, C. E., Kruizinga, G. L., & Young, L. E. (2017a). Triggering conditions for GRACE ranging measurement signal-to-noise ratio dips. *Journal of Spacecraft and Rockets*, *54*(1), 327–330. https://doi.org/10.2514/1.a33578 (cit. on pp. 14, 73)

Harvey, N., Dunn, C. E., Kruizinga, G. L., & Young, L. E. (2017b). Triggering conditions for GRACE ranging measurement signal-to-noise ratio dips. *Journal of Spacecraft and Rockets*, *54*(1), 327–330. https://doi.org/10.2514/1.a33578 (cit. on pp. 51, 54, 62)

Harvey, N., McCullough, C. M., & Save, H. (2022). Modeling grace-fo accelerometer data for the version 04 release. *Advances in Space Research*, *69*(3), 1393–1407. https://doi.org/https://doi.org/10.1016/j.asr.2021.10.056 (cit. on pp. 82, 84, 92, 109)

Harvey, N., & Sakumura, C. (2019). Results from a GRACE/GRACE-FO attitude reconstruction kalman filter. *Journal of Geodesy*, *93*(10), 1881–1896. https://doi.org/10.1007/s00190-019-01289-z (cit. on p. 91)

Inácio, P., Ditmar, P., Klees, R., & Farahani, H. H. (2015). Analysis of star camera errors in GRACE data and their impact on monthly gravity field models. *J. Geod.*, *89*(6), 551–571. https://doi.org/10.1007/s00190-015-0797-1 (cit. on pp. 44, 54)

Iyemori, T., Takeda, M., Nose, M., Odagi, Y., & Toh, H. (2010). *Mid-latitude Geomagnetic Indices ASY and SYM for 2009* (tech. rep.). Internal Report of Data Analysis Center for Geomagnetism and Space Magnetism, Kyoto University, Japan. http://wdc.kugi.kyoto-u.ac.jp/aeasy/asy.pdf. (Cit. on p. 100)

Jekeli, C. (1981). *Alternative methods to smooth the Earth's gravity field* (tech. rep.). Department of Civil, Environmental Engineering, and Geodetic Science, The Ohio State University. (Cit. on p. 20).

Keller, W. (2004). *Wavelets in Geodesy and Geodynamics*. Walter de Gruyter. https://doi.org/10.1515/9783110198188. (Cit. on pp. 37, 44, 46)

Kim, J. (2000). *Simulation study of a low-low satellite-to-satellite tracking mission* (Doctoral dissertation). The University of Texas at Austin. http://geodesy.geology.ohio-state.edu/course/refpapers/Kim_diss_GRACE_00.pdf. (Cit. on pp. 50, 103)

Kim, J., & Tapley, B. (2002). Error Analysis of a Low-Low Satellite-to-Satellite Tracking Mission. *Journal of Guidance, Control, and Dynamics*, *25*(6), 1100–1106. https://doi.org/10.2514/2.4989 (cit. on pp. 9, 19, 44)

Klinger, B. (2018). *A contribution to GRACE time-variable gravity field recovery: Improved Level-1B data pre-processing methodologies* (Doctoral dissertation). Institute of Geodesy, Graz University of Technology. (Cit. on p. 12).

Klinger, B., & Mayer-Gürr, T. (2016a). The role of accelerometer data calibration within GRACE gravity field recovery: Results from ITSG-Grace2016. *Advances in Space Research*, *58*(9), 1597–1609. https://doi.org/https://doi.org/10.1016/j.asr.2016.08.007 (cit. on p. 12)

Klinger, B., & Mayer-Gürr, T. (2016b). The role of accelerometer data calibration within GRACE gravity field recovery: Results from ITSG-Grace2016. *Adv. Space Res.*, *58*(9), 1597–1609. https://doi.org/10.1016/j.asr.2016.08.007 (cit. on pp. 44, 62, 87)

Ko, U.-D., Tapley, B., Ries, J., & Bettadpur, S. (2012). High-Frequency Noise in the Gravity Recovery and Climate Experiment Intersatellite Ranging System. *Journal of Spacecraft and Rockets*, *49*(6), 1163–1173. https://doi.org/10.2514/1.a32141 (cit. on pp. 44, 51, 62)

Koch, K.-R. (1999). *Parameter Estimation and Hypothesis Testing in Linear Models*. Springer, Berlin, Heidelberg. https://doi.org/10.1007/978-3-662-03976-2. (Cit. on p. 31)

Koch, K.-R., & Kusche, J. (2002). Regularization of geopotential determination from satellite data by variance components. *Journal of Geodesy*, *76*(5), 259–268. https://doi.org/10.1007/s00190-002-0245-x (cit. on pp. 14, 34)

Kopp, G., & Lean, J. L. (2011). A new, lower value of total solar irradiance: Evidence and climate significance. *Geophysical Research Letters*, *38*(1), n/a–n/a. https://doi.org/10.1029/2010gl045777 (cit. on p. 25)

Krauss, S., Behzadpour, S., Temmer, M., & Lhotka, C. (2020). Exploring thermospheric variations triggered by severe geomagnetic storm on 26 august 2018 using GRACE follow-on data. *Journal of Geophysical Research: Space Physics*, *125*(5). https://doi.org/10.1029/2019ja027731 (cit. on p. 98)

Kurtenbach, E., Eicker, A., Mayer-Gürr, T., Holschneider, M., Hayn, M., Fuhrmann, M., & Kusche, J. (2012). Improved daily grace gravity field solutions using a kalman smoother [Mass Transport and Mass Distribution in the System Earth]. *Journal of Geodynamics*, *59-60*, 39–48. https://doi.org/https://doi.org/10.1016/j.jog.2012.02.006 (cit. on pp. 12, 44)

Kvas, A., Behzadpour, S., Ellmer, M., Klinger, B., Strasser, S., Zehentner, N., & Mayer-Gürr, T. (2018). Incorporation of background model uncertainties into the gravity field recovery process. https://meetingorganizer.copernicus.org/GSTM-2018/GSTM-2018-35.pdf. (Cit. on p. 44)

Kvas, A., Behzadpour, S., Ellmer, M., Klinger, B., Strasser, S., Zehentner, N., & Mayer-Gürr, T. (2019). ITSG-Grace2018: Overview and evaluation of a new GRACE-only

gravity field time series. *Journal of Geophysical Research: Solid Earth*, *124*(8), 9332–9344. https://doi.org/10.1029/2019jb017415 (cit. on pp. 3, 11, 12, 14, 43, 46, 100)

Kvas, A., Brockmann, J. M., Krauss, S., Schubert, T., Gruber, T., Meyer, U., Mayer-Gürr, T., Schuh, W.-D., Jäggi, A., & Pail, R. (2021). GOCO06s – a satellite-only global gravity field model. *Earth System Science Data*, *13*(1), 99–118. https://doi.org/10.5194/essd-13-99-2021 (cit. on pp. 13, 19)

Landerer, F. W., & Swenson, S. C. (2012). Accuracy of scaled GRACE terrestrial water storage estimates. *Water Resources Research*, *48*(4). https://doi.org/10.1029/2011wr011453 (cit. on p. 10)

Landerer, F. W., Flechtner, F. M., Save, H., Webb, F. H., Bandikova, T., Bertiger, W. I., Bettadpur, S. V., Byun, S. H., Dahle, C., Dobslaw, H., Fahnestock, E., Harvey, N., Kang, Z., Kruizinga, G. L. H., Loomis, B. D., McCullough, C., Murböck, M., Nagel, P., Paik, M., … Yuan, D.-N. (2020). Extending the global mass change data record: GRACE follow-on instrument and science data performance. *Geophysical Research Letters*, *47*(12). https://doi.org/10.1029/2020gl088306 (cit. on pp. 2, 5, 81, 91)

Loomis, B. D., Rachlin, K. E., Wiese, D. N., Landerer, F. W., & Luthcke, S. B. (2020). Replacing GRACE/GRACE-FO with satellite laser ranging: Impacts on antarctic ice sheet mass change. *Geophysical Research Letters*, *47*(3). https://doi.org/10.1029/2019gl085488 (cit. on p. 83)

Mallat, S. (1989). A theory for multiresolution signal decomposition: The wavelet representation. *IEEE Transactions on Pattern Analysis and Machine Intelligence*, *11*(7), 674–693. https://doi.org/10.1109/34.192463 (cit. on pp. 39–41)

Mayer-Gürr, T. (2006). *Gravitationsfeldbestimmung aus der analyse kurzer bahnbögen am beispiel der satellitenmissionen champ und grace* (Doctoral dissertation). Institute of Theoretical Geodesy, University of Bonn. http://hss.ulb.uni-bonn.de/2006/0904/0904.htm. (Cit. on p. 14)

Mayer-Gürr, T., Behzadpour, S., Eicker, A., Ellmer, M., Koch, B., Krauss, S., Pock, C., Rieser, D., Strasser, S., Süsser-Rechberger, B., Zehentner, N., & Kvas, A. (2021). Groops: A software toolkit for gravity field recovery and gnss processing. *Computers Geosciences*, *155*, 104864. https://doi.org/https://doi.org/10.1016/j.cageo.2021.104864 (cit. on p. 11)

McCullough, C., Bettadpur, S., & McDonald, K. (2015). Accuracy of numerical algorithms for satellite orbit propagation and gravity field determination. *Journal of Spacecraft and Rockets*, *52*(3), 766–775. https://doi.org/10.2514/1.a33008 (cit. on p. 82)

McCullough, C., Harvey, N., Save, H., & Bandikova, T. (2019). *Description of Calibrated GRACE-FO Accelerometer Data Products (ACT), Level-1 Product Version 04* (tech. rep. JPL D-103863). Jet Propulsion Laboratory, Pasadena, California. https://podaac-tools.jpl.nasa.gov/drive/files/allData/grace/docs/ATBD_L1B_v1.2.pdf. (Cit. on pp. 7, 81, 82, 84, 91, 92)

Meyer, U., Jäggi, A., & Beutler, G. (2011). The impact of attitude control on GRACE accelerometry and orbits. *Geodesy for Planet Earth* (pp. 139–146). Springer Berlin Heidelberg. https://doi.org/10.1007/978-3-642-20338-1_17. (Cit. on pp. 82, 91)

Meyer, Y. (1993). *Wavelets and Operators* (Vol. 1). Cambridge University Press. https://doi.org/10.1017/CBO9780511623820. (Cit. on p. 41)

Misfeldt, M. (2019). Data processing and investigations for the GRACE Follow-On laser ranging interferometer. https://doi.org/doi.org/10.15488/9639. (Cit. on p. 108)

Moe, K., & Moe, M. M. (2005). Gas–surface interactions and satellite drag coefficients. *Planetary and Space Science*, *53*(8), 793–801. https://doi.org/10.1016/j.pss.2005.03.005 (cit. on p. 24)

Montenbruck, O., Steigenberger, P., & Hugentobler, U. (2014). Enhanced solar radiation pressure modeling for Galileo satellites. *Journal of Geodesy*, *89*(3), 283–297. https://doi.org/10.1007/s00190-014-0774-0 (cit. on p. 29)

Montenbruck, O., & Gill, E. (2000). *Satellite orbits*. Springer Berlin Heidelberg. https://doi.org/10.1007/978-3-642-58351-3. (Cit. on pp. 26, 27, 115)

Peterseim, N. (2014). *TWANGS – High-Frequency Disturbing Signals in 10 Hz Accelerometer Data of the GRACE Satellites* (Doctoral dissertation). Technischen Universität München. (Cit. on pp. 91, 92).

Peterseim, N., Flury, J., & Schlicht, A. (2012). Magnetic torquer induced disturbing signals within grace accelerometer data. *Advances in Space Research*, *49*(9), 1388–1394. https://doi.org/https://doi.org/10.1016/j.asr.2012.02.013 (cit. on p. 44)

Petit, G., & Luzum, B. (Eds.). (2010). *IERS Conventions (2010)*. Verlag des Bundesamts für Kartographie und Geodäsie. (Cit. on pp. 13, 18, 114).

Prieto, D. M., Graziano, B. P., & Roberts, P. C. (2014). Spacecraft drag modelling. *Progress in Aerospace Sciences*, *64*, 56–65. https://doi.org/10.1016/j.paerosci.2013.09.001 (cit. on p. 24)

Robertson, R., Flury, J., Bandikova, T., & Schilling, M. (2015). Highly physical penumbra solar radiation pressure modeling with atmospheric effects. *Celestial Mechanics and Dynamical Astronomy*, *123*(2), 169–202. https://doi.org/10.1007/s10569-015-9637-0 (cit. on p. 26)

Rodriguez-Solano, C. J., Hugentobler, U., & Steigenberger, P. (2011). Impact of albedo radiation on GPS satellites. *Geodesy for planet earth* (pp. 113–119). Springer Berlin Heidelberg. https://doi.org/10.1007/978-3-642-20338-1_14. (Cit. on pp. 21, 30, 31)

Save, H. V., Bettadpur, S. V., & Tapley, B. D. (2006). Single Accelerometer Gravity Solutions for GRACE (cit. on p. 82).

Shihora, L., & Dobslaw, H. (2020). *Towards AOD1B RL07* [Presented at the GRACE / GRACE-FO Science Team Meeting 2020, Abstract GSTM2020-29,]. (Cit. on p. 108).

Siemes, C., de Teixeira da Encarnação, J., Doornbos, E., van den IJssel, J., Kraus, J., Pereštý, R., Grunwaldt, L., Apelbaum, G., Flury, J., & Olsen, P. E. H. (2016).

Swarm accelerometer data processing from raw accelerations to thermospheric neutral densities. *Earth, Planets and Space*, *68*(1). https://doi.org/10.1186/s40623-016-0474-5 (cit. on p. 100)

Tapley, B., Bettadpur, S., Watkins, M., & Reigber, C. (2004). The gravity recovery and climate experiment: Mission overview and early results. *Geophys. Res. Lett.*, *31*(9). https://doi.org/10.1029/2004gl019920 (cit. on pp. 2, 5)

Touboul, P., Foulon, B., & Willemenot, E. (1999). Electrostatic space accelerometers for present and future missions11based on paper iaf.96.j1.02 presented at the 47th international astronautical congress, 7–11 october, 1996, beijing, china. *Acta Astronautica*, *45*(10), 605–617. https://doi.org/https://doi.org/10.1016/S0094-5765(99)00132-0 (cit. on p. 7)

van Dam, T., & Ray, R. D. (2010). S1 and S2 Atmospheric Tide Loading Effects for Geodetic Applications. http://geophy.uni.lu/ggfc-atmosphere/tide-loading-calculator.html. (Cit. on p. 13)

van Etten, W. C. (2006). *Introduction to random signals and noise*. John Wiley & Sons, Ltd. https://doi.org/10.1002/0470024135. (Cit. on p. 14)

Vetterli, M., & Herley, C. (1992). Wavelets and filter banks: theory and design. *IEEE Transactions on Signal Processing*, *40*(9), 2207–2232. https://doi.org/10.1109/78.157221 (cit. on p. 40)

Vokrouhlicky, D., Farinella, P., & Mignard, F. (1994). Solar radiation pressure perturbations for Earth satellites. III. Global atmospheric phenomena and the albedo effect. *Astronomy and Astrophysics*, *290*, 324–334 (cit. on p. 21).

Wahr, J., Molenaar, M., & Bryan, F. (1998). Time variability of the earth's gravity field: Hydrological and oceanic effects and their possible detection using GRACE. *Journal of Geophysical Research: Solid Earth*, *103*(B12), 30205–30229. https://doi.org/10.1029/98jb02844 (cit. on p. 20)

Wen, H. Y., Kruizinga, G., Paik, M., Landerer, F., Bertiger, W., Sakumura, C., Bandikova, T., & McCullough, C. (2019). *Gravity Recovery and Climate Experiment Follow-On (GRACE-FO) Level-1 Data Product User Handbook* (tech. rep. JPL D-56935 (URS270772)). Jet Propulsion Laboratory, Pasadena, California. https://podaac-tools.jpl.nasa.gov/drive/files/allData/gracefo/docs/GRACE-FO_L1_Handbook.pdf. (Cit. on pp. 5, 9, 21, 29)

Wielicki, B. A., Barkstrom, B. R., Harrison, E. F., Lee, R. B., Smith, G. L., & Cooper, J. E. (1996). Clouds and the earth's radiant energy system (CERES): An earth observing system experiment. *Bulletin of the American Meteorological Society*, *77*(5), 853–868. https://doi.org/10.1175/1520-0477(1996)077⟨0853:catere⟩2.0.co;2 (cit. on pp. 30, 31)

Wouters, B., Gardner, A. S., & Moholdt, G. (2019). Global glacier mass loss during the GRACE satellite mission (2002-2016). *Frontiers in Earth Science*, *7*. https://doi.org/10.3389/feart.2019.00096 (cit. on p. 2)

Wu, S.-C., Kruizinga, G., & Bertiger, W. (2006). *Algorithm Theoretical Basis Document for GRACE Level-1B Data Processing V1.2* (tech. rep. GRACE 327-741). Jet Propulsion Laboratory, Pasadena, California. https://podaac-tools.jpl.nasa.gov/drive/files/allData/grace/docs/ATBD_L1B_v1.2.pdf. (Cit. on pp. 81, 84, 85)

Zehentner, N., & Mayer-Gürr, T. (2016). Precise orbit determination based on raw GPS measurements. *Journal of Geodesy*, *90*(3), 275–286. https://doi.org/10.1007/s00190-015-0872-7 (cit. on p. 12)

List of Abbreviations

ACC	Accelerometer
ACT	Calibrated Accelerometer Data
AIUB	Astronomical Institute of the University of Bern
AOC	Antenna Offset Correction
APC	Antenna Phase Center
AR	Autoregressive
CERES	Clouds and Earth's Radiant Energy System
CNES	Le Centre national d'études spatiales
CoM	Center of Mass
cpr	cycle-per-revolution
CRN	A digital filter of N-th order self-Convolution with a Rectangular window function
CSR	Center for Space Research at the University of Texas at Austin
DORIS	Doppler Orbitography and Radio Positioning Integrated by Satellite
DLR	German Aerospace Center
DWT	Discrete Wavelet Transform
ERP	Earth Radiation Pressure
EWH	Equivalent Water Height
FoV	Field of View
FWT	Fast Wavelet Transform
GFZ	German Research Centre for Geosciences
GPS	Global Navigation Satellite System

GRACE	Gravity Recovery and Climate Experiment
GRACE-FO	Gravity Recovery and Climate Experiment
GRGS	Le Groupe de Recherche de Géodésie Spatiale
ICRF	International Celestial Reference Frame
IERS	International Earth Rotation and Reference System Service
IPU	Instrument Processing Unit
ITSG	working group of Satellite Geodesy and Theoretical Geodesy at Graz University of Technology
JPL	Jet Propulsion Laboratory
KBR	K-band ranging system
LEO	Low Earth Orbit
LOS	Line of Sight
LRI	Laser Ranging Interferometer
LSA	Least Square Adjustment
MOS	Mission Operation System
MRA	Multiresolution Analysis
NASA	National Aeronautics and Space Administration
OBC	On-Board Computer
ONERA	Office National d'Études et de Recherches Aérospatiales
PSD	Power Spectral Density
RDC	Raw Data Center
RMS	Root Mean Square
SCA	Star Camera Assembly
SCF	Star Camera Frame
SDS	Science Data System
SIS	Science Instrument System
SLR	Satellite Laser Ranging

SNR	Signal to Noise Ratio
SORCE	Solar Radiation and Climate Experiment
SRP	Solar Radiation Pressure
SH	Spherical Harmonics
STFT	Short Time Fourier Transform
TN-14	Technical Note-14
TRF	Terrestrial Reference Frame
TSI	Total Solar Irradiance
TUG	Graz University of Technology
UCBS	Uniform Cubic Basis Spline
USO	Ultra-Stable Oscillator
VCE	Variance Component Estimation
VLBI	Very Long Baseline Interferometry
w.r.t	with respect to

List of Figures

List of Tables